MODELLING THE TIME EVOLUTION OF THE STRUCTURE FACTOR IN POLYMER BLENDS

MATTHEW JONES

School of Mathematical and Physical Sciences
University of Sheffield

A thesis submitted in partial fulfilment of the requirements for the degree of Doctor of Philosophy

October 2024

Declaration of Authorship

I, Matthew Jones, declare that the work presented in this thesis, except where otherwise stated, is based on my own research, guided by my supervisor, Professor Nigel Clarke, and has not been submitted previously for a degree at any university or institution.

Acknowledgements

First and foremost, thank you to my supervisor, Nigel Clarke. I am grateful for your support, guidance, encouragement and entertaining cycling stories.

Thank you to those who facilitated graduate teaching opportunities within the department. I have many happy memories from helping in the computer labs and math problems classes.

Thank you to the professional services staff for administrating our research training support grants, supporting our welfare and all the other vital things you do.

Thank you to the research software engineering team for helping to set meup on Stanage.

Thank you to my friends and housemates. Whether we ran, swam, walked, shared a lunch break or played music together, you gave me balance and perspective.

Thank you to Mum, Dad, Tim, Em and Nicole. I am eternally grateful for your love, support, wisdom and humour.

Abstract

Polymer blends can exhibit a range of phase behaviour. During phase transitions, the evolution of the microstructure can be monitored using small-angle scattering. Information about the microstructure can be deduced from measurements of the structure factor – a quantity directly proportional to the scattered intensity. While the time evolution of the structure factor can be measured relatively easily, modelling it has proved to be much more difficult. We believe the latter could be impeding our ability to control the underlying phase transitions.

In this thesis, we are primarily concerned with thermally-induced polymeric spinodal decomposition and dissolution. The equation of motion for the structure factor during these phase transitions is known to be unclosed, i.e. an infinite hierarchy of coupled differential equations. Existing attempts to model the time evolution of the structure factor during spinodal decomposition and dissolution have focussed on deriving approximate equations of motion based on truncation schemes.

Arguably, the most advanced approximate equation of motion was derived by Akcasu et al. We refer to this as the Akcasu equation. There is very little literature aimed at testing the Akcasu equation. To rectify this, we tested the Akcasu equation using synthetic structure factor snapshots derived from simulations. In the case of dissolution, the Akcasu equation performed well at describing the time evolution of the synthetic structure factor snapshots. In the case of spinodal decomposition, we determined that improvements are required. We hope these respective findings motivate further experimental testing and modelling work.

Embracing the duality between the fact the structure factor is hard to model but relatively easy to measure, we investigated the application of system identification techniques to the problem of modelling the time evolution of the structure factor during spinodal decomposition. One technique we considered is dynamic mode decomposition. We demonstrated the ability of dynamic mode decomposition to make accurate future predictions of synthetic structure factor snapshots based on the knowledge of previous ones. While further research is required, we believe our findings could be promising for developing a system to control spinodal decomposition.

Dynamic mode decomposition is a linear and equation-free system identification technique. This prompted us to investigate system identification techniques that output parsimonious non-linear governing equations. We had mixed success in this direction, demonstrating that one such technique could not be applied to the problem while another showed promising signs. We provide a comprehensive outline of how one could build on these findings.

Contents

Chapter 1

Introduction

1.1 Context

Polymer blends, the polymer equivalent of metal alloys, offer the chance to develop new materials with unique properties. In general, polymer blends are prone to phase separating, leading to the formation of phase-separated microstructures, which affect the properties of the resulting material [1]. Phase separation can be key to the emergence of desirable properties - see, for example, [2–5].

In this thesis, we are primarily concerned with thermally-induced polymeric spinodal decomposition [6, 7] - the process of spontaneous phase separation following a temperature change into the unstable region of the phase diagram. We also consider dissolution [8, 9] - the process by which phase-separated microstructures dissipate.

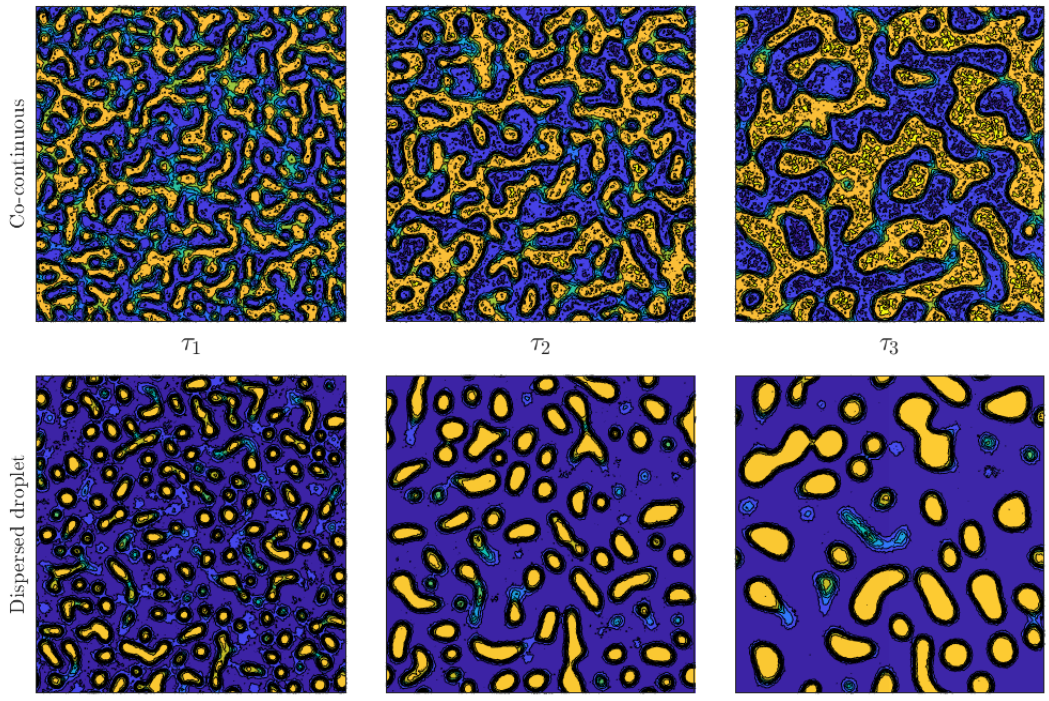

Figure 1.1: The development of a co-continuous and a dispersed droplet microstructure captured at three times $\tau_1 < \tau_2 < \tau_3$ during simulations of spinodal decomposition. Simulating spinodal decomposition is discussed in chapter 3.

Depending on several factors, such as the temperature of the blend and the ratio of the constituent polymers, spinodal decomposition can give rise to a range of phase-separated microstructures, from dispersed droplets to co-continuous networks [10, 11]. Figure 1.1 shows the development of such microstructures during simulations of spinodal decomposition. Polymeric materials with co-continuous microstructures have generated significant interest over recent years, finding applications in many industries, including renewable energy, membrane technology and metamaterials [2, 4, 5, 12–14]. Improving our ability to control spinodal decomposition and dissolution could drive advances in these industries, as well as many others, by opening the door to the development of tailored, tunable microstructures.

The development of the microstructure during spinodal decomposition and dissolution can be monitored in real time using small-angle scattering. Figure 1.2 shows a schematic of a small-angle scattering experiment in the context of a polymer blend undergoing spinodal decomposition. Information about the microstructure can be deduced from measurements of the structure factor [15, 16] - a quantity that is directly proportional to the scattered intensity.

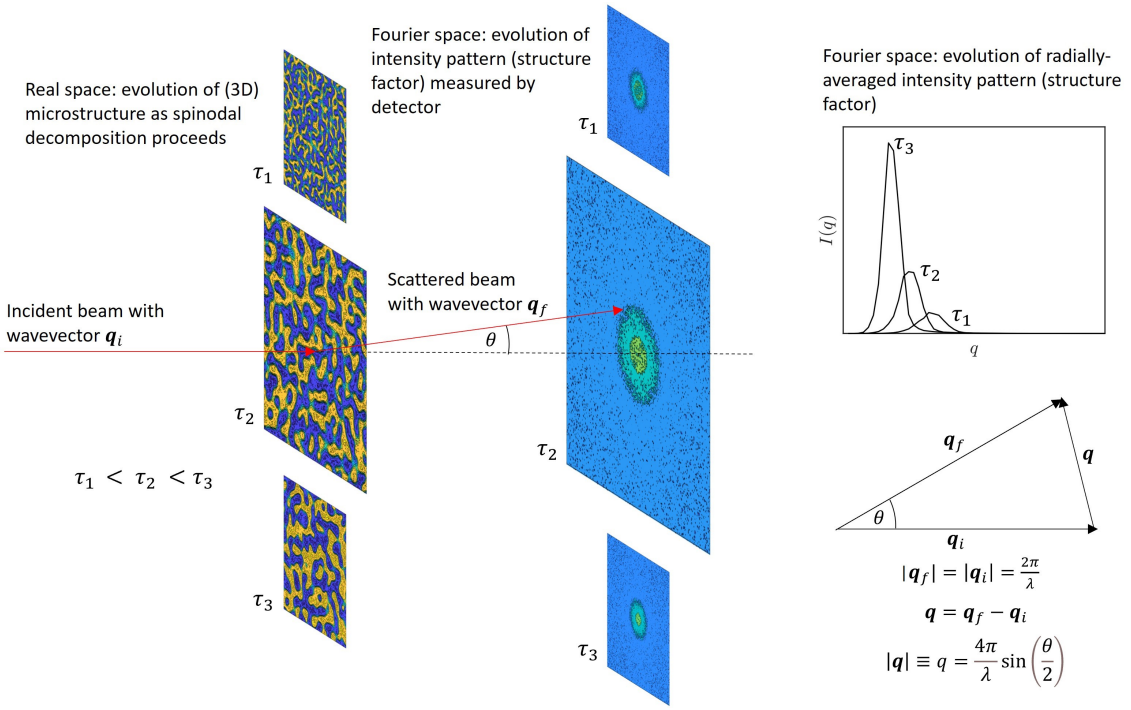

Figure 1.2: A schematic of a small-angle scattering experiment in the context of a polymer blend undergoing spinodal decomposition. Small-angle scattering experiments are outlined in chapter 2.

The equation of motion for the structure factor during spinodal decomposition and dissolution is known to be unclosed [17–19]. In other words, it is an intractable infinite hierarchy of coupled differential equations. Existing attempts to model the time evolution of the structure factor have focussed on deriving approximate equations of motion based on truncation schemes. Of these approximate equations of motion, perhaps the most commonly used is the linear Cahn-Hilliard-Cook Flory-Huggins-de Gennes equation [20–26]. This equation has proved to be a useful tool in the analysis of scattering data [2, 10, 27–29]. However, it is only applicable under a restrictive set of conditions and assumptions [8, 26, 30]. Motivated to improve this

situation, Akcasu et al. set out to derive a non-linear equation of motion [19,31,32]. We refer to this equation as the Akcasu equation. There is currently very little literature aimed at testing the Akcasu equation [31].

There is a duality to the situation outlined above: the structure factor is relatively easy to measure but hard to model. The nature of this duality is the driving force behind recent developments in the field of system identification, which is concerned with building models of dynamical systems from data [33].

1.2 Aims

We believe we lack an adequate model for the time evolution of the structure factor during spinodal decomposition and dissolution. This could be impeding our ability to control these processes: without an adequate model for the structure factor, it will be hard to make future predictions of the structure factor - valuable information for a control system. With this in mind, we set out to:

- Test the Akcasu equation for the time evolution of the structure factor
- Explore the application of system identification techniques to the problem of modelling the time evolution of the structure factor

To allow us to have as much control as possible in our investigations, we worked with synthetic time series of structure factor snapshots, which we generated ourselves.

1.3 Thesis structure

The remaining chapters of this thesis are structured as follows. In the next chapter, we outline the theories and techniques underpinning our work. In chapter 3, we detail how we generated the synthetic time series we used to obtain our results. In chapter 4, we test the Akcasu equation. In chapter 5, we apply a linear system identification technique called dynamic mode decomposition to the problem of modelling the time evolution of the structure factor during polymeric spinodal decomposition. In chapter 6, we investigate the application of non-linear system identification techniques. Finally, in chapter 7, we conclude the thesis by summarising our key findings and potential directions for future research.

Chapter 2

Background

2.1 Introduction

In this chapter, we outline the theories and techniques underpinning the work in this thesis. We start, in section 2.2, by considering the phase behaviour of polymer blends. Next, in section 2.3, we focus on the mechanisms of phase separation and dissolution in polymer blends. Next, in section 2.4, we consider the application of small-angle scattering experiments to polymer blends. Finally, in section 2.5, we outline the field of system identification, focussing on the techniques pertinent to this thesis.

2.2 Phase behaviour of polymer blends

2.2.1 Free energy of mixing

The phase behaviour of a polymer blend, or any mixture, can be predicted from knowledge of the free energy [6], a thermodynamic potential that quantifies the maximum amount of work a system can do on its surroundings at constant temperature. The mathematical definition of the free energy depends on the constraints imposed on the system by its surroundings. Assuming the volume of the system is fixed, the free energy is defined as follows [34]:

$$F = U - TS, \tag{2.1}$$

where U is the internal energy, T is the temperature and S is the entropy. This form of the free energy is known as the Helmholtz free energy.

To illustrate why the free energy can be used as a predictor of phase behaviour, we consider the first law of thermodynamics. This states that the change in the internal energy of a system is equal to the sum of the work done on the system, dW, and the heat supplied to it, dQ [34]:

$$dU = dW + dQ. \tag{2.2}$$

In words, energy is conserved. Depending on whether the heat is supplied reversibly or not, dQ is related to the change in entropy, dS, via [34]

$$dQ \leq TdS, \tag{2.3}$$

where the equality holds in the case of reversible heat supply. Combining equations 2.1 - 2.3, it can be shown that

$$dF \leq dW. \tag{2.4}$$

If the system were to be mechanically isolated from its surroundings, then $dW = 0$ and equation 2.4 becomes

$$dF \leq 0. \tag{2.5}$$

From this equation, we can infer that any process that might occur within the system, e.g. phase separation, will occur if it causes the free energy to decrease, and the equilibrium state is achieved by minimising the free energy. These inferences suggest that we can predict the phase behaviour of a polymer blend when armed with the knowledge of its free energy function.

Instead of considering the 'full' free energy, it is convenient to consider a quantity called the free energy of mixing instead. For a binary blend, the free energy of mixing is defined as the free energy change associated with forming a homogeneous blend from pure samples of two different species, labelled A and B [6]:

$$F_{\text{mix}} = F_{A+B} - (F_A + F_B), \tag{2.6}$$

where F_{A+B} is the free energy of the homogeneous blend of A and B, F_A is the free energy of the pure sample of A, and F_B is the free energy of the pure sample of B. The free energy of mixing tells us the free energy of the fully mixed state relative to the fully unmixed state. Combining equation 2.1 with equation 2.6, we obtain

$$F_{\text{mix}} = U_{\text{mix}} - TS_{\text{mix}}, \tag{2.7}$$

where $U_{\text{mix}} = U_{A+B} - (U_A + U_B)$ is the internal energy of mixing and $S_{\text{mix}} = S_{A+B} - (S_A + S_B)$ is the entropy of mixing. As in equation 2.6, the subscript $A+B$ refers to the homogeneous blend of A and B, the subscript A refers to the pure sample of A, and the subscript B refers to the pure sample of B.

2.2.2 Regular solution theory for small molecule mixtures

By virtue of its simplicity and the fact it can be applied semi-empirically, a commonly used theory to calculate the free energy of mixing in polymer blends is the Flory-Huggins theory [23, 24, 35, 36]. This theory, which was developed independently by Flory and Huggins, is rooted in the regular solution theory for small molecule mixtures [6, 37]. We outline the regular solution theory first [6, 23].

The regular solution theory is based on a lattice model of mixing, i.e. the molecules of the constituent species are assumed to occupy a regular lattice, with each molecule occupying a single lattice site at any discrete moment in time. Molecules belonging to the same species are assumed to be indistinguishable from each other. To calculate the free energy of mixing, the theory invokes the mean-field assumption that the mixing is random. This means that, in the mixed state, the probability of a given lattice site containing a molecule of A or B is independent of its nearest neighbours. It is assumed that there are short-ranged energetic interactions between the constituent molecules. Collectively, the assumptions of random mixing and short-ranged interactions are called the regular solution assumptions.

With equation 2.7 in mind, we first consider the entropy of mixing. Making use of Boltzmann's relation for the entropy,

$$S = k_B \ln \Omega, \tag{2.8}$$

where k_B is Boltzmann's constant and Ω is the number of microstates, this can be written as

$$S_{\text{mix}} = k_B \ln \frac{\Omega_{A+B}}{\Omega_A \Omega_B}, \tag{2.9}$$

where Ω_{A+B} is the number of microstates corresponding to a homogeneous mixture of A and B, Ω_A is the number of microstates corresponding to a pure sample of A, and Ω_B is the number of microstates corresponding to a pure sample of B. Under the random mixing assumption, the number of microstates in the mixed state is equal to the number of indistinguishable ways of placing n_A molecules of A (or, equivalently, n_B molecules of B) on $n = n_A + n_B$ lattice sites:

$$\Omega_{\text{A+B}} = \frac{n!}{n_A! n_B!}. \tag{2.10}$$

In the unmixed state, $\Omega_A = \Omega_B = 1$. Substituting equation 2.10 and $\Omega_A = \Omega_B = 1$ into equation 2.9 gives

$$S_{\text{mix}} = k_B(\ln n! - \ln n_A! - \ln n_B!). \tag{2.11}$$

Using Stirling's approximation, which is valid in the limit $n_A, n_B >> 1$, we can write

$$S_{\text{mix}} = k_B\Big(n_A \ln \frac{n_A + n_B}{n_A} + n_B \ln \frac{n_A + n_B}{n_B}\Big). \tag{2.12}$$

It is often desirable to work in terms of intensive ('per lattice site') variables. With this in mind, we introduce the volume fractions of A and B, which are defined as

$$\phi_A = \frac{n_A}{n_A + n_B} \tag{2.13a}$$

$$\phi_B = \frac{n_B}{n_A + n_B}. \tag{2.13b}$$

Upon substituting equations 2.13a and 2.13b into equation 2.12 and rearranging, we obtain the following equation for the entropy of mixing per lattice site:

$$S_{\text{mix}}^{\text{lat}} \equiv \frac{S_{\text{mix}}}{n} = -k_B(\phi_A \ln \phi_A + \phi_B \ln \phi_B). \tag{2.14}$$

We now consider the internal energy of mixing. Under the assumption that there are short-ranged interactions between the constituent molecules, we only need to consider the nearest-neighbour interactions. Making use of the random mixing assumption, a given molecule in the mixed state has, on average, $z\phi_A$ nearest neighbours of type A and $z\phi_B$ nearest neighbours of type B, where z is the number of nearest neighbour lattice sites. This corresponds to there being $\frac{1}{2}n\phi_A z\phi_A$ '$A-A$' interactions, $\frac{1}{2}n\phi_B z\phi_B$ '$B-B$' interactions and $n\phi_A z\phi_B$ '$A-B$' interactions in the mixed state. The factor of $\frac{1}{2}$ in the first two quantities prevents counting each interaction twice. Denoting the interaction energy for each possible pair of nearest

neighbours as ϵ_{AA}, ϵ_{BB} and ϵ_{AB}, the internal energy in the mixed state per lattice site is given by

$$\frac{U_{A+B}}{n} = \frac{z}{2}(\phi_A^2\epsilon_{AA} + \phi_B^2\epsilon_{BB} + 2\phi_A\phi_B\epsilon_{AB}). \tag{2.15}$$

In the unmixed state,

$$\frac{U_A + U_B}{n} = \frac{z}{2}(\phi_A\epsilon_{AA} + \phi_B\epsilon_{BB}). \tag{2.16}$$

Therefore, the internal energy of mixing per lattice site is given by

$$U_{\text{mix}}^{\text{lat}} \equiv \frac{U_{\text{mix}}}{n} = \frac{z}{2}((\phi_A^2 - \phi_A)\epsilon_{AA} + (\phi_B^2 - \phi_B)\epsilon_{BB} + 2\phi_A\phi_B\epsilon_{AB}). \tag{2.17}$$

An implicit assumption in the regular solution theory is that the mixture is incompressible. As a result, $\phi_A + \phi_B = 1$. Using this relationship, equation 2.17 can be rewritten as

$$U_{\text{mix}}^{\text{lat}} = \frac{z}{2}(-\phi_A\phi_B\epsilon_{AA} - \phi_A\phi_B\epsilon_{BB} + 2\phi_A\phi_B\epsilon_{AB}) \tag{2.18a}$$

$$= \phi_A\phi_B\chi k_BT, \tag{2.18b}$$

where

$$\chi = \frac{z}{2k_BT}(2\epsilon_{AB} - \epsilon_{AA} - \epsilon_{BB}). \tag{2.19}$$

The parameter χ is known as the interaction parameter since it encapsulates the energetic interactions between the molecules in the mixture.

Inserting equation 2.14 and 2.18b into an intensive version of equation 2.7 yields the regular solution equation for the free energy of mixing per lattice site in a binary small molecule mixture

$$\frac{F_{\text{mix,RS}}^{\text{lat}}}{k_BT} = \phi_A \ln \phi_A + \phi_B \ln \phi_B + \phi_A\phi_B\chi. \tag{2.20}$$

2.2.3 Flory-Huggins theory for polymer-solvent mixtures

Next, we outline how Flory and Huggins extended the regular solution theory to polymer-solvent mixtures [23, 38]. Again, we adopt a lattice model of mixing and make the same assumptions as listed at the start of section 2.2.2. We label the polymer component as A and the solvent (small molecule) component as B. Given that there are n_A polymer molecules, each formed of N monomers, and n_B solvent molecules, the total number of lattice sites can be expressed in terms of the number of monomers, polymers and solvent molecules as $n = Nn_A + n_B$. In this case, the volume fractions of A and B are defined as

$$\phi_A = \frac{Nn_A}{Nn_A + n_B} \tag{2.21a}$$

$$\phi_B = \frac{n_B}{Nn_A + n_B}. \tag{2.21b}$$

The monomers referred to above are defined such that they fit on the lattice sites. Equating the volume of a lattice site with a solvent molecule and denoting this v_0, N is related to the number of actual monomers $\hat{N}$ via [39]

$$N = \frac{\hat{N}v}{v_0}, \tag{2.22}$$

where v is the volume of each actual monomer. We note that this is only an approximate correction for dealing with differences in the monomer and solvent volumes.

With equation 2.7 in mind, we first consider the entropy of mixing. In the mixed state, we must count the number of ways of placing n_A polymers on the lattice. The solvent molecules can be thought of as filling the gaps, therefore their placement does not contribute to the total number of microstates. By considering the $(j+1)^{th}$ polymer, a general, approximate, equation for the number of ways of placing a single polymer can be derived. The first segment of the $(j+1)^{th}$ polymer can be placed on any of the $n - Nj$ available lattice sites. The second segment can be placed on $z\Big(\frac{n-Nj}{n}\Big)$ lattice sites, where the fraction denotes the probability that a given lattice site is free. The third and higher segments can be placed on $(z-1)\Big(\frac{n-Nj}{n}\Big)$ lattice sites. For simplicity, the possibility that one of the nearest neighbour lattice sites could be occupied by another monomer of the same polymer has been neglected. Putting the above steps together, the number of ways of placing the $(j+1)^{th}$ polymer is

$$\omega_{j+1} = (n - Nj)z\Big(\frac{n-Nj}{n}\Big)\Big((z-1)\Big(\frac{n-Nj}{n}\Big)\Big)^{N-2} \tag{2.23a}$$

$$\approx n(z-1)^{N-1}\Big(1 - \frac{Nj}{n}\Big)^N, \tag{2.23b}$$

where the approximation holds for large N. The number of indistinguishable microstates is given by

$$\Omega_{A+B} = \frac{\omega_1 \times ... \times \omega_j \times ... \times \omega_{n_A}}{n_A!} \tag{2.24a}$$

$$= \frac{1}{n_A!}\prod_{j=0}^{n_A-1}\omega_{j+1}, \tag{2.24b}$$

where the denominator accounts for the fact that the polymers are indistinguishable. Making use of equation 2.8, the entropy of the mixed state is given by

$$S_{A+B} = k_B \ln \prod_{j=0}^{n_A-1}\frac{\omega_{j+1}}{n_A!} \tag{2.25a}$$

$$= k_B \sum_{j=0}^{n_A-1}\ln\frac{\omega_{j+1}}{j+1}. \tag{2.25b}$$

To evaluate this, we may replace the sum with an integral:

$$S_{A+B} = k_B \int_0^{n_A-1} dj \Big[\ln\Big(n(z-1)^{N-1}\Big(1-\frac{Nj}{n}\Big)^N\Big) - \ln(j+1)\Big] \tag{2.26a}$$

$$= nk_B\Big[\frac{-\phi_A}{N}\ln(\phi_A) - (1-\phi_A)\ln(1-\phi_A) + \frac{\phi_A}{N}(1+\ln(N)) + \phi_A \ln\Big(\frac{z-1}{e}\Big)\Big]. \tag{2.26b}$$

As we saw in the small molecule mixture, the entropy of the unmixed solvent is zero. However, this is not the case for the unmixed polymer, which we assume to be disordered. Due to the connectivity, there are many different ways of placing the polymers to fill the lattice in the unmixed state. Only in the situation where the polymers align, forming a polymer crystal, is the entropy zero - deviations from a crystalline structure are reflected in a non-zero entropy. The entropy of the disordered unmixed polymer state can be calculated using equation 2.26b by setting $n = Nn_A$, i.e $n_B = 0$, and $\phi_A = 1$. It follows that

$$S_A = k_B\Big(n_A(1+\ln(N)) + Nn_A \ln\Big(\frac{z-1}{e}\Big)\Big), \tag{2.27}$$

or, in terms of ϕ_A (equation 2.21a),

$$S_A = nk_B\Big(\frac{\phi_A}{N}(1+\ln(N)) + \phi_A \ln\Big(\frac{z-1}{e}\Big)\Big). \tag{2.28}$$

Therefore, using equations 2.26b and 2.28, as well as $S_B = 0$, we can write the entropy of mixing per lattice site as

$$S^{\text{lat}}_{\text{mix}} = k_B\Big(\frac{-\phi_A}{N}\ln(\phi_A) - (1-\phi_A)\ln(1-\phi_A)\Big) \tag{2.29a}$$

$$= -k_B\Big(\frac{\phi_A}{N}\ln(\phi_A) + \phi_B \ln(\phi_B)\Big), \tag{2.29b}$$

where we used the incompressibility assumption to write $\phi_B = 1-\phi_A$. We note that, in equation 2.29b, the entropic contribution of the polymer component is inversely proportional to the degree of polymerisation. This can be interpreted as a reduction in the number of configurations available to polymers in the mixed state compared to small molecules [40].

We now consider the internal energy of mixing. For simplicity, we assume that, on average, each monomer and solvent molecule in the mixed state has $z\phi_A$ monomer nearest neighbours and $z\phi_B$ solvent nearest neighbours. This is an approximation since each monomer in a linear polymer chain, excluding those at the ends, actually has $z-2$ nearest neighbour sites available to form energetic contacts - each monomer within a chain is covalently bonded to two other monomers. We note that interactions between covalently bonded monomers are irrelevant since they are the same in the mixed and unmixed states. Proceeding, nonetheless, without accounting for the connectivity of the monomers, there are, on average, $\frac{1}{2}n\phi_A z\phi_A$ 'A-A' interactions, $\frac{1}{2}n\phi_A z\phi_B$ 'B-B' interactions and $n\phi_A z\phi_B$ 'A-B' interactions in the mixed state to consider. It follows that the internal energy of mixing per lattice site in the polymer-solvent mixture is given by equation 2.18b, i.e. the same equation for small molecule mixtures, albeit with ϕ_A and ϕ_B defined in equations 2.21a and 2.21b instead of equations 2.13a and 2.13b.

Inserting equations 2.29b and 2.18b into an intensive version of equation 2.7 yields the Flory-Huggins equation for the free energy of mixing per lattice site in a polymer-solvent mixture

$$\frac{F^{\text{lat}}_{\text{mix,PS}}}{k_B T} = \frac{\phi_A}{N} \ln(\phi_A) + \phi_B \ln(\phi_B) + \phi_A \phi_B \chi. \tag{2.30}$$

2.2.4 Flory-Huggins theory for polymer blends

We are now in a position to generalise equation 2.30 to polymer blends. First, we rewrite N as N_A. Second, we replace the solvent with a second type of polymer formed of N_B 'lattice site' monomers. We must now modify equation 2.30 to include N_B, while ensuring we recover equation 2.30 when $N_B = 1$. Indeed, based on the previous generalisation from small molecule mixtures to polymer-solvent mixtures, we expect that the volume fractions and the entropy of mixing term require modification. It follows that the Flory-Huggins equation for the free energy of mixing per lattice site in a polymer blend is given by [6]

$$\frac{F^{\text{lat}}_{\text{mix,PP}}}{k_B T} = \frac{\phi_A}{N_A} \ln(\phi_A) + \frac{\phi_B}{N_B} \ln(\phi_B) + \phi_A \phi_B \chi, \tag{2.31}$$

where

$$\phi_A = \frac{N_A n_A}{N_A n_A + N_B n_B} \tag{2.32a}$$

$$\phi_B = \frac{N_B n_B}{N_A n_A + N_B n_B}. \tag{2.32b}$$

Only slightly unfavourable interactions between unlike pairs of monomers, which correspond to small positive values of χ, can be tolerated before phase separation occurs [6]. This is because the entropic contributions to the free energy of mixing are inversely proportional to the degrees of polymerisation. We explore this concept in more detail in sections 2.2.6 and 2.2.7.

2.2.5 Limitations of the Flory-Huggins theory

Limitations of the Flory-Huggins theory are well documented. To contextualise the theory, we outline three limitations below:

- A single lattice is used to describe the distributions of the different constituent species [23]. For this assumption to hold, the volumes and shapes of the constituent species would need to be more or less identical, which is rarely the case in reality.

- The lattice model of mixing does not allow for volume changes upon mixing [41]. Such volume changes have been observed experimentally. If two species have an unfavourable interaction, it may be energetically favourable for the system to lower its density in places to reduce the number of unfavourable contacts.

- The conformations of the polymers are assumed to be random [42]. The effects of energetic interactions, such as van der Waals forces or hydrogen bonds, on the conformations are ignored. Other factors that may affect the conformations include a volume change upon mixing and the local structure of the monomers, which relate to the two limitations above.

Up to a point, one can overcome the limitations of the theory by treating the interaction parameter as an empirical parameter [41]. This is discussed further in section 2.2.8.

We note that the Flory-Huggins theory incorporates numerous simplifying mathematical approximations. However, as noted by Flory [23], the relative significance of these compared with the limitations of the theory, such as those listed above, is small.

2.2.6 Free energy curves

Equation 2.31 is perhaps best interpreted graphically [6, 7]. To illustrate this, we consider a symmetric blend, i.e. $N_A = N_B = N$. In this case, the functional form of $F^{\text{lat}}_{\text{mix,PP}}(\phi)$, where $\phi = \phi_A$, depends on the value of $N\chi$. As shown in figure 2.1, if $N\chi < 2$, the corresponding curves are concave up, while for $N\chi > 2$ they have a double-well structure. The critical value $\chi_c = 2/N$ marks the transition between these two functional forms. We examine the significance of each functional form below.

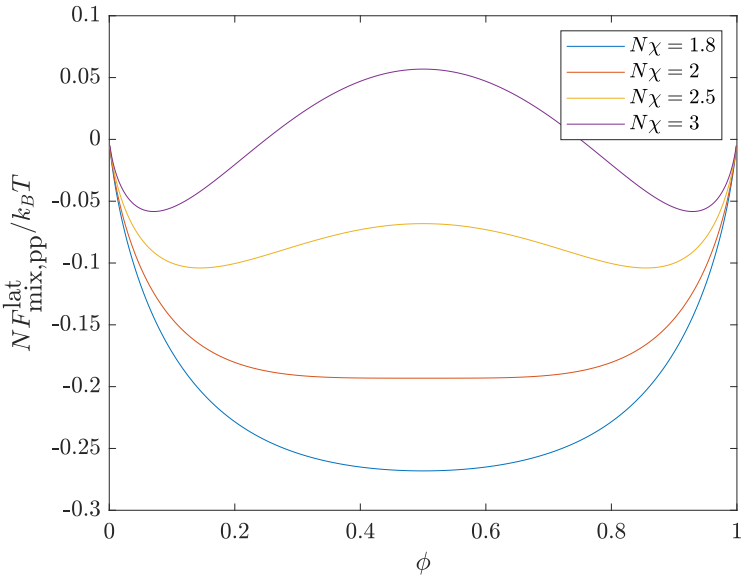

Figure 2.1: The free energy curves corresponding to equation 2.31 with different values of $N\chi$ in the context of a symmetric blend ($N_A = N_B = N$). For $N\chi < 2$, the free energy curves are concave up, while for $N\chi > 2$ they have a double-well structure. The critical value $\chi_c = 2/N$ marks the transition between these two functional forms. Redrawn from [6] with permission from The Licensor through PLSclear. © Oxford University Press 2002.

First, let us denote the volume of the blend as V_0 and the volume fraction of species A within this volume as ϕ_0. Under the assumption of incompressibility, the

volume fraction of species B is $1 - \phi_0$. A phase transition to some unmixed state can be thought of as the formation of two volumes, V_1 and V_2, with volume fractions of A denoted by ϕ_1 and ϕ_2, respectively. These distinct volumes are referred to as phases or phase-separated regions, and the structure formed by two phases is referred to as the phase-separated microstructure. The volume fraction of A (or B) associated with a particular phase is referred to as the composition. Assuming the total volume remains constant, i.e.

$$V_1 + V_2 = V_0, \tag{2.33}$$

and that material is conserved, i.e.

$$V_0\phi_0 = V_1\phi_1 + V_2\phi_2, \tag{2.34}$$

the free energy of an unmixed state per lattice site (relative to the fully unmixed state) is given by

$$F^{\text{lat}}_{\text{sep}} = \frac{V_1}{V_0}F^{\text{lat}}_{\text{mix,PP}}(\phi_1) + \frac{V_2}{V_0}F^{\text{lat}}_{\text{mix,PP}}(\phi_2). \tag{2.35}$$

The value of $F^{\text{lat}}_{\text{sep}}$ can be determined by drawing a straight line between $F^{\text{lat}}_{\text{mix,PP}}(\phi_1)$ and $F^{\text{lat}}_{\text{mix,PP}}(\phi_2)$ and reading off the value on the line at ϕ_0. Figure 2.2 shows two examples of this straight line calculation: one in the context of each free energy functional form.

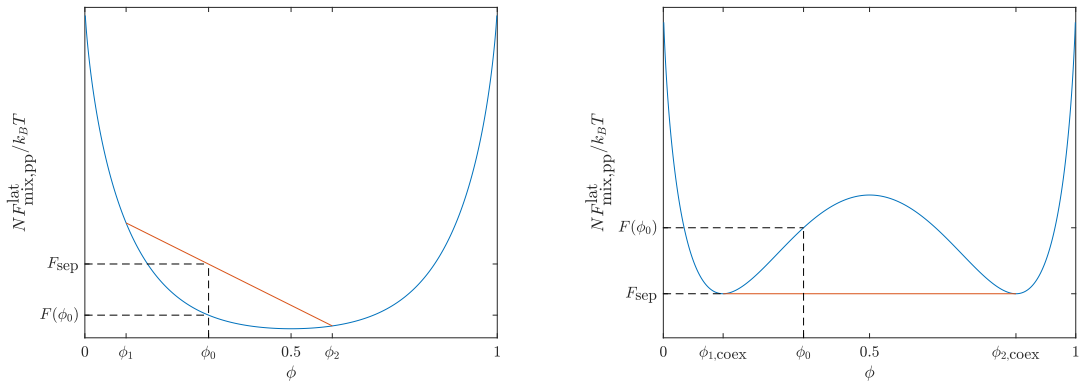

(a) (b)

Figure 2.2: The straight line calculation described beneath equation 2.35 applied to the concave up (a) and the double-well (b) free energy functional forms. We note that $F(\phi_0) \equiv NF^{\text{lat}}_{\text{mix,PP}}(\phi_0)/k_BT$ and $F_{\text{sep}} \equiv NF^{\text{lat}}_{\text{sep}}/k_BT$. In the case of the concave up functional form, one-phase blends of all compositions ϕ_0 are stable - it is always the case that $F^{\text{lat}}_{\text{sep}} > F^{\text{lat}}_{\text{mix,PP}}(\phi_0)$. In the case of the double-well functional form, one-phase blends with compositions $\phi_{1,\text{coex}} < \phi_0 < \phi_{2,\text{coex}}$ are prone to phase-separation since $F^{\text{lat}}_{\text{sep}} < F^{\text{lat}}_{\text{mix,PP}}(\phi_0)$. The compositions corresponding to the minima of the double-well, i.e $\phi_{1,\text{coex}}$ and $\phi_{2,\text{coex}}$, are known as the coexistence compositions - they define the limit of phase separation. Redrawn from [6] with permission from The Licensor through PLSclear.

In the case of the concave up functional form (figure 2.2a), $F^{\text{lat}}_{\text{sep}} > F^{\text{lat}}_{\text{mix,PP}}(\phi_0)$ for all compositions ϕ_0, ϕ_1 and ϕ_2. Therefore, when $N\chi \leq 2$, one-phase blends are stable: phase separation would increase the free energy.

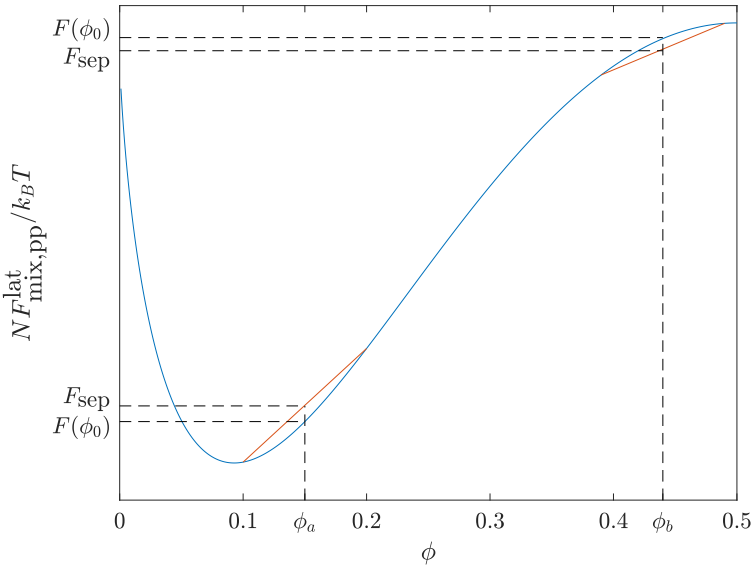

Figure 2.3: A close up view of the double-well free energy functional form with the straight line calculation described beneath equation 2.35 applied in two different regions. We note that $F(\phi_0) \equiv NF^{\text{lat}}_{\text{mix,PP}}(\phi_0)/k_BT$ and $F_{\text{sep}} \equiv NF^{\text{lat}}_{\text{sep}}/k_BT$. Blends with compositions in the concave up region (e.g., ϕ_a) are metastable, while blends in the concave down region (e.g., ϕ_b) are unstable. A metastable blend is stable with respect to small composition fluctuations, which would increase the free energy ($F^{\text{lat}}_{\text{sep}} > F^{\text{lat}}_{\text{mix,PP}}(\phi_a)$), but not large fluctuations. An unstable blend is unstable with respect to small composition fluctuations, which would decrease the free energy ($F^{\text{lat}}_{\text{sep}} < F^{\text{lat}}_{\text{mix,PP}}(\phi_b)$). Redrawn from [6] with permission from The Licensor through PLSclear.

In the case of the double-well functional form (figure 2.2b), $F^{\text{lat}}_{\text{sep}} < F^{\text{lat}}_{\text{mix,PP}}(\phi_0)$ for all compositions $\phi_{1,\text{coex}} < \phi_0 < \phi_{2,\text{coex}}$, where $\phi_{1,\text{coex}}$ and $\phi_{2,\text{coex}}$ - known as the coexistence compositions - are located at the minima of the double well. It follows that, when $N\chi > 2$, one-phase blends with compositions $\phi_{1,\text{coex}} < \phi_0 < \phi_{2,\text{coex}}$ are prone to phase separation. The coexistence compositions define the equilibrium state of the blend and, therefore, the limit of phase separation. To understand how one-phase blends with compositions $\phi_{1,\text{coex}} < \phi_0 < \phi_{2,\text{coex}}$ phase separate, we need to consider the shape of the wells in more detail.

Figure 2.3 shows a close up view of the double-well functional form with the straight line calculation applied in two different regions. In the part of the well that is concave up, meaning it has positive curvature, phase separation into phases with compositions close to ϕ_a would increase the free energy ($F^{\text{lat}}_{\text{sep}} > F^{\text{lat}}_{\text{mix,PP}}(\phi_a)$). Therefore, one-phase blends with compositions in the concave up part of the well are stable with respect to small fluctuations, i.e. small deviations away from ϕ_a. Compositions fluctuations arise due to random thermal fluctuations (Brownian motion). Since the free energy could be lowered by phase separation to the coexistence compositions, one-phase blends with compositions in the concave up part of the well are unstable with respect to large composition fluctuations. Such fluctuations could trigger the nucleation of droplets of the coexistence phases. Once nucleated, these droplets will grow (if the initial radius is greater than or equal to a critical value),

resulting in the formation of different phases. Phase separation via this mechanism, called nucleation and growth, is an activated process since there is an energy barrier associated with the nucleation - further details are provided in section 2.3.1. One-phase blends with compositions in the concave up part of the well are metastable, i.e. they are stable with respect to small composition fluctuations but not large composition fluctuations.

In the part of the well that is concave down in figure 2.3, meaning it has negative curvature, phase separation into compositions close to ϕ_b would decrease the free energy ($F^{\text{lat}}_{\text{sep}} < F^{\text{lat}}_{\text{mix,PP}}(\phi_b)$). Therefore, one-phase blends with compositions in the concave down part of the well are unstable with respect to small composition fluctuations. As a result of this, small composition fluctuations induce a spontaneous and continuous phase transition to an unmixed state. Phase separation via this mechanism, called spinodal decomposition, is spontaneous since there is no energy barrier to the growth of fluctuations. Further details regarding spinodal decomposition are provided in section 2.3.2.

2.2.7 Phase diagrams

The information about the phase behaviour of binary, symmetric polymer blends contained in figures 2.1, 2.2 and 2.3 can be summarised in a phase diagram, which allows one to visualise the state and stability of a blend as a function of the interaction parameter and the composition. The phase diagram of a binary, symmetric polymer blend is shown in figure 2.4. The construction of a phase diagram is rooted in the shape of the free energy curves [6, 7].

The line marking the boundary between the stable and metastable states in figure 2.4, referred to as the coexistence curve, is comprised of the points of common tangent to the free energy curves for which $N\chi > 2$. These points satisfy the condition that the chemical potentials of each phase are equal. Only in the case of symmetric blends can the points of common tangent be determined analytically. Here, the tangent is horizontal and so the points of common tangent correspond to the minima of the free energy curves. These can be located using the condition that $\frac{dF^{\text{lat}}_{\text{mix,PP}}}{d\phi} = 0$. Rearranging for the interaction parameter gives

$$\chi_{\text{coex}} = \frac{1}{N(2\phi - 1)} \ln\left(\frac{\phi}{1-\phi}\right). \tag{2.36}$$

This equation is undefined at $\phi = 0.5$, therefore the condition $\frac{dF^{\text{lat}}_{\text{mix,PP}}}{d\phi} = 0$ only determines the minima at $\phi \neq 0.5$ and not the maximum at $\phi = 0.5$. There are no solutions to $\frac{dF^{\text{lat}}_{\text{mix,PP}}}{d\phi} = 0$ when $N\chi < 2$.

The line marking the boundary between the unstable and metastable states, referred to as the spinodal curve, is comprised of the points of inflection in the free energy curves for which $N\chi > 2$. The points of inflection can be determined using the condition $\frac{d^2F^{\text{lat}}_{\text{mix,PP}}}{d\phi^2} = 0$. Rearranging for the interaction parameter gives

$$\chi_s = \frac{1}{2N\phi(1-\phi)}. \tag{2.37}$$

The point at which the spinodal and coexistence curves meet is called the critical point. This can be determined using the condition $\frac{\partial \chi_s}{\partial \phi} = 0$, which corresponds to

the lowest point on the spinodal curve. The critical point is given by

$$\phi_c = \frac{1}{2}, \chi_c = \frac{2}{N}. \tag{2.38}$$

For $\chi < \chi_c$, blends are stable for any composition. For $\chi > \chi_c$, there is a miscibility gap, meaning not all compositions are stable and therefore phase separation may occur. The miscibility gap becomes larger as N increases, which explains why few polymers with large degrees of polymerisation are miscible. As noted beneath equation 2.31, only slightly unfavourable interactions between unlike pairs of monomers can be tolerated before phase separation occurs.

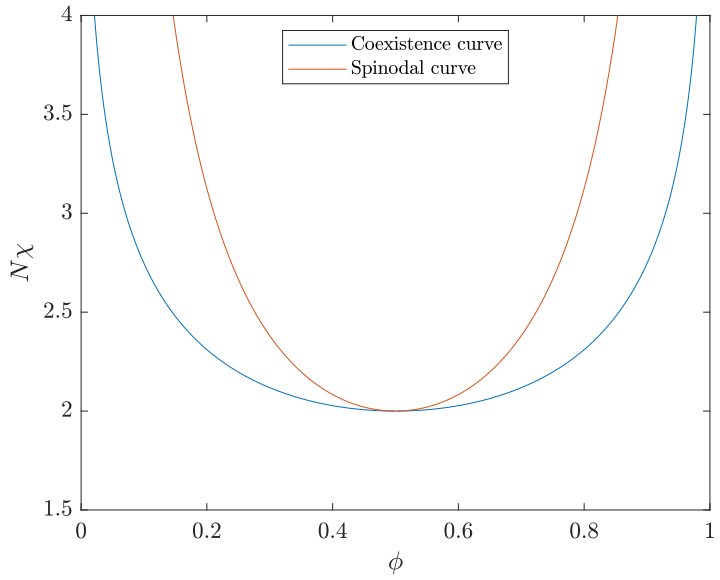

Figure 2.4: The phase diagram of a binary, symmetric ($N_A = N_B = N$) polymer blend with a free energy of mixing described by equation 2.31. One-phase blends of all compositions are stable when $N\chi < 2$. For $N\chi > 2$, there is a miscibility gap, meaning not all compositions are stable and therefore phase separation may occur. The coexistence curve marks the boundary between stable and metastable states, while the spinodal curve marks the boundary between metastable and unstable states. The point at which the spinodal and binodal curves meet is called the critical point. Blends with a given composition can be moved into different regions of the phase diagram by changing χ, i.e. the temperature. Inside the spinodal curve, the mechanism of phase separation is spinodal decomposition, which is a spontaneous process. Inside the region marked by the coexistence curve and the spinodal curve, the mechanism of phase separation is nucleation and growth, which is an activated process. Redrawn from [6] with permission from The Licensor through PLSclear.

2.2.8 The interaction parameter, χ

The interaction parameter derived as part of the Flory-Huggins theory is purely energetic in origin. It has a temperature dependence of T^{-1}. This suggests that phase separation occurs when the temperature is lowered. Blends that exhibit this

behaviour are said to have an upper critical solution temperature. However, experiments have shown that many blends have a lower critical solution temperature, i.e. phase separation occurs when the temperature is increased [7]. Based on this evidence, the interaction parameter must have a different temperature dependence to simply T^{-1}.

It has been shown that the interaction parameter is not purely energetic in origin [7]. Instead, it includes an entropic contribution. This entropic contribution is attributed to a non-combinatorial entropy, which may arise from the effects of energetic interactions on the conformations of the polymers [42], for example.

In practice, the interaction parameter is often treated as an empirical parameter [7, 41]:

$$\chi = a + \frac{b}{T}, \tag{2.39}$$

where a encapsulates the entropic contribution and b encapsulates the energetic contribution. This empirical form can capture both upper and lower critical solution temperature behaviour. Experiments have shown that the interaction parameter often also depends on the composition [41]. This can be accounted for by using a more complex empirical equation for the interaction parameter than equation 2.39.

Treating the interaction parameter as an empirical parameter allows one to overcome some of the limitations of the Flory-Huggins theory. The ability to treat the interaction parameter as an empirical parameter is one of the main reasons for the sustained, wide-spread use of the Flory-Huggins theory. Despite its shortcomings, the theory is a convenient parametrisation of the free energy [41].

2.3 Mechanisms of phase separation and dissolution in polymer blends

As mentioned in section 2.2.6, there are two mechanisms by which a polymer blend can phase separate: nucleation and growth and spinodal decomposition. When a phase-separated blend is brought back into the one-phase region, the phase-separated structure will dissipate in a process called dissolution. In this thesis, we are primarily concerned with thermally-induced spinodal decomposition and dissolution. Therefore, our discussion of nucleation and growth is minimal.

2.3.1 Nucleation and growth

Nucleation and growth [6, 7] occurs when a blend lies in the metastable region of the phase diagram. Here, the blend is stable with respect to small composition fluctuations but not large composition fluctuations, which could trigger the nucleation of droplets of one of the coexistence phases. If the nucleated droplets have a radius greater than some critical value, they will grow. Otherwise, they will dissipate. The critical radius requirement stems from the fact that there is a free energy barrier associated with the formation of droplets - this is explained by classical nucleation theory, which we outline below.

When a droplet of one of the coexistence phases is nucleated, there are two contributions to the net change in the free energy of the blend, one positive and one negative. The negative contribution stems from the fact that the droplet phase

has a lower free energy per unit volume than the metastable phase. The positive contribution stems from unfavourable interactions between A and B molecules at the interface of the droplet and an entropy cost due to the interface restricting the number of configurations a polymer can adopt. Combining the positive and negative contributions, the net change in the free energy of a blend associated with the formation of a droplet of radius r can be written as [6]

$$\Delta F(r) = \frac{4}{3}\pi r^3 \Delta F_v + 4\pi r^2 \gamma, \tag{2.40}$$

where ΔF_v is the negative free energy change per unit volume and γ is the interfacial energy per unit area.

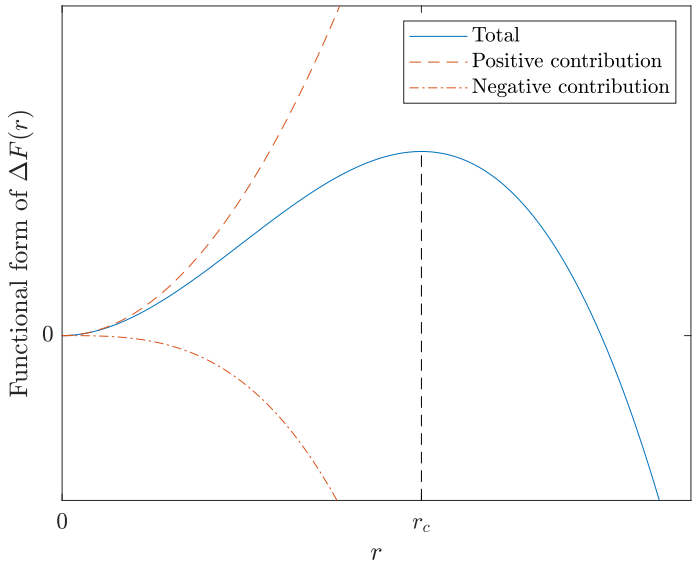

Figure 2.5: The functional form of the net change in the free energy of a polymer blend associated with forming a droplet of one of the coexistence phases, $\Delta F(r)$, during nucleation and growth. The net change in the free energy balances two opposing contributions, which are plotted. The negative contribution stems from the fact that droplets of the coexistence phases have a lower free energy per unit volume than droplets of the metastable phase. The positive contribution is associated with the formation of an energetically unfavourable interface. Redrawn from [7] with permission from Springer Nature.

Figure 2.5 shows a plot of equation 2.40. The net change in the free energy is maximum at r_c, which corresponds to the critical radius. Droplets with radius $r < r_c$ will dissipate since they would increase the free energy of the blend if they were to grow. Conversely, droplets with radius $r > r_c$ will grow, leading to a reduction in the free energy of the blend. The critical radius can be calculated from the condition $\frac{d\Delta F(r)}{dr} = 0$. The result is

$$r_c = \frac{-2\gamma}{\Delta F_v}. \tag{2.41}$$

Therefore, the energy barrier to forming a critical nucleus is given by

$$\Delta F_c = \frac{16\pi\gamma^3}{3\Delta F_v^2}. \tag{2.42}$$

The probability of a fluctuation overcoming the energy barrier, and therefore the rate of nucleation, is proportional to the Boltzmann factor, i.e. $\exp(-\Delta F_c/k_B T)$.

The phase-separated microstructure of a blend undergoing nucleation and growth is characterised by dispersed droplets, which grow in time [10, 43].

2.3.2 Spinodal decomposition and dissolution

Spinodal decomposition [6, 7] occurs when a blend lies in the unstable region of the phase diagram. Here, the blend is unstable with respect to small fluctuations in the composition. As a result of this, small composition fluctuations induce a spontaneous and continuous phase transition to an unmixed state. The process of dissolution [8, 9] is essentially the inverse of spinodal decomposition - there is a spontaneous and continuous phase transition from an unmixed state to the mixed state. The unmixed state can be obtained by either spinodal decomposition or nucleation and growth.

Spinodal decomposition can be described in terms of a three stage model [6, 44]:

- Early stage. Phase-separated regions begin to form as a result of the spontaneous amplification of composition fluctuations. Polymers move from regions of low concentration to regions of high concentration. Fluctuations with a particular, optimal, wavelength grow fastest. This wavelength can be regarded as the characteristic length of the system. Fluctuations with wavelengths greater than the characteristic length grow too slowly because of the large distances over which the polymers must diffuse. The free energy cost associated with composition gradients (interfaces) suppresses the growth of fluctuations with wavelengths smaller than the characteristic length - such fluctuations would create too much interface.

- Intermediate stage. Fluctuations with different wavelengths begin to couple and the characteristic length of the system increases - this has the effect of reducing the interfacial energy. During the early stage, it is hard to distinguish between phase-separated regions and the interfaces. However, during the intermediate stage, the two become distinguishable. There are now two important lengths: the characteristic length, which is correlated with the average size of the phase separated regions, and the interfacial width. The compositions of the developing, coarsening phase-separated regions tend towards the coexistence values. The initially diffuse interfaces begin to sharpen.

- Late stage. The interfacial width is more or less constant. The characteristic length continues to increase, i.e. the phase-separated regions continue to coarsen. The characteristic length is once again the single time-evolving length.

Figure 2.6 illustrates the above stages pictorially.

A symmetric binary blend is referred to as critical if $\phi_0 = \phi_c = 0.5$, i.e. the mixing ratio of the constituent species is 1:1. Otherwise, the blend is referred to

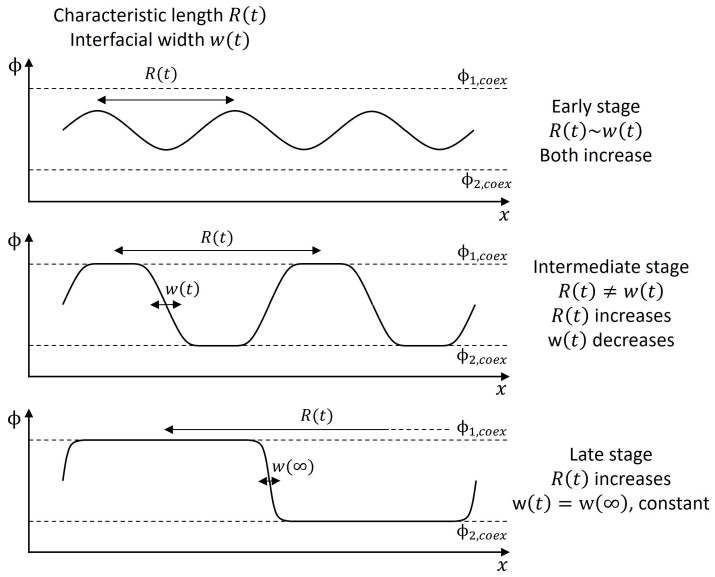

Figure 2.6: A schematic diagram of the three stage model of spinodal decomposition highlighting how the composition profiles and important length scales evolve. Redrawn from [6] with permission from The Licensor through PLSclear. © Oxford University Press 2002.

as off-critical. The phase-separated microstructure resulting from spinodal decomposition depends on the volume fraction ratio of the coexistence phases [11]. In general, the phase-separated microstructure of a critical blend undergoing spinodal decomposition is characterised by a random, co-continuous pattern, which coarsens over time [6, 10, 11]. The pattern is random since it is initiated by composition fluctuations caused by random thermal fluctuations. At a given point in time, the widths of different regions of the co-continuous microstructure will be more or less uniform. This is a result of the blend having a characteristic length scale. The phase-separated microstructure of an off-critical blend undergoing spinodal decomposition is usually characterised by dispersed droplets, which grow in time [10, 11]. We note that examples of the time evolution of co-continuous and dispersed droplet microstructures during spinodal decomposition are shown in figure 1.1.

2.3.3 Cahn-Hilliard-Cook theory

Perhaps the most commonly used and successful theory for describing the time evolution of spinodal decomposition and dissolution in polymer blends is the Cahn-Hilliard-Cook Flory-Huggins-de Gennes (CHC-FHdG) theory [23–26]. This is an extension of a theory called the Cahn-Hilliard-Cook (CHC) theory [20–22, 45, 46], which applies to small molecule mixtures. To illustrate the key ideas underpinning the CHC-FHdG theory, we first outline the CHC theory [20–22, 45, 46].

The key idea behind the CHC theory is that a generalised diffusion equation can be used to describe both spinodal decomposition and dissolution. We note that the theory assumes a coarse grained version of the lattice adopted in the regular solution and Flory-Huggins theories [30]. A natural order parameter for this lattice is the local volume fraction of one of the constituent species:

$$\phi(\boldsymbol{r}) = \frac{v_0}{L^3} \sum_{i \in \text{cell}} c_i, \tag{2.43}$$

where 'cell' refers to a coarse-graining volume with side length L centred on $\boldsymbol{r}$ and the value of c_i depends on whether a lattice site within the cell contains a molecule of A or not. Specifically, $c_i = 1$ if a molecule of A is present and $c_i = 0$ otherwise. The value of L must be large in comparison to the lattice spacing to facilitate a continuum description of the mixture while also small in comparison with the wavelengths of the composition fluctuations [30]. To derive a generalised diffusion equation, we begin with the following continuity equation:

$$\frac{\partial \phi(\boldsymbol{r}, t)}{\partial t} = -\nabla \cdot \boldsymbol{J}, \tag{2.44}$$

where $\boldsymbol{J}$ is the flux of material. The flux is defined by a generalised version of Fick's first law:

$$\boldsymbol{J} = -M \nabla (\mu_A - \mu_B), \tag{2.45}$$

where M is the mobility and $\mu_A - \mu_B$ is the exchange chemical potential per unit volume, which we denote as μ. The mobility relates the response of the flux to gradients in the exchange chemical potential. For simplicity, we take M to be constant. In reality, M is often found to be dependent on the local composition [17, 30]. The exchange chemical potential describes how the free energy changes with the composition. Accounting for the fact that ϕ will vary in time and space, we use the following definition

$$\mu \equiv \mu_A - \mu_B = \frac{\delta F\{\phi(\boldsymbol{r}, t)\}}{\delta \phi}, \tag{2.46}$$

where F is the free energy of the system, expressed as a functional, i.e. a function that depends on the functional form of $\phi(\boldsymbol{r}, t)$, and $\delta / \delta \phi$ represents the functional derivative with respect to ϕ. We note that $\boldsymbol{J}$, M and μ do not have 'typical' dimensions because of how equations 2.44 - 2.46 have been formulated. Since equation 2.44 is a continuity equation in terms of the volume fraction rather than the concentration, $\boldsymbol{J}$ has dimensions of LT^{-1} instead of the usual $L^{-2}T^{-1}$. As will become clear, since μ is defined in terms of a functional derivative, it has dimensions of [energy]L^{-3} instead of [energy]. From the dimensions of $\boldsymbol{J}$ and μ, it follows that M has dimensions of $L^5 T^{-1}$[energy]$^{-1}$ instead of $L^2 T^{-1}$ [2].

Combining equations 2.44-2.46 yields a modified diffusion equation capable of describing diffusion both along and against a composition gradient, i.e. dissolution and spinodal decomposition, respectively, subject to the formulation of F:

$$\frac{\partial \phi(\boldsymbol{r}, t)}{\partial t} = M \nabla^2 \frac{\delta F\{\phi(\boldsymbol{r}, t)\}}{\delta \phi}. \tag{2.47}$$

Both dissolution and spinodal decomposition involve phase-separated microstructures. An essential component of phase-separated systems is the interface between the phases. Indeed, the interfacial energy must be accounted for when calculating the free energy of the system. Under the assumption that the free energy of a region of a heterogeneous system will depend both on the local composition and the composition of the immediate environment, Cahn and Hilliard proposed the following phenomenological form of the free energy functional [20]:

$$\frac{F\{\phi(\boldsymbol{r},t)\}}{k_BT} = \int_V d^3r \left(\frac{f(\phi(\boldsymbol{r},t))}{k_BT} + \kappa(\nabla\phi(\boldsymbol{r},t))^2\right), \tag{2.48}$$

where f is the free energy density of some small homogeneous region around $\boldsymbol{r}$ and κ is the 'square gradient coefficient'. The integrand approximates the free energy density of an infinitesimal region of the mixture as the sum of two contributions. The first contribution is the free energy density that the region would have if it was homogeneous. The second contribution is due to the interface. These contributions are the leading terms in a generalised Taylor expansion of the free energy density of a heterogeneous mixture. Therefore, the interface contribution can be thought of as the lowest order correction to the homogeneous free energy density required to describe a heterogeneous system.

In the case of a regular solution, we can substitute the following into equation 2.48 [20]:

$$f(\phi(\boldsymbol{r},t)) = \frac{F^{\text{lat}}_{\text{mix,RS}}(\phi(\boldsymbol{r},t))}{v_0} \tag{2.49a}$$

$$\kappa = \frac{\chi\lambda^2}{v_0}, \tag{2.49b}$$

where λ is the interaction distance between molecules. We note that $F^{\text{lat}}_{\text{mix,RS}}$ is the regular solution free energy of mixing per lattice site given by equation 2.20. The square gradient coefficient is purely energetic in origin. As a result of composition gradients, molecules will sense a different number of like and unlike molecules in their environment than the local composition would indicate. There is no entropic part to the square gradient coefficient since the combinatorial entropy depends solely on the local composition and so it is captured by $f(\phi(\boldsymbol{r},t))$.

The functional derivative of equation 2.48 is given by [47]

$$\frac{\delta F\{\phi(\boldsymbol{r},t)\}}{\delta\phi} = \frac{\partial f(\phi)}{\partial\phi} - 2\kappa k_BT\nabla^2\phi. \tag{2.50}$$

Upon substituting equations 2.49a and 2.49b into equation 2.50, we obtain, after some calculations,

$$\frac{\delta F\{\phi(\boldsymbol{r},t)\}}{\delta\phi} = \frac{k_BT}{v_0}\big(\ln(\phi) - \ln(1-\phi) + (1-2\phi)\chi - 2\chi\lambda^2\nabla^2\phi\big). \tag{2.51}$$

Combining equations 2.47 and 2.51 yields the Cahn-Hilliard equation for small molecule mixtures

$$\frac{\partial\phi(\boldsymbol{r},t)}{\partial t} = \frac{Mk_BT}{v_0}\nabla^2(\ln(\phi) - \ln(1-\phi) - 2\chi\phi - 2\chi\lambda^2\nabla^2\phi). \tag{2.52}$$

A major shortcoming of the Cahn-Hilliard equation is that it is deterministic. It neglects the effects of thermal fluctuations (Brownian motion), which give rise to composition fluctuations - the essential ingredient for initiating spinodal decomposition. Cook rectified this problem by including a stochastic term $\xi(\boldsymbol{r},t)$ to model the composition fluctuations [22]. The resulting equation, called the Cahn-Hilliard-Cook equation, is given by

$$\frac{\partial\phi(\boldsymbol{r},t)}{\partial t} = \frac{Mk_BT}{v_0}\nabla^2(\ln(\phi) - \ln(1-\phi) - 2\chi\phi - 2\chi\lambda^2\nabla^2\phi) + \xi(\boldsymbol{r},t). \tag{2.53}$$

The noise is assumed to have a Gaussian distribution described by the following moments [17, 22, 30]:

$$< \xi(\boldsymbol{r},t) > = 0 \tag{2.54a}$$
$$< \xi(\boldsymbol{r},t)\xi(\boldsymbol{r}',t') > = B\delta(\boldsymbol{r}-\boldsymbol{r}')\delta(t-t'), \tag{2.54b}$$

where B is an operator - the form of which ensures any change in $\phi(\boldsymbol{r},t)$ due to $\xi(\boldsymbol{r},t)$ is balanced by the correct flux. In other words, B ensures no material is created or destroyed. To determine B, it is assumed that the system will evolve to its equilibrium state over a sufficiently long time period. Non-linear Langevin equations, such as equation 2.53, are hard to solve analytically. The most practical approach to deal with them is to construct the corresponding Fokker-Planck equation, which describes the time evolution of the probability distribution of the order parameter [48, 49]:

$$\frac{\partial P(\{\phi(\boldsymbol{r})\},t)}{\partial t} = \int d^3r \frac{\delta}{\delta\phi}\Big[- M\nabla^2\frac{\delta F}{\delta\phi}P + \frac{B}{2}\frac{\delta P}{\delta\phi}\Big]. \tag{2.55}$$

As $t \to \infty$, the solution approaches the equilibrium solution. Equilibrium thermodynamics tells us this should be a Boltzmann distribution, therefore [48]

$$B = -2Mk_BT\nabla^2. \tag{2.56}$$

Specifically, it is the factor of ∇^2 in B that ensures material is conserved. We discuss this point further in appendix A - see equation A.7 and the text beneath it.

2.3.4 Cahn-Hilliard-Cook Flory-Huggins de Gennes theory

We are now in a position to turn our attention to polymer blends. For simplicity, we assume equal 'lattice' degrees of polymerisation and Kuhn (statistical segment) lengths [6, 40], i.e. $N_A = N_B = N$ and $\sigma_A = \sigma_B = \sigma$, respectively.

To extend the Cahn-Hilliard-Cook equation to polymer blends, de Gennes modified the Cahn-Hilliard free energy functional [25]. Specifically, he proposed setting

$$f(\phi(\boldsymbol{r},t)) = \frac{F^{\text{lat}}_{\text{mix,PP}}(\phi(\boldsymbol{r},t))}{v_0} \tag{2.57}$$

and modifying the square gradient coefficient to become

$$\kappa(\phi(\boldsymbol{r},t)) = \frac{\chi\lambda^2}{v_0} + \frac{1}{36v_0}\Big[\frac{\sigma^2}{\phi(\boldsymbol{r},t)} + \frac{\sigma^2}{1-\phi(\boldsymbol{r},t)}\Big]. \tag{2.58}$$

We note that $F^{\text{lat}}_{\text{mix,PP}}$ is the Flory-Huggins free energy of mixing per lattice site given by equation 2.31. The square-gradient coefficient is comprised of two contributions: one purely energetic in origin, i.e. $\chi\lambda^2/v_0$, and the other entropic. The former was discussed above in the context of small molecule mixtures. In the case of polymer

blends, λ is the interaction distance between monomers. The entropic contribution captures costs to the free energy due to the formation of composition gradients, which impose constraints on the number of configurations available to the polymers in the blend [6]. De Gennes derived the exact form of equation 2.58 to be consistent with his random phase approximation for the static structure factor in one-phase blends [50, 51], which we discuss in section 2.4.9. Often it is found that the entropic contribution to the square gradient coefficient is much larger than the energetic contribution, therefore the energetic contribution is often neglected in the treatment of polymer blends [25, 26]. We adopt this convention.

As well as the modifications mentioned above, De Gennes suggested that the connectivity of polymers manifests itself in a non-local relation between the polymer flux and the gradient of the exchange chemical potential [25]:

$$\boldsymbol{J}(\boldsymbol{r}) = -\int d^3r \frac{\Lambda(\boldsymbol{r}-\boldsymbol{r}')}{k_BT}\nabla\mu(\boldsymbol{r}'), \tag{2.59}$$

where $\Lambda(\boldsymbol{r}-\boldsymbol{r}')$ is an Onsager coefficient. This equation states that the flux at a given point depends on its environment because of the connectivity. When considering length scales larger than the chain scale, one may consider a local relation similar to equation 2.45 instead of equation 2.59 [52]. For simplicity, we set $\Lambda(\boldsymbol{r}-\boldsymbol{r}') = k_BTM\delta(\boldsymbol{r}-\boldsymbol{r}')$ [26], which recovers equation 2.45 exactly when substituted into equation 2.59.

In the case of a square gradient coefficient that depends on ϕ, the functional derivative of equation 2.48 is given by [47]

$$\frac{\delta F\{\phi(\boldsymbol{r},t)\}}{\delta\phi} = \frac{\partial f(\phi)}{\partial\phi} - k_BT\frac{\partial\kappa(\phi)}{\partial\phi}(\nabla\phi)^2 - 2k_BT\kappa(\phi)\nabla^2\phi. \tag{2.60}$$

Upon substituting equations 2.57 and 2.58 into equation 2.60, we obtain, after some calculations,

$$\begin{aligned}\frac{\delta F\{\phi(\boldsymbol{r},t)\}}{\delta\phi} = \frac{k_BT}{v_0}\Big[&\frac{1}{N}\ln(\phi) - \frac{1}{N}\ln(1-\phi) + \chi(1-2\phi)\\ &- \frac{\sigma^2}{18}\Big(\frac{1}{\phi(1-\phi)}\Big)\nabla^2\phi + \frac{\sigma^2}{36}\Big(\frac{1-2\phi}{(\phi(1-\phi))^2}\Big)(\nabla\phi)^2\Big].\end{aligned} \tag{2.61}$$

Combining equations 2.47 and 2.61 and accounting for composition fluctuations with a stochastic term yields the CHC-FHdG equation for polymer blends:

$$\begin{aligned}\frac{\partial\phi(\boldsymbol{r},t)}{\partial t} = \frac{Mk_BT}{v_0}\nabla^2\Big[&\frac{1}{N}\ln(\phi) - \frac{1}{N}\ln(1-\phi) - 2\chi\phi\\ &- \frac{\sigma^2}{18}\Big(\frac{1}{\phi(1-\phi)}\Big)\nabla^2\phi + \frac{\sigma^2}{36}\Big(\frac{1-2\phi}{(\phi(1-\phi))^2}\Big)(\nabla\phi)^2\Big] + \xi(\boldsymbol{r},t).\end{aligned} \tag{2.62}$$

In its current form, equation 2.62 can only be solved numerically. To make it analytically tractable, we must linearise it [25, 26]. Upon making the substitution $\phi(\boldsymbol{r},t) = \phi_0 + \delta\phi(\boldsymbol{r},t)$, where ϕ_0 is the average (overall) volume fraction and $\delta\phi$ is a fluctuation, performing a power series expansion and neglecting all non-linear terms in $\delta\phi(\boldsymbol{r},t)$, we obtain

$$\frac{\partial \delta\phi(\boldsymbol{r},t)}{\partial t} = \frac{Mk_BT}{v_0}\Big[2(\chi_s-\chi)\nabla^2\delta\phi - \frac{\sigma^2}{18}\Big(\frac{1}{\phi_0(1-\phi_0)}\Big)\nabla^4\delta\phi\Big] + \xi(\boldsymbol{r},t), \quad (2.63)$$

where $\chi_s = \frac{2}{4N\phi_0(1-\phi_0)}$ is the value of the interaction parameter on the spinodal. We refer to equation 2.63 as the linear CHC-FHdG equation. It is valid for small $\delta\phi$. Therefore, in the case of dissolution, we expect the linear CHC-FHdG equation to be valid when the composition fluctuations are small from the beginning of the process [8, 31], which depends on how developed the initial phase-separated microstructure is. In the case of spinodal decomposition, we expect the linear CHC-FHdG equation to be valid during the early stage, i.e. when the composition fluctuations are small [8, 45]. Upon comparing equation 2.63 with Fick's second law, we can identify the mutual diffusion coefficient of the blend as [2]

$$D = \frac{2Mk_BT(\chi_s-\chi)}{v_0}. \quad (2.64)$$

In the case of dissolution, D is positive. Therefore, diffusion occurs along the composition gradient, which leads to mixing. In the case of spinodal decomposition, D is negative. Therefore, diffusion occurs against the composition gradient, or 'uphill', which leads to phase separation.

The solution to equation 2.63 without noise is given by [45]

$$\delta\phi(\boldsymbol{r},t) = \sum_{\boldsymbol{q}} \exp(R(q)t)(A(\boldsymbol{q})\cos(\boldsymbol{q}\cdot\boldsymbol{r}) + B(\boldsymbol{q})\sin(\boldsymbol{q}\cdot\boldsymbol{r})), \quad (2.65)$$

where A and B are the initial amplitudes of the composition fluctuations present in the sample, and

$$R(q) = -\frac{Mk_BT}{v_0}\Big[2(\chi_s-\chi)q^2 + \frac{\sigma^2}{18}\Big(\frac{1}{\phi_0(1-\phi_0)}\Big)q^4\Big] \quad (2.66)$$

is a q-dependent amplification factor. The symbol q denotes the wavenumber of a composition fluctuation, which is related to the the wavelength via $\lambda = \frac{2\pi}{q}$.

The functional form of $R(q)$ is shown in figure 2.7 for both dissolution and spinodal decomposition. In the case of dissolution, $R(q)$ is negative for all values of q, which means composition fluctuations of all wavelengths decay. In the case of spinodal decomposition, $R(q)$ is positive for $q < q_c$ and negative for $q > q_c$, where q_c is the critical wavenumber at which $R(q) = 0$. This means that composition fluctuations with wavelengths $\lambda > \frac{2\pi}{q_c}$ will grow, while those with wavelengths $\lambda < \frac{2\pi}{q_c}$ will decay. Composition fluctuations with a wavelength $\lambda_m = \frac{2\pi}{q_m}$ will grow fastest, where $q = q_m$ is the wavenumber at which $R(q)$ is maximum. The wavelength λ_m corresponds to the initial value of the characteristic length scale of the blend during the early stage of spinodal decomposition.

The linear CHC-FHdG equation has been shown to quantitatively capture the early stage of spinodal decomposition in polymer blends [2, 27, 28, 30]. Beyond the early stage, the non-linear CHC-FHdG equation qualitatively captures the dynamics of the process [45, 53]. For example, it captures coarsening and can be used to generate simulated morphologies that are representative of spinodal decomposition.

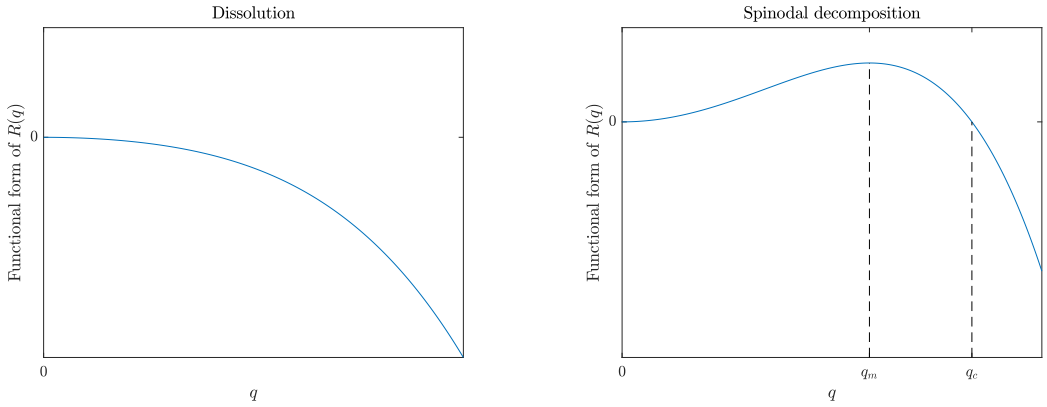

(a) (b)

Figure 2.7: The functional form of the amplification factor, $R(q)$, in the case of (a) dissolution and (b) spinodal decomposition. In dissolution, $R(q)$ is negative for all values of the wavenumber q. In spinodal decomposition, $R(q)$ is positive for $0 < q < q_c$ and negative for $q > q_c$, where q_c is the critical wavenumber at which $R(q) = 0$. The maximum value of $R(q)$ occurs at $q = q_m$. Redrawn from [6] with permission from The Licensor through PLSclear.

2.3.5 Limitations of the Cahn-Hilliard-Cook Flory-Huggins-de Gennes theory

To contextualise the CHC-FHdG theory, we outline three limitations below:

- In equation 2.48, composition gradients are assumed to be shallow [20, 30]. This assumption holds near the critical point and limits the range of systems for which the theory is valid.
- The effects of hydrodynamics are neglected [54]. Generally, hydrodynamic effects - induced by the interfacial tension between phase-separated regions - become important during the late stage of spinodal decomposition. They play an important role in coarsening.
- The composition dependence of the mobility is not fully understood [2,55]. To apply the theory, one must make assumptions about the mobility, which may undermine the validity of the theory.

Another limitation of the theory is that equation 2.62 cannot be solved analytically. This complicates the analysis of experimental data. Furthermore, calculating the numerical solution to the non-linear equation often requires a lot of computing power [47, 53, 56].

2.4 Small-angle scattering

Small-angle scattering experiments are often used to monitor the time evolution of composition fluctuations, i.e. the development of the microstructure, in polymer blends [2, 15, 16, 29]. A small-angle scattering experiment can be described in terms of three steps [15, 16]:

- Radiation, typically in the form of X-rays or neutrons, is fired at a sample.
- The radiation interacts with the sample, causing the radiation to scatter.
- The intensity of the scattered radiation (structure factor) is measured as a function of the scattering angle or magnitude of the scattering vector.

We note that a schematic of a small-angle scattering experiment in the context of a polymer blend undergoing spinodal decomposition is shown in figure 1.2.

One can learn about the microstructure by analysing the structure factor [2, 15, 16, 57]. For example, in the case of spinodal decomposition, the characteristic length can be determined from the peak. The structure factor is essentially the power spectrum of the composition fluctuations, i.e. the product of the Fourier transform with its complex conjugate. It is not possible to obtain full knowledge of the microstructure from the structure factor.

Small-angle scattering is used to measure relatively large structures, i.e. structures on a scale of roughly $10 - 100$ nm when X-rays or neutrons are scattered and $100 - 1000$ nm when light is scattered [15, 16, 29]. The reciprocity between lengths in real space and Fourier space means that information relating to structures on these scales is contained in the part of the structure factor corresponding to small scattering angles, hence the name small-angle scattering.

X-rays and neutrons are well suited to probing the structure of materials since they have wavelengths around 1 Å, which is of a similar magnitude to typical interatomic spacings [15, 16]. In what follows, we specialise to small-angle neutron scattering. A benefit of small-angle neutron scattering over small-angle X-ray scattering is that the strength of neutron-nuclei interactions varies in a seemingly random way with the atomic number [15, 16]. The strength of X-ray-electron interactions increases with the atomic number. Therefore, neutrons are sensitive to as many light elements as they are heavy elements. X-rays, on the other hand, struggle to detect light elements. Furthermore, deuterium and hydrogen interact very differently with neutrons. This opens the door to deuterium labelling, in which deuterium can be substituted for hydrogen in specific molecules to highlight them [15, 16].

2.4.1 Scattering off a single particle

We wish to derive the key equations describing the scattering of neutrons off a polymer blend. To do this, we follow the treatment in [16]. We note that another good source of information on the subject is [15].

First, we consider the simple case of scattering off a single particle, which allows us to introduce and define some key terms. Figure 2.8 shows a schematic of the scattering off a single particle. A plane wave is incident on the particle. The flux of the wave, i.e. the energy transferred per unit area per second, is denoted $\boldsymbol{J}_0$. The incident plane wave scatters off the point particle as a spherical wave. We assume that the detector is placed far enough away that the scattered wave appears as a plane wave, although its amplitude will have decreased inversely proportionally to R, the distance between the particle and the detector. To ensure that the flux of the scattered wave, $\boldsymbol{J}$, is independent of R, it is defined slightly differently to $\boldsymbol{J}_0$, namely as the energy transferred per unit solid angle per second. Fluxes are proportional to the square of the wave amplitude, denoted A in the case of $\boldsymbol{J}$ (or A_0 in the case of $\boldsymbol{J}_0$):

$$\boldsymbol{J} = |A|^2 = AA^*. \tag{2.67}$$

The detector measures a quantity called the differential cross section,

$$\frac{d\sigma}{d\Omega} = \frac{\boldsymbol{J}}{\boldsymbol{J}_0}, \tag{2.68}$$

which can be thought of as the number of particles scattered into a unit solid angle in a given direction per second divided by the number of particles fired at the sample per unit area per second. Indeed, the differential cross section is a function of the scattering angle. From now on, we refer to the differential cross section as the intensity.

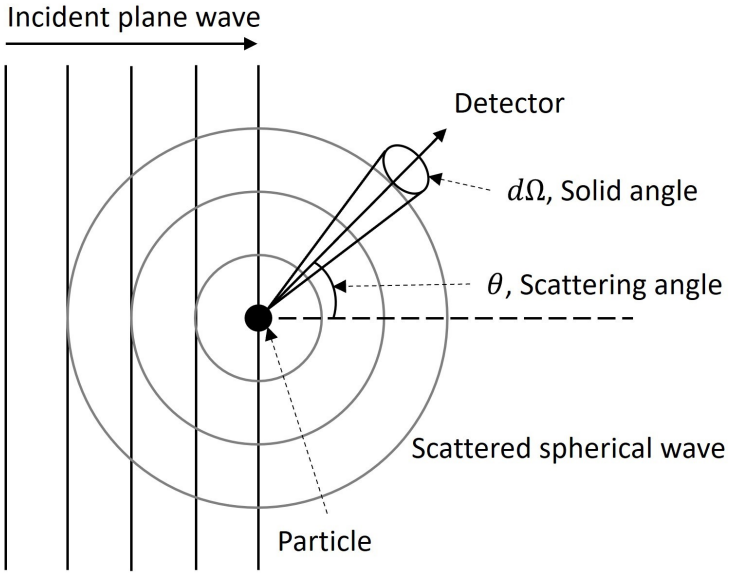

Figure 2.8: The basic geometry of a scattering experiment in the context of scattering off a single particle. Redrawn from [16] with permission from The Licensor through PLSclear. © Oxford University Press 2000.

2.4.2 Scattering off two particles

Adding a layer of complexity, we now consider the scattering off two particles. This situation is shown in figure 2.9. The incident plane wave propagates along the z-axis with wavevector $\boldsymbol{q}_i$ and scatters off the particles situated at O and B. Given that it has frequency f and wavelength λ, the amplitude of the incident plane wave is given by

$$A(x, y, z, t) = A_0 \cos\left(2\pi\left(ft - \frac{z}{\lambda}\right)\right) \tag{2.69a}$$

$$= A_0 \cos(\omega t - q_i z), \tag{2.69b}$$

where z is the position of the plane wave along the z-axis. In complex notation, which is helpful for the ensuing maths, the amplitude is given by

$$A(x, y, z, t) = A_0 \exp(i(\omega t - q_i z)), \tag{2.70}$$

where the real part recovers the original equation.

A detector is situated far away from the particles. We assume the scattering is coherent and elastic. The scattered wave emanating away from B has to travel further to the detector than the one emanating from O. This results in there being a phase difference at the detector, which gives rise to interference. The phase difference is given by

$$\delta\varphi = \frac{2\pi}{\lambda}(|AB| - |OC|) \tag{2.71a}$$

$$= (\boldsymbol{q} \cdot \boldsymbol{r}_{OB}), \tag{2.71b}$$

where $|AB| = \left(\frac{\boldsymbol{q}_i}{|\boldsymbol{q}_i|} \cdot \boldsymbol{r}_{OB}\right)$, $|OC| = \left(\frac{\boldsymbol{q}_f}{|\boldsymbol{q}_f|} \cdot \boldsymbol{r}_{OB}\right)$ and $\boldsymbol{q} = \boldsymbol{q}_i - \boldsymbol{q}_f$. The latter quantity is referred to as the scattering vector. It is related to the scattering angle via

$$|\boldsymbol{q}| = q = \frac{4\pi}{\lambda} \sin\left(\frac{\theta}{2}\right). \tag{2.72}$$

We note that the relationship between $\boldsymbol{q}_i$, $\boldsymbol{q}_f$ and $\boldsymbol{q}$ is shown in the bottom right of figure 1.2.

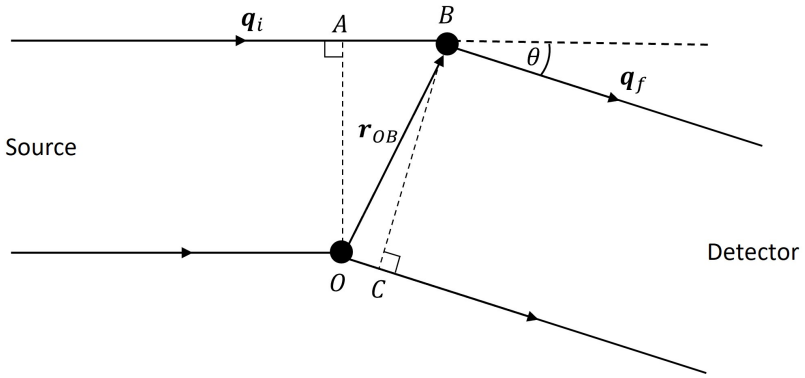

Figure 2.9: The scattering of a plane wave off two particles. The scattered wave emanating from the particle B has to travel further to the detector than the scattered wave emanating from O. This results in there being a phase difference at the detector, which gives rise to interference. Redrawn from [16] with permission from The Licensor through PLSclear. © Oxford University Press 2000.

The amplitude of the scattered spherical wave emanating from O can be written as

$$A_1(x, y, z, t) = A_0 b \exp(i(\omega t - q_i z)), \tag{2.73}$$

where A_0 is the amplitude of the incident plane wave and b is the scattering length, which describes the strength of the neutron-nucleus interaction. Similarly, the scattered spherical wave emanating from B can be written as

$$A_2(x, y, z, t) = A_0 b \exp(i(\omega t - q_i z)) \exp(-i\boldsymbol{q} \cdot \boldsymbol{r}_{OB}). \tag{2.74}$$

The combined wave at the detector is given by

$$A(x, y, z, t) = A_0 b \exp(i(\omega t - q_i z))(1 + \exp(-i\boldsymbol{q} \cdot \boldsymbol{r}_{OB})). \tag{2.75}$$

The flux of the combined wave is

$$J(\boldsymbol{q}) = A_0^2 b^2 (1 + \exp(-i\boldsymbol{q} \cdot \boldsymbol{r}_{OB}))(1 + \exp(i\boldsymbol{q} \cdot \boldsymbol{r}_{OB})), \tag{2.76}$$

therefore we can write

$$A(\boldsymbol{q}) = A_0 b (1 + \exp(-i\boldsymbol{q} \cdot \boldsymbol{r}_{OB})). \tag{2.77}$$

This equation reveals that the combined scattering amplitude at some point on the detector specified by the scattering vector $\boldsymbol{q}$ only depends on the relative positions of the particles $\boldsymbol{r}_{OB}$.

2.4.3 Scattering off many particles

In the case of N identical scatterers, equation 2.77 becomes

$$A(\boldsymbol{q}) = A_0 b \sum_{j=1}^{N} \exp(-\boldsymbol{q} \cdot \boldsymbol{r}_j), \tag{2.78}$$

where $\boldsymbol{r}_j$ is the position of the j^{th} scatterer relative to some arbitrary origin. If the scattering centres are continuously dispersed, we can generalise further to get

$$A(\boldsymbol{q}) = A_0 b \int_V d^3r \; \eta(\boldsymbol{r}) \exp(-i\boldsymbol{q} \cdot \boldsymbol{r}), \tag{2.79}$$

where $\eta(\boldsymbol{r})$ is the local number density of the scatterers at $\boldsymbol{r}$. The amplitude is proportional to the three-dimensional Fourier transform of $\eta(\boldsymbol{r})$.

Typically, in a many-body system, there will be random variability in the scattering length b at different points due to the presence of isotopes and spin states. This gives rise to an incoherent component of the scattering signal, which can be thought of as background noise since it contains no structural information. In contrast to this, the coherent component contains structural information through its dependence on the relative positions of the scattering centres. Ignoring the incoherent component of the scattering, we can write the normalised coherent scattering amplitude for a sample containing multiple species as

$$A(\boldsymbol{q}) = \int_V d^3r \rho(\boldsymbol{r}) \exp(-i\boldsymbol{q} \cdot \boldsymbol{r}), \tag{2.80}$$

where $A(\boldsymbol{q})$ has been redefined as $A(\boldsymbol{q})/A_0$ and $\rho(\boldsymbol{r})$ is the coherent scattering length density distribution $\rho(\boldsymbol{r}) = \sum_\alpha b_\alpha \eta_\alpha(\boldsymbol{r})$. The subscript α refers to the different species present in the sample.

Using equation 2.80, we can write equation 2.68, i.e. the intensity, as:

$$I(\boldsymbol{q}) = < |A(\boldsymbol{q})|^2 > = \left\langle \int_V d^3r \rho(\boldsymbol{r}) \exp(-i\boldsymbol{q} \cdot \boldsymbol{r}) \int_V d^3r' \rho(\boldsymbol{r}') \exp(i\boldsymbol{q} \cdot \boldsymbol{r}') \right\rangle \tag{2.81}$$

where we introduced the time average $< ... >$ to reflect the finite measurement time of a detector. It is instructive to write this in a slightly different form. Upon making the substitution $\boldsymbol{u} = \boldsymbol{r} - \boldsymbol{r}'$ and rearranging, we obtain

$$I(\boldsymbol{q}) = \int d^3u \Big(\int d^3r' \rho(\boldsymbol{r'} + \boldsymbol{u}) \rho(\boldsymbol{r'}) \Big) \exp(-i\boldsymbol{q} \cdot \boldsymbol{u}), \tag{2.82}$$

where the factor in the brackets is the autocorrelation function of $\rho(\boldsymbol{r})$. This is related to the average of $\rho(\boldsymbol{r})\rho(\boldsymbol{r'})$ throughout the sample for some fixed $\boldsymbol{u}$, i.e.

$$< \rho(\boldsymbol{r})\rho(\boldsymbol{r'}) >= \frac{\int d^3r' \rho(\boldsymbol{r'} + \boldsymbol{u})\rho(\boldsymbol{r'})}{\int d^3r'}. \tag{2.83}$$

In calculating the average of $\rho(\boldsymbol{r})\rho(\boldsymbol{r'})$, positional information is lost - there is no unique way to recover $\rho(\boldsymbol{r})$. The objective of scattering is thus to obtain as much structural information as possible from measurements of $I(\boldsymbol{q})$.

2.4.4 Scattering off polymer blends

We are now ready to specialise the discussion of scattering to polymer blends. First, we must make some assumptions. Namely, for each species of polymer in the blend, we assume that each segment, i.e. monomer or Kuhn segment, acts as a scattering centre, and each of these segments has the same segmental scattering length $\hat{b}$ - this is the sum of the scattering lengths of the constituent atoms in the segment.

The scattering amplitude of a system containing a single type of polymer can be written as

$$A(\boldsymbol{q}) = \hat{b} \int_V d^3r \eta(\boldsymbol{r}) \exp(-i\boldsymbol{q} \cdot \boldsymbol{r}). \tag{2.84}$$

Generalising to a two-polymer mixture,

$$A(\boldsymbol{q}) = \int_V d^3r (\hat{b}_A \eta_A(\boldsymbol{r}) + \hat{b}_B \eta_B(\boldsymbol{r})) \exp(-i\boldsymbol{q} \cdot \boldsymbol{r}). \tag{2.85}$$

It follows that the scattering intensity in a two-polymer mixture is given by

$$\begin{aligned} I(\boldsymbol{q}) = \Big\langle & \hat{b}_A^2 \int d^3r \int d^3r' \eta_A(\boldsymbol{r}) \eta_A(\boldsymbol{r'}) \exp(-i\boldsymbol{q} \cdot (\boldsymbol{r} - \boldsymbol{r'})) + \\ & 2\hat{b}_A \hat{b}_B \int d^3r \int d^3r' \eta_A(\boldsymbol{r}) \eta_B(\boldsymbol{r'}) \exp(-i\boldsymbol{q} \cdot (\boldsymbol{r} - \boldsymbol{r'})) + \\ & \hat{b}_B^2 \int d^3r \int d^3r' \eta_B(\boldsymbol{r}) \eta_B(\boldsymbol{r'}) \exp(-i\boldsymbol{q} \cdot (\boldsymbol{r} - \boldsymbol{r'})) \Big\rangle. \end{aligned} \tag{2.86}$$

To write this more compactly, we can introduce quantities called partial structure factors:

$$S_{\alpha\beta} = \Big\langle \frac{v_\alpha v_\beta}{V} \int d^3r \int d^3r' \eta_\alpha(\boldsymbol{r}) \eta_\beta(\boldsymbol{r'}) \exp(-i\boldsymbol{q} \cdot (\boldsymbol{r} - \boldsymbol{r'})) \Big\rangle \tag{2.87a}$$

$$= \Big\langle \frac{v_\alpha v_\beta}{V} \int d^3u \int d^3r' \eta_\alpha(\boldsymbol{r'} + \boldsymbol{u}) \eta_\beta(\boldsymbol{r'}) \exp(-i\boldsymbol{q} \cdot \boldsymbol{u}) \Big\rangle, \tag{2.87b}$$

where the $v_{\alpha(\beta)}$ factors are the volumes of each type of polymer segment. In terms of $S_{\alpha\beta}$, the intensity can be written as

$$I(\boldsymbol{q}) = V(\varrho_A^2 S_{AA}(\boldsymbol{q}) + 2\varrho_A \varrho_B S_{AB}(\boldsymbol{q}) + \varrho_B^2 S_{BB}(\boldsymbol{q})), \tag{2.88}$$

where the ϱ_α are scattering length densities defined by $\varrho_\alpha = \frac{\hat{b}_\alpha}{v_\alpha}$.

Noting that $v_\alpha \eta_\alpha(\boldsymbol{r}) = \phi_\alpha(\boldsymbol{r})$, the partial structure factors can be rewritten as

$$S_{\alpha\beta}(\boldsymbol{q}) = \Big\langle \frac{1}{V} \int d^3u \int d^3r' \phi_\alpha(\boldsymbol{r}' + \boldsymbol{u}) \phi_\beta(\boldsymbol{r}') \exp(-i\boldsymbol{q} \cdot \boldsymbol{u}) \Big\rangle. \tag{2.89}$$

The scattering depends on fluctuations in the scattering length distribution $\rho(\boldsymbol{r})$. This allows us to write the above in terms of fluctuations of the volume fraction:

$$S_{\alpha\beta}(\boldsymbol{q}) = \Big\langle \frac{1}{V} \int d^3u \int d^3r' \delta\phi_\alpha(\boldsymbol{r}' + \boldsymbol{u}) \delta\phi_\beta(\boldsymbol{r}') \exp(-i\boldsymbol{q} \cdot \boldsymbol{u}) \Big\rangle. \tag{2.90}$$

Assuming the mixture is incompressible, it follows that $\delta\phi_A(\boldsymbol{r}) = -\delta\phi_B(\boldsymbol{r})$, therefore $S_{AA}(\boldsymbol{q}) = S_{BB}(\boldsymbol{q}) = -S_{AB}(\boldsymbol{q}) = -S_{BA}(\boldsymbol{q})$. We refer to $S(\boldsymbol{q}) \equiv S_{AA}(\boldsymbol{q})$ as the structure factor. Inserting $S(\boldsymbol{q})$ into equation 2.88, the intensity can be written as

$$I(\boldsymbol{q}) = V(\Delta\varrho)^2 S(\boldsymbol{q}), \tag{2.91}$$

where $\Delta\varrho = \varrho_B - \varrho_A$. The intensity is directly proportional to the structure factor. In isotropic systems, $I(\boldsymbol{q})$ and $S(\boldsymbol{q})$ depend only on the magnitude of $\boldsymbol{q}$. Indeed, polymer blends are generally isotropic. In an experimental context, $S(q,t)$ is often calculated as the radial average of $S(\boldsymbol{q},t)$ [15, 53].

2.4.5 The time evolution of the structure factor

There is a duality concerning the time evolution of the structure factor during spinodal decomposition and dissolution: it is relatively easy to measure but much harder to model [17, 18]. Specifically, the full equation of motion for the structure factor during these processes is unclosed. We demonstrate this below.

First, we note that the structure factor can be written compactly as

$$S(q,t) = \frac{1}{V} < \delta\phi(q,t)\delta\phi(-q,t) >, \tag{2.92}$$

where $\delta\phi(q) = \int d^3r \ \delta\phi(\boldsymbol{r}) \exp(-i\boldsymbol{q} \cdot \boldsymbol{r})$. To aid the next chapter, we take this opportunity to introduce the power spectrum of $\phi(\boldsymbol{r})$:

$$P(q,t) = \delta\phi(q,t)\delta\phi(-q,t). \tag{2.93}$$

The structure factor is related to the power spectrum via

$$S(q,t) = \frac{1}{V} < P(q,t) > . \tag{2.94}$$

Differentiating equation 2.92 with respect to time, we obtain the following equation of motion for the structure factor in terms of $\frac{\partial\delta\phi(q,t)}{\partial t}$:

$$\frac{\partial S(q,t)}{\partial t} = \frac{1}{V}\Big\langle \frac{\partial\delta\phi(q)}{\partial t}\delta\phi(-q) \Big\rangle + \frac{1}{V}\Big\langle \delta\phi(q)\frac{\partial\delta\phi(-q)}{\partial t} \Big\rangle. \tag{2.95}$$

We can use the CHC-FHdG equation to write down the equation of motion for $\delta\phi(q,t)$, i.e. $\frac{\partial\delta\phi(q,t)}{\partial t}$. For simplicity, we assume that the square gradient coefficient is constant. In this case, the time evolution of the volume fraction is given by

$$\frac{\partial \phi(\boldsymbol{r},t)}{\partial t} = M\nabla^2\Big(\frac{\partial f(\phi)}{\partial \phi} - 2\kappa k_B T \nabla^2 \phi\Big), \tag{2.96}$$

where we have combined equations 2.47 and 2.50. Upon making the substitution $\phi(\boldsymbol{r},t) = \phi_0 + \delta\phi(\boldsymbol{r},t)$ and performing a power series expansion, we obtain

$$\frac{\partial \delta\phi(\boldsymbol{r},t)}{\partial t} = M\nabla^2\Big(\frac{\partial^2 f}{\partial \phi^2}\Big|_{\phi_0}\delta\phi - 2\kappa k_B T\nabla^2\delta\phi + \sum_{n=3}^{\infty}\frac{1}{(n-1)!}\frac{\partial^n f}{\partial \phi^n}\Big|_{\phi_0}\delta\phi^{n-1}\Big). \tag{2.97}$$

In Fourier space, this becomes

$$\begin{aligned}\frac{\partial \delta\phi(q,t)}{\partial t} =& -Mq^2\Big(\frac{\partial^2 f}{\partial \phi^2}\Big|_{\phi_0}\delta\phi(q) + 2\kappa k_B T q^2\delta\phi(q) \\ &+ \sum_{n=3}^{\infty}\frac{1}{(n-1)!}\frac{\partial^n f}{\partial \phi^n}\Big|_{\phi_0}\int d^3r\ \delta\phi(\boldsymbol{r})^{n-1}\exp(-i\boldsymbol{q}\cdot\boldsymbol{r})\Big).\end{aligned} \tag{2.98}$$

Upon substituting equation 2.98 and its complex conjugate into equation 2.95, we obtain, after rearranging,

$$\begin{aligned}\frac{\partial S(q,t)}{\partial t} =& -2Mq^2\Big(\frac{\partial^2 f}{\partial \phi^2}\Big|_{\phi_0}S(q) + 2\kappa k_B T q^2 S(q) \\ &+ \frac{1}{2V}\sum_{n=3}^{\infty}\frac{1}{(n-1)!}\frac{\partial^n f}{\partial \phi^n}\Big|_{\phi_0} \\ &\Big[\int d^3r\int d^3r'\ <\delta\phi(\boldsymbol{r})^{n-1}\delta\phi(\boldsymbol{r}')>\exp(-i\boldsymbol{q}\cdot(\boldsymbol{r}-\boldsymbol{r}')) \\ &+ \int d^3r\int d^3r'\ <\delta\phi(\boldsymbol{r})\delta\phi(\boldsymbol{r}')^{n-1}>\exp(-i\boldsymbol{q}\cdot(\boldsymbol{r}-\boldsymbol{r}'))\Big]\Big).\end{aligned} \tag{2.99}$$

The terms in the square brackets cannot be written in terms of $S(q,t)$ - this can be shown using the cross-correlation theorem [58]. Trying to write down the equations of motion of the terms in the square brackets leads us to discover an infinite hierarchy of coupled differential equations. Therefore, equation 2.99 is unclosed [17, 18]. This can be traced back to the non-linear terms in the CHC-FHdG equation. We note that full knowledge of $\delta\phi(\boldsymbol{r})$ is only possible in a computational setting since, as mentioned earlier, positional information is lost when measuring the structure factor experimentally.

A truncation scheme is required to make equation 2.99 tractable.

2.4.6 The linear Cahn-Hilliard-Cook Flory-Huggins-de Gennes equation

Arguably, the simplest and most commonly used truncation scheme is based on the linear CHC-FHdG equation (equation 2.63) [17, 18, 26], which, in Fourier space, becomes

$$\frac{\partial \delta\phi(q,t)}{\partial t} = -\frac{Mk_BTq^2}{v_0}\Big[2(\chi_s - \chi) + \frac{\sigma^2}{18\phi_0(1-\phi_0)}q^2\Big]\phi(q,t) + \xi(q,t) \tag{2.100a}$$

$$= R(q)\delta\phi(q,t) + \xi(q,t). \tag{2.100b}$$

Upon substituting equation 2.100b and its complex conjugate into equation 2.95, we obtain

$$\frac{\partial S(q,t)}{\partial t} = 2R(q)S(q,t) + \frac{1}{V}C(q), \tag{2.101}$$

where $C(q) =< \xi(q,t)\delta\phi(-q,t) + \xi(-q,t)\delta\phi(q,t) >$. The variable $C(q)$ appears in the definition of the covariance of the noise term in Fourier space [59] (see reference for proof):

$$< \xi(q,t)\xi(-q,t') >= C(q)\delta(t-t'). \tag{2.102}$$

Therefore, $C(q)$ can be calculated by mapping equation 2.54b to Fourier space

$$\begin{aligned}
< \xi(q,t)\xi(-q,t') >= & -2Mk_BT\delta(t-t') \\
& \int d^3r \int d^3r' \nabla^2(\delta(\boldsymbol{r}-\boldsymbol{r'}))\exp(-i\boldsymbol{q}\cdot(\boldsymbol{r}-\boldsymbol{r'})) && \text{(2.103a)} \\
= & -2Mk_BT\delta(t-t') \\
& \int d^3r \int d^3r' \delta(\boldsymbol{r}-\boldsymbol{r'})\nabla^2\exp(-i\boldsymbol{q}\cdot(\boldsymbol{r}-\boldsymbol{r'})) && \text{(2.103b)} \\
= & -2Mk_BT(-q^2)\delta(t-t') \\
& \int d^3r \int d^3r' \delta(\boldsymbol{r}-\boldsymbol{r'})\exp(-i\boldsymbol{q}\cdot(\boldsymbol{r}-\boldsymbol{r'})) && \text{(2.103c)} \\
= & 2Mk_BTq^2V\delta(t-t'), && \text{(2.103d)}
\end{aligned}$$

where we applied integration by parts twice to get from equation 2.103a to equation 2.103b. Using equation 2.103d, we can identify $C(q) = 2Mk_BTq^2V$.

Putting everything together, we obtain the linear CHC-FHdG equation for the time evolution of the structure factor:

$$\frac{\partial S(q,t)}{\partial t} = 2R(q)S(q,t) + 2Mk_BTq^2. \tag{2.104}$$

The amplification factor can be written as [60]

$$R(q) = -Mk_BTq^2S_T^{-1}(q), \tag{2.105}$$

where S_T is the stationary solution to equation 2.104:

$$S_T(q) = v_0\Big[2(\chi_s - \chi) + \frac{\sigma^2}{18}\Big(\frac{1}{\phi_0(1-\phi_0)}\Big)q^2\Big]^{-1}. \tag{2.106}$$

In dissolution, S_T coincides with the small-q limit of de Gennes' random phase approximation for the static structure factor [50,60]. In spinodal decomposition, S_T coincides with the small-q limit of the 'virtual' structure factor [50, 60]. Rewriting the final term on the right-hand side of equation 2.104 as '$-2R(q)S_T(q)$', equation 2.104 can be solved using separation of variables to get [60]

$$S(q,t) = (S(q,0) - S_T)\exp(2R(q)t) + S_T(q). \tag{2.107}$$

From this solution, a fitting relationship can be established to calculate $R(q)$ from experimental (or simulated) data [2]. This provides a means of testing the linear CHC-FHdG equation, which, as we mentioned earlier, has been shown to quantitatively capture the early stage of spinodal decomposition in polymer blends.

2.4.7 The Akcasu equation

Indeed, the linear CHC-FHdG equation for the structure factor is only valid during the early stage of spinodal decomposition, i.e. while composition fluctuations are small. Therefore, the validity of the linear CHC-FHdG equation is limited. Motivated to improve this situation, Akcasu et al. set out to develop an approximate, tractable, non-linear equation of motion [19,31,32]. Their equation is based on that of Langer, Bar-on and Miller [61], who worked on the same problem but in the context of small molecule mixtures.

The derivation of the equation of motion developed by Akcasu et al., which we refer to as the Akcasu equation, is quite long. To the best of our knowledge, it has not been published in its entirety. We provide the full derivation in chapter 4. For now, we simply quote the result in its simplest, most interpretable form:

$$\frac{\partial S(q,t)}{\partial t} = 2R(q)S(q,t)[1 + Z(q,t)] - 2R(q)S_{\text{eq}}(q)[1 + Z_{\text{eq}}(q)], \tag{2.108}$$

where $Z(q,t)$ is a non-linear mode-coupling term, $Z_{\text{eq}}(q)$ is the equilibrium value of $Z(q,t)$, and $S_{\text{eq}}(q)$ is the equilibrium value of $S(q,t)$. The mode-coupling term describes the coupling of composition fluctuations with different wavelengths. The term after the minus sign on the right-hand side is the noise term, which ensures the correct long-time (equilibrium) behaviour of $S(q,t)$. As a result of the closure approximations introduced by Akcasu et al., the noise term here is, in general, different to that in equation 2.104.

There has been no reported comparison between the predictions of the Akcasu equation and numerical or experimental measurements of the structure factor in the case of spinodal decomposition. In the case of dissolution, a comparison with experimental data was performed by Akcasu et al. [31]. The comparison revealed a quantitative discrepancy between theory and experiment, which worsened as the dissolution time increased. Akcasu et al. used best-guess values of molecular and thermodynamic parameters to solve their equation because some of the parameters are hard to measure. It is unclear whether the Akcasu equation failed as a result of the equation being inadequate or incorrect parameter values being used.

2.4.8 The small-q limit

Both equations 2.104 and 2.108 are only valid in the small-q limit. This is a consequence of using the modified form of the Cahn-Hilliard free energy functional proposed by de Gennes (see equations 2.57 and 2.58) to derive them. As we mentioned beneath equation 2.58, the square gradient coefficient was derived to be consistent with the random phase approximation for the static structure factor. We should now be more specific: the square gradient coefficient was actually derived to be consistent with the small-q (or 'long wavelength') limit of de Gennes' random phase approximation [50, 51, 60], which we outline in the next section. The small-q limit is defined as $qR_g << 1$ [51, 60], where $R_g = \sqrt{\frac{N\sigma^2}{6}}$ is a representative radius of gyration for the polymers in the blend.

2.4.9 The random phase approximation for the static structure factor

In the context of polymer physics, the random phase approximation (RPA) was developed by de Gennes to characterise composition fluctuations due to thermal fluctuations (Brownian motion) in a one-phase blend [38, 50]. The result is an equation for the static structure factor. We outline the RPA theory below [26, 38, 41, 50].

In the context of the lattice model introduced in section 2.2.2, let us consider a binary polymer blend in which the constituent polymers, labelled A and B, have degrees of polymerisation N_A and N_B, respectively. To describe the local composition, we use the local volume fractions $\phi_A(\boldsymbol{r})$ and $\phi_B(\boldsymbol{r})$, where $\phi_A(\boldsymbol{r}) = 1$ ($\phi_B(\boldsymbol{r}) = 1$) if the lattice site located at $\boldsymbol{r}$ is occupied by a segment of polymer A (B), otherwise $\phi_A(\boldsymbol{r}) = 0$ ($\phi_B(\boldsymbol{r}) = 0$). We assume the blend is incompressible, therefore $\phi_A(\boldsymbol{r}) + \phi_B(\boldsymbol{r}) = 1$ for all $\boldsymbol{r}$.

Local fluctuations in the composition can be defined as $\delta\phi_A(\boldsymbol{r}) = \phi_A(\boldsymbol{r}) - \phi_{0,A}$ (and similarly for $\phi_B(\boldsymbol{r})$), where $\phi_{0,A}$ is the average (overall) volume fraction of A. These fluctuations are characterised by the following correlation functions

$$S_{AA}(\boldsymbol{r} - \boldsymbol{r}') =< \delta\phi_A(\boldsymbol{r})\delta\phi_A(\boldsymbol{r}') > \tag{2.109a}$$
$$S_{BB}(\boldsymbol{r} - \boldsymbol{r}') =< \delta\phi_B(\boldsymbol{r})\delta\phi_B(\boldsymbol{r}') > \tag{2.109b}$$
$$S_{AB}(\boldsymbol{r} - \boldsymbol{r}') =< \delta\phi_A(\boldsymbol{r})\delta\phi_B(\boldsymbol{r}') > . \tag{2.109c}$$

Under the incompressibility assumption,

$$S_{AA}(\boldsymbol{r} - \boldsymbol{r}') = S_{BB}(\boldsymbol{r} - \boldsymbol{r}') = -S_{AB}(\boldsymbol{r} - \boldsymbol{r}') = -S_{BA}(\boldsymbol{r} - \boldsymbol{r}'), \tag{2.110}$$

i.e. only one correlation function is required to characterise the fluctuations, $S(\boldsymbol{r} - \boldsymbol{r}') \equiv S_{AA}(\boldsymbol{r} - \boldsymbol{r}')$.

We wish to calculate $S(\boldsymbol{r} - \boldsymbol{r}')$ or, as we shall see, its Fourier transform. To do this, we turn to linear response theory [34]. This requires us to introduce two weak external potentials, $u_A(\boldsymbol{r})$ and $u_B(\boldsymbol{r})$, which act respectively on the segments of A and B. The source of these external potentials could be, for example, an external electric field, but the theory does not require we specify this. Indeed, the external potentials could be viewed as a tool for facilitating the use of linear response theory. Under the external potentials, the averages of $\phi_A(\boldsymbol{r})$ and $\phi_B(\boldsymbol{r})$ deviate from $\phi_{0,A}$ and $\phi_{0,B}$, respectively. In terms of $\phi_A(\boldsymbol{r})$, we denote this deviation as $\overline{\delta\phi_A(\boldsymbol{r})} =< \phi_A(\boldsymbol{r}) >_{\text{ext}} -\phi_{0,A}$. Linear response theory allows us to relate $\overline{\delta\phi_A(\boldsymbol{r})}$ to the perturbing potentials via the correlation function $S(\boldsymbol{r} - \boldsymbol{r}')$, which, in this context, is often referred to as a response function:

$$\overline{\delta\phi_A(\boldsymbol{r})} = \frac{-1}{v_0 k_B T} \int d^3r' S(\boldsymbol{r} - \boldsymbol{r}')[u_A(\boldsymbol{r}') - u_B(\boldsymbol{r}')]. \tag{2.111}$$

We note that the integral should be a sum since we are considering a lattice model of mixing, however approximating the sum with an integral simplifies the ensuing maths. The factor of $1/v_0$ keeps the dimensions consistent following this approximation.

To make progress, we assume we can derive an alternative equation for $\overline{\delta\phi_A(\boldsymbol{r})}$ using an ideal mixture in a randomly mixed state as a base and adding complexities, such as molecular interactions, as perturbations. For the ideal randomly mixed base state, we have the following non-zero correlation functions due to chain connectivity:

$$S^0_{AA}(\boldsymbol{r}-\boldsymbol{r}') =< \delta\phi_A(\boldsymbol{r})\delta\phi_A(\boldsymbol{r}') > \tag{2.112a}$$
$$S^0_{BB}(\boldsymbol{r}-\boldsymbol{r}') =< \delta\phi_B(\boldsymbol{r})\delta\phi_B(\boldsymbol{r}') > . \tag{2.112b}$$

In contrast, $S^0_{AB}(\boldsymbol{r}-\boldsymbol{r}') =< \delta\phi_A(\boldsymbol{r})\delta\phi_B(\boldsymbol{r}') >= 0$. We now estimate the effects of molecular interactions, excluded volume effects and external potentials using linear response theory and the aforementioned perturbation assumption:

$$\overline{\delta\phi_A(\boldsymbol{r})} = \frac{-1}{v_0 k_B T}\int d^3r' S^0_{AA}(\boldsymbol{r}-\boldsymbol{r}')[u_A(\boldsymbol{r}') + w_A(\boldsymbol{r}') + V(\boldsymbol{r}')] \tag{2.113a}$$
$$\overline{\delta\phi_B(\boldsymbol{r})} = \frac{-1}{v_0 k_B T}\int d^3r' S^0_{BB}(\boldsymbol{r}-\boldsymbol{r}')[u_B(\boldsymbol{r}') + w_B(\boldsymbol{r}') + V(\boldsymbol{r}')], \tag{2.113b}$$

where $w_A(\boldsymbol{r}')+V(\boldsymbol{r}')$ and $w_B(\boldsymbol{r}')+V(\boldsymbol{r}')$ are mean-field potentials comprised of fields relating to molecular interactions and excluded volume effects. The fields relating to molecular interactions are given by

$$w_A(\boldsymbol{r}) = -z[\epsilon_{AA} < \phi_A(\boldsymbol{r}) >_{\text{ext}} + \epsilon_{AB} < \phi_B(\boldsymbol{r}) >_{\text{ext}}] \tag{2.114a}$$
$$w_B(\boldsymbol{r}) = -z[\epsilon_{BA} < \phi_A(\boldsymbol{r}) >_{\text{ext}} + \epsilon_{BB} < \phi_B(\boldsymbol{r}) >_{\text{ext}}]. \tag{2.114b}$$

Equations 2.113a and 2.113b constitute a pair of simultaneous equations for three unknowns: $\overline{\delta\phi_A(\boldsymbol{r})}$, $\overline{\delta\phi_B(\boldsymbol{r})}$ and $V(\boldsymbol{r})$. A third simultaneous equation can be obtained from the incompressibility assumption:

$$\overline{\delta\phi_A(\boldsymbol{r})} + \overline{\delta\phi_B(\boldsymbol{r})} = 0. \tag{2.115}$$

Expressing the solution to these simultaneous equations in the form of equation 2.111 would allow us to to determine $S(\boldsymbol{r}-\boldsymbol{r}')$. It is convenient to solve the simultaneous equations in Fourier space, which allows us to make use of the convolution theorem. The result of solving the simultaneous equations in Fourier space is

$$\overline{\delta\phi_A(q)} = \frac{-1}{v_0 k_B T}\Big[\frac{1}{S^0_{AA}(q)} + \frac{1}{S^0_{BB}(q)} - \frac{2\chi}{v_0}\Big]^{-1}(u_A(q) - u_B(q)). \tag{2.116}$$

Upon comparing equation 2.116 with the Fourier transform of equation 2.111, we can identify

$$\frac{1}{S(q)} = \frac{1}{S^0_{AA}(q)} + \frac{1}{S^0_{BB}(q)} - \frac{2\chi}{v_0}. \tag{2.117}$$

We now need to determine the ideal correlation functions, which we can do using thermodynamic relations. We are guided by the following result, which applies to polymer blends in the one-phase region and can be derived independently of the RPA [15, 40]:

$$\frac{1}{S(q=0)} = \frac{1}{v_0 k_B T}\frac{\partial^2 F^{\text{lat}}_{\text{mix,PP}}}{\partial \phi^2} = \frac{1}{k_B T}\frac{\partial \mu}{\partial \phi}. \tag{2.118}$$

We note that we have included the factor of $\frac{1}{v_0}$ in the definition of μ to ensure consistency with equation 2.46, which applies in the presence of composition gradients.

Equation 2.118 motivates us to calculate how the local composition of a blend changes in response to a change in the local chemical potential. To begin, we consider an ideal blend ($\chi = 0$) and assume the volume under consideration is large relative to the size of the constituent polymers. In large volumes, the mean-square magnitude of composition fluctuations is small - the composition is indistinguishable from the average composition. This means we can use equation 2.31 to write the chemical potential of species A as

$$\mu_A = \frac{1}{v_0}\frac{\partial F^{\text{lat}}_{\text{mix,PP}}}{\partial \phi_A} = \frac{k_B T}{N_A v_0}\ln(\phi_A). \tag{2.119}$$

It follows that the change in the local composition of species A in the volume in response to a change in the local chemical potential is

$$\frac{\partial \phi_A}{\partial \mu_A} = \frac{\phi_A v_0 N_A}{k_B T}. \tag{2.120}$$

A similar response function can be obtained for species B:

$$\frac{\partial \phi_B}{\partial \mu_B} = \frac{\phi_B v_0 N_B}{k_B T}. \tag{2.121}$$

We can combine equations 2.120 and 2.121 to obtain the following equation for the change in the exchange chemical potential:

$$\delta\mu = \delta\mu_A - \delta\mu_B = k_B T\Big(\frac{\delta\phi_A}{\phi_A v_0 N_A} - \frac{\delta\phi_B}{\phi_B v_0 N_B}\Big). \tag{2.122}$$

Assuming the blend is incompressible, we can then write

$$\frac{\partial \phi}{\partial \mu} = \frac{1}{k_B T}\Big(\frac{1}{\phi v_0 N_A} + \frac{1}{(1-\phi) v_0 N_B}\Big)^{-1}. \tag{2.123}$$

For small volumes, i.e. on the scale of or smaller than the size of the constituent polymers, composition fluctuations are significant. Equation 2.123 needs to be generalised before it can be applied to such volumes. In Fourier space, the response functions given by equations 2.120 and 2.121 can be generalised by introducing a q-dependence via the (dimensionless) form factor of a polymer chain:

$$\frac{\partial \phi_A(q)}{\partial \mu_A(q)} = \frac{\phi_A v_0 P_A(q)}{k_B T} \tag{2.124a}$$

$$\frac{\partial \phi_B(q)}{\partial \mu_B(q)} = \frac{\phi_B v_0 P_B(q)}{k_B T}. \tag{2.124b}$$

Form factors are related to the size and shape of individual molecules [15]. Using equations 2.124a and 2.124b, we can generalise equation 2.123 as

$$\frac{\partial\phi(q)}{\partial\mu(q)} = \frac{1}{k_BT}\Big(\frac{1}{\phi v_0 P_A(q)} + \frac{1}{(1-\phi)v_0 P_B(q)}\Big)^{-1}. \tag{2.125}$$

Upon comparing equations 2.125 and 2.117 (setting $\chi = 0$ in the latter), we can identify the non-interacting structure factor

$$S^{-1}_{\text{n.i.}}(q) = \frac{1}{S^0_{AA}(q)} + \frac{1}{S^0_{BB}(q)} = \frac{1}{\phi v_0 P_A(q)} + \frac{1}{(1-\phi)v_0 P_B(q)}. \tag{2.126}$$

Substituting this relation into equation 2.117 yields

$$\frac{1}{S(q)} = \frac{1}{\phi v_0 P_A(q)} + \frac{1}{(1-\phi)v_0 P_B(q)} - \frac{2\chi}{v_0}. \tag{2.127}$$

To proceed, we need to insert the appropriate form factors, $P_A(q)$ and $P_B(q)$, into equation 2.127. We know from equation 2.126 that $P_A(q)$ is related to $S^0_{AA}(q)$ and $P_B(q)$ is related to $S^0_{BB}(q)$. Since $S^0_{AA}(q)$ and $S^0_{BB}(q)$ correspond to the randomly mixed base state, $P_A(q)$ and $P_B(q)$ must describe Gaussian chains, i.e. polymers that are described by random walk statistics. The form factor of a Gaussian chain is given by [15, 16, 38]

$$P_A(q) = N_A f_D(qR_{g,A}), \tag{2.128}$$

where

$$f_D(qR_{g,A}) = \frac{2}{(q^2R^2_{g,A})^2}(q^2R^2_{g,A} - 1 + \exp\big(-q^2R^2_{g,A}\big)) \tag{2.129}$$

is known as the Debye function. In the small-q limit, the Debye function can be expanded as

$$f_D(qR_{g,A}) \approx 1 - \frac{q^2R^2_{g,A}}{3}. \tag{2.130}$$

Upon substituting equations 2.128 and 2.130 into equation 2.127 and simplifying, we obtain the small-q limit of de Gennes' random phase approximation for the static structure factor:

$$\frac{1}{S(q)} = \frac{1}{\phi v_0 N_A} + \frac{1}{(1-\phi)v_0 N_B} - \frac{2\chi}{v_0} + \frac{q^2}{18v_0}\Big(\frac{\sigma_A^2}{\phi} + \frac{\sigma_B^2}{(1-\phi)}\Big). \tag{2.131}$$

This coincides with equation 2.106 when we set $N_A = N_B = N$ and $\sigma_A = \sigma_B = \sigma$ and write $\phi = \phi_0$ (indeed, in equation 2.131, $\phi = \phi_A$ corresponds to the overall volume fraction of monomers of type A, which is equivalent to ϕ_0 in equation 2.106).

The small-q limit of de Gennes' random phase approximation for the static structure factor can be derived from a free energy functional in the form of equation 2.48, allowing for the square gradient coefficient to depend on the composition. For a free energy functional of this form, the chemical potential is given by equation 2.61. Upon linearising the chemical potential, we obtain

$$\mu = \frac{\partial f}{\partial\phi}\Big|_{\phi_0} + \frac{\partial^2 f}{\partial\phi^2}\Big|_{\phi_0}\delta\phi - 2k_BT\kappa(\phi_0)\nabla^2\delta\phi. \tag{2.132}$$

In Fourier space this becomes

$$\mu(q) = \frac{\partial f}{\partial \phi}\Big|_{\phi_0} \delta(\boldsymbol{q}) + \frac{\partial^2 f}{\partial \phi^2}\Big|_{\phi_0} \delta\phi(q) + 2k_B T q^2 \kappa(\phi_0)\delta\phi(q). \tag{2.133}$$

It follows that

$$\frac{\partial \mu(q)}{\partial \phi(q)} = \frac{\partial^2 f}{\partial \phi^2}\Big|_{\phi_0} + 2k_B T q^2 \kappa(\phi_0). \tag{2.134}$$

Upon substituting equation 2.57 into equation 2.134 and simplifying, we obtain

$$\frac{\partial \mu(q)}{\partial \phi(q)} = k_B T\Big(\frac{1}{N_A v_0 \phi_0} + \frac{1}{N_B v_0 (1-\phi_0)} - \frac{2\chi}{v_0} + 2q^2\kappa(\phi_0)\Big). \tag{2.135}$$

Comparing this equation with equation 2.131 (writing $\phi_0 = \phi$), we can identify the entropic component to the square gradient coefficient given in equation 2.58. We note that the RPA theory does not yield the purely energetic component of the square gradient coefficient. Although this term is commonly neglected, it can be recovered by including a correction term in equation 2.127 [26, 47].

2.5 System identification

Dynamical systems are ubiquitous in a wide range of fields. In many of these fields, there is a duality between abundant measurement data and elusive governing equations [33], i.e. differential equations describing a process of interest. Embracing this duality, the field of system identification, concerned with building models of dynamical systems from measurement data, has emerged as an alternative to traditional theory-driven modelling [33].

Broadly speaking, existing system identification techniques can be categorised into three groups based on the type of models they give rise to [33, 62]:

- Black box models
- Linear models
- Parsimonious non-linear models, i.e. non-linear models with few terms

Examples of black box techniques include NARMAX [63], time-lagged autoencoders [64] and LSTM networks [65]. While many black box techniques have demonstrated the ability to make accurate predictions for complex systems, they are lacking in terms of generalisability and interpretability. Typically, generalisability and interpretability are important considerations in the development of scientific theories. For this reason, we subsequently focus on system identification techniques that give rise to linear or parsimonious non-linear models.

2.5.1 Motivating linear system identification

We first motivate linear system identification, which is often a logical first port of call when modelling dynamical systems [33, 66]. There are several reasons for this. For example, linear models are straightforward to interpret and simulate. Furthermore,

many techniques exist for controlling systems described by linear models. Other motivating factors are outlined below.

Linear models of dynamical systems can be represented as follows:

$$\frac{d\mathbf{x}}{dt} = \mathcal{A}\mathbf{x}, \tag{2.136}$$

where $\mathbf{x} \in \mathbb{R}^n$ is the state of the system, i.e. a vector comprised of variables of interest, and $\mathcal{A} \in \mathbb{R}^{n \times n}$ is a matrix. Unlike non-linear models, linear models always admit a closed-form solution, specifically:

$$\mathbf{x}(t_0 + t) = \exp(\mathcal{A}t)\mathbf{x}(t_0). \tag{2.137}$$

The dynamics described by linear models are encoded in the eigenvectors and eigenvalues of $\mathcal{A}$, which are defined by the following relationship, i.e. the eigendecomposition of $\mathcal{A}$:

$$\mathcal{A}\mathbf{T} = \mathbf{T}\mathbf{\Omega}, \tag{2.138}$$

where $\mathbf{T}$ is a matrix comprised of the eigenvectors appended column-wise and $\mathbf{\Omega}$ is a diagonal matrix containing the corresponding eigenvalues. One can use $\mathbf{T}$ to define a transformation $\mathbf{z} = \mathbf{T}^{-1}\mathbf{x}$ into eigenvector coordinates. In this coordinate system, the dynamics of each transformed variable z_j are decoupled, giving rise to simple models of the form

$$\frac{d\mathrm{z}_j}{dt} = \omega_j \mathrm{z}_j. \tag{2.139}$$

Using equation 2.137, we can write the discrete analogue to equation 2.136 as

$$\mathbf{x}_{k+1} = \mathbf{A}\mathbf{x}_k, \tag{2.140}$$

where $\mathbf{A} = \exp(\mathcal{A}\Delta t)$ and $\mathbf{x}_k$ is a snapshot of the system, i.e. a snapshot of the state vector, at time $t = k\Delta t$. The eigenvectors and eigenvalues of $\mathbf{A}$ are contained in $\mathbf{T}$ and $\mathbf{\Lambda} = \exp(\mathbf{\Omega}\Delta t)$, respectively.

2.5.2 Dynamic mode decomposition (DMD)

Developed by Schmid [67] in the field of fluid mechanics before being developed by others [33, 66, 68], dynamic mode decomposition (DMD) is a algorithm for calculating the leading eigenvectors and eigenvalues of the best-fit linear operator $\mathbf{A}$ that approximately describes the dynamics of a high-dimensional, non-linear, spatio-temporal system. A purely data-driven technique, DMD only requires snapshots of the system as an input. We outline DMD below [33, 66].

DMD is formulated based on the following equation (c.f. equation 2.137):

$$\mathbf{X}' \approx \mathbf{A}\mathbf{X}, \tag{2.141}$$

where $\mathbf{X}$ and $\mathbf{X}'$ are data matrices comprised of snapshots $\mathbf{x}_k$ appended column-wise. Given m snapshots sampled every Δt in time, the data matrices are given by

$$\mathbf{X} = \begin{bmatrix} | & | & & | \\ \mathbf{x}_1 & \mathbf{x}_2 & \dots & \mathbf{x}_{m-1} \\ | & | & & | \end{bmatrix} \tag{2.142a}$$

$$\mathbf{X}' = \begin{bmatrix} | & | & & | \\ \mathbf{x}_2 & \mathbf{x}_3 & \dots & \mathbf{x}_{m} \\ | & | & & | \end{bmatrix}. \tag{2.142b}$$

One might wonder about the point of using DMD to calculate the eigendecomposition of $\mathbf{A}$ when they could calculate $\mathbf{A}$ directly using least-squares regression instead:

$$\mathbf{A} = \underset{\mathbf{A}}{\text{argmin}} ||\mathbf{X}' - \mathbf{A}\mathbf{X}||_F = \mathbf{X}'\mathbf{X}^\dagger, \tag{2.143}$$

where F denotes the Frobenius norm and † denotes the Moore-Penrose pseudoinverse [69]. The motivation for the approach adopted in DMD is that the calculation in equation 2.143 can prove problematic if $\mathbf{A}$ is high-dimensional. Given that each snapshot contains n elements, $\mathbf{A}$ will contain n^2 elements. Therefore, if n is large, just representing $\mathbf{A}$ could be problematic, let alone performing calculations involving it.

To circumvent any calculations that directly involve $\mathbf{A}$, DMD makes use of dimensionality reduction through singular value decomposition (SVD), a data-driven technique for matrix factorisation. The SVD factorisation is structured in such a way that a low-dimensional, or low-rank, approximation to the original matrix is often easy to obtain. To illustrate this, we consider the SVD of $\mathbf{X}$. Given that the snapshots $\mathbf{x}_k$ contain n elements, meaning $\mathbf{X} \in \mathbb{R}^{n\times(m-1)}$, the SVD of $\mathbf{X}$ is given by

$$\mathbf{X} = \mathbf{U}\mathbf{\Sigma}\mathbf{V}^*, \tag{2.144}$$

where $\mathbf{U} \in \mathbb{R}^{n\times n}$ and $\mathbf{V} \in \mathbb{R}^{(m-1)\times(m-1)}$ are unitary matrices with orthonormal columns and $\mathbf{\Sigma} \in \mathbb{R}^{n\times(m-1)}$ is a diagonal matrix with real, positive entries, collectively referred to as singular values. The symbol * denotes the complex conjugate transpose. The columns of $\mathbf{U}$ are referred to as proper orthogonal decomposition (POD) modes. These modes are a superposition of patterns or signals in the data. When POD modes are constructed, temporal information is largely ignored - typically, patterns or signals that oscillate at different frequencies are mixed. The rows of $\mathbf{V}^*$ describe the time evolution of the POD modes. The singular values in $\mathbf{\Sigma}$ are ordered hierarchically. The magnitude of a given singular value ranks the relative importance of the corresponding POD mode in $\mathbf{U}$ for describing the data in $\mathbf{X}$, i.e. the first POD mode is more important than the second and so on. Therefore, to calculate a low-rank approximation to $\mathbf{X}$, one can simply choose to keep the leading $\tilde{r}$ columns of $\mathbf{U}$, rows of $\mathbf{V}^*$ and singular values in $\mathbf{\Sigma}$, discarding everything else:

$$\mathbf{X} \approx \tilde{\mathbf{U}}\tilde{\mathbf{\Sigma}}\tilde{\mathbf{V}}^*, \tag{2.145}$$

where $\tilde{\mathbf{U}} \in \mathbb{C}^{n\times\tilde{r}}$, $\tilde{\mathbf{V}} \in \mathbb{C}^{(m-1)\times\tilde{r}}$, $\tilde{\mathbf{\Sigma}} \in \mathbb{R}^{\tilde{r}\times\tilde{r}}$, and $\tilde{r} < m-1$. Choosing the rank $\tilde{r}$ is an important, albeit often subjective, part of this dimensionality reduction procedure. A heuristic approach is to locate 'elbows' in an ordered plot of the singular values. The resulting reduced SVD defines a low-dimensional, orthogonal coordinate system in which the data in $\mathbf{X}$ can be represented. Functions for calculating the SVD

are standard in most programming languages. References regarding the numerical implementation of the SVD can be found in [33].

We are now in a position to outline the DMD algorithm. The first step is to calculate the reduced SVD of the data matrix $\mathbf{X}$, which is given by equation 2.145.

The second step is project $\mathbf{A}$ onto the POD modes in $\tilde{\mathbf{U}}$:

$$\tilde{\mathbf{A}} = \tilde{\mathbf{U}}^* \mathbf{A} \tilde{\mathbf{U}} = \tilde{\mathbf{U}}^* \mathbf{X}' \tilde{\mathbf{V}} \tilde{\mathbf{\Sigma}}^{-1}. \tag{2.146}$$

The reduced matrix $\tilde{\mathbf{A}}$ has the same nonzero eigenvalues as the full matrix $\mathbf{A}$. It is this step that enables one to circumvent calculations that directly involve $\mathbf{A}$.

The third step is to calculate the eigendecomposition of $\tilde{\mathbf{A}}$:

$$\tilde{\mathbf{A}} \mathbf{W} = \mathbf{W} \mathbf{\Lambda}, \tag{2.147}$$

where $\mathbf{W}$ contains the eigenvectors of $\tilde{\mathbf{A}}$, appended column-wise, and $\mathbf{\Lambda}$ is a diagonal matrix containing the eigenvalues.

The final step, developed by Tu et al. [33, 68], is to construct the eigenmodes of $\mathbf{A}$ from $\mathbf{W}$:

$$\mathbf{\Phi} = \mathbf{X}' \tilde{\mathbf{V}} \tilde{\mathbf{\Sigma}}^{-1} \mathbf{W}. \tag{2.148}$$

We subsequently refer to these modes as DMD modes.

With knowledge of $\mathbf{\Phi}$ and $\mathbf{\Lambda}$, one can use the following equation, which can be deduced from equation 2.137, to reconstruct the data in $\mathbf{X}$ and make predictions of future snapshots:

$$\mathbf{x}_k \approx \mathbf{\Phi} \exp(\mathbf{\Omega} k \Delta t) \boldsymbol{b}, \tag{2.149}$$

where $\mathbf{\Omega} = \ln(\mathbf{\Lambda})/\Delta t$ and $\boldsymbol{b}$ is a vector of coefficients. The vector $\boldsymbol{b}$ can be calculated in two ways: either directly using $\boldsymbol{b} = \mathbf{\Phi}^\dagger \mathbf{x}_1$ or indirectly using a projection onto the POD modes. In contrast to POD modes, DMD modes consist of patterns or signals in the data that oscillate, with growth or decay, at the same frequency. The oscillatory behaviour is described by the corresponding eigenvalue. In general, the eigenvalues are complex. The real part encapsulates growth or decay, while the imaginary part encapsulates periodic behaviour. Eigenvalues with a modulus greater than or equal to one are unstable, limiting how far one can use equation 2.149 to accurately and reliably predict into the future.

There are several extensions to the 'base' DMD algorithm outlined above. These include dynamic mode decomposition with control (DMDc) [70], which can disambiguate between the natural and forced components of the dynamics in an actuated system, and bagging, optimised DMD (BOP-DMD) [71], which overcomes two key weaknesses of DMD: sensitivity to measurement noise and a lack of uncertainty quantification. Measurement noise has been shown to cause DMD to calculate a spurious eigendecomposition of $\mathbf{A}$ [71, 72]. Another pertinent limitation of DMD is its inability to handle translations and scaling [33, 66]. Inherent to the application of SVD is the assumption that the spatial and temporal dependencies of the dynamics can be decoupled. In systems where this is not the case, for example, travelling waves, SVD, and therefore DMD, breaks down.

Examples of applying DMD and its extensions, including code, can be found online [73].

2.5.3 Sparse identification of non-linear dynamics (SINDy)

While linear models have their advantages, many systems exhibit dynamics that require the construction of non-linear models. Over the last couple of decades, there have been major developments targeted towards non-linear models in the field of system identification. Seminal work in this area used symbolic regression to learn non-linear governing equations from data [74, 75]. A key limitation of symbolic regression is that it is computationally expensive. Brunton et al. proposed an alternative, more computationally efficient, approach to learning governing equations from data called sparse identification of non-linear dynamics (SINDy) [76]. We outline SINDy below [76].

SINDy was developed in the context of non-linear ODEs, i.e. models of the form

$$\frac{d\mathbf{x}(t)}{dt} = \mathbf{f}(\mathbf{x}(t)), \tag{2.150}$$

where $\mathbf{f}(\mathbf{x}(t))$ is a non-linear function comprised of basis functions that depend on $\mathbf{x}(t)$. At the heart of SINDy is the assumption that $\mathbf{f}(\mathbf{x})$ only contains a few terms, i.e. it is sparse (parsimonious) in the space of possible basis functions. This assumption is valid for many physical systems in an appropriate basis. Under the assumption of sparsity, SINDy frames the problem of model discovery in terms of sparse regression. SINDy models, therefore, balance model accuracy with complexity, avoiding over-fitting and increasing the chances of generalisability.

The first step of SINDy is to collect snapshots of the system of interest and assemble them into a data matrix of the form

$$\mathbf{X} = \begin{bmatrix} \mathbf{x}^T(t_1) \\ \mathbf{x}^T(t_2) \\ \vdots \\ \mathbf{x}^T(t_m) \end{bmatrix} = \begin{bmatrix} x_1(t_1) & x_2(t_1) & \dots & x_n(t_1) \\ x_1(t_2) & x_2(t_2) & \dots & x_n(t_2) \\ \vdots & \vdots & \ddots & \vdots \\ x_1(t_m) & x_2(t_m) & \dots & x_n(t_m) \end{bmatrix}. \tag{2.151}$$

Similarly, a data matrix of first order temporal derivatives must also be assembled:

$$\dot{\mathbf{X}} = \begin{bmatrix} \dot{\mathbf{x}}^T(t_1) \\ \dot{\mathbf{x}}^T(t_2) \\ \vdots \\ \dot{\mathbf{x}}^T(t_m) \end{bmatrix} = \begin{bmatrix} \dot{x}_1(t_1) & \dot{x}_2(t_1) & \dots & \dot{x}_n(t_1) \\ \dot{x}_1(t_2) & \dot{x}_2(t_2) & \dots & \dot{x}_n(t_2) \\ \vdots & \vdots & \ddots & \vdots \\ \dot{x}_1(t_m) & \dot{x}_2(t_m) & \dots & \dot{x}_n(t_m) \end{bmatrix}. \tag{2.152}$$

The derivatives can either be measured directly or calculated from the snapshots in $\mathbf{X}$.

The second step is to construct a library of candidate basis functions that may appear in $\mathbf{f}(\mathbf{x})$. For example,

$$\boldsymbol{\Theta}(\mathbf{X}) = \begin{bmatrix} \mathbf{1} & \mathbf{X} & \mathbf{X}^2 & \dots & \sin(\mathbf{X}) & \dots \end{bmatrix}. \tag{2.153}$$

Here, $\sin(\mathbf{X})$ denotes the element-wise operation of sin on $\mathbf{X}$, and $\mathbf{X}^2$ denotes all the quadratic terms that can be formed from the elements in $\mathbf{X}$, considering one row at a time, i.e.

$$\mathbf{X}^2 = \begin{bmatrix} x_1^2(t_1) & x_1(t_1)x_2(t_1) & \dots & x_1(t_1)x_n(t_1) & x_2^2(t_1) & \dots & x_n^2(t_1) \\ x_1^2(t_2) & x_1(t_2)x_2(t_2) & \dots & x_1(t_2)x_n(t_2) & x_2^2(t_2) & \dots & x_n^2(t_2) \\ \vdots & \vdots & \ddots & \vdots & \vdots & \ddots & \vdots \\ x_1^2(t_m) & x_1(t_m)x_2(t_m) & \dots & x_1(t_m)x_n(t_m) & x_2^2(t_m) & \dots & x_n^2(t_m) \end{bmatrix}. \quad (2.154)$$

The construction of $\boldsymbol{\Theta}(\mathbf{X})$ is down to the user, who may be informed by prior knowledge of the system under consideration. If there is little or no prior knowledge, there are general best-practice principles one can follow [33, 77–81].

The third step is to form the following linear system of equations (c.f. equation 2.150):

$$\dot{\mathbf{X}} = \boldsymbol{\Theta}(\mathbf{X})\boldsymbol{\Xi}, \quad (2.155)$$

where $\boldsymbol{\Xi} = \begin{bmatrix} \boldsymbol{\xi}_1 & \boldsymbol{\xi}_2 & \dots & \boldsymbol{\xi}_n \end{bmatrix}$ is a (sparse) matrix of coefficients to be found. Denoting the columns of $\dot{\mathbf{X}}$ as $\dot{\mathbf{x}}_k$, we can write

$$\dot{\mathbf{x}}_k = \boldsymbol{\Theta}(\mathbf{X})\boldsymbol{\xi}_k, \quad (2.156)$$

therefore each vector $\boldsymbol{\xi}_k$ contains the active terms in the equation of motion for x_k, i.e. the k^{th} variable in $\mathbf{x}$.

The final step is to find a sparse solution to equation 2.155. Based on its computational efficiency and robustness to noise, Brunton et al. [76] advocate using sequential threshold least-squares (STLS), which imposes the assumption that $\mathbf{f}(\mathbf{x})$ is parsimonious. STLS can be summarised as follows:

- Calculate the least squares solution for $\boldsymbol{\Xi}$.
- Threshold all coefficients smaller than ϵ, which is a hyperparameter.
- Calculate a new least squares solution for $\boldsymbol{\Xi}$ using only the non-zero coefficients.
- Threshold all coefficients smaller than ϵ.
- Repeat the above two steps until all non-zero coefficients converge.

An optimal value of ϵ can be determined using cross-validation techniques. It is likely to be beneficial to normalise the columns of $\boldsymbol{\Theta}(\mathbf{X})$ before applying STLS. It may also be necessary to filter $\mathbf{X}$ and $\dot{\mathbf{X}}$ if the data is contaminated with a significant amount of noise.

A key limitation of SINDy is that it requires the state vector is represented in a coordinate system that enables a sparse representation of the dynamics. Moreover, SINDy requires that the library of candidate functions is overcomplete, i.e. it contains the correct sparse model. While prior knowledge of the system might help inform the choice of coordinate system and library of candidate functions, these things are otherwise difficult to determine. That being said, there is an extension to SINDy that opens the door to the joint discovery of coordinates and governing equations [82]. We discuss this in chapter 6. Indeed, the simple formulation of SINDy as a regression problem has enabled the development of many extensions to

the technique. A summary of these extensions can be found in [33]. Pertinent to this thesis is the extension of SINDy to systems described by parametric partial differential equations [83], i.e. partial differential equations (PDEs) with non-constant coefficients. This extension relies on an intermediate extension of SINDy to systems described by PDEs with constant coefficients [84, 85], which we outline first. Before doing so, we wish to note that excellent guidance for applying SINDy can be found online [77–81], as can examples of applying SINDy, including code [86, 87].

2.5.4 Partial differential equation functional identification of non-linear dynamics (PDE-FIND)

Independently of each other, Rudy et al. [84] and Schaeffer [85] generalised the library of candidate functions in SINDy to include partial derivatives and developed new algorithms to solve the ensuing sparse regression problem, enabling the identification of PDEs with constant coefficients, i.e. models of the form

$$\frac{\partial u(x,t)}{\partial t} = \mathrm{f}(u, u_x, u_{xx}, ...), \tag{2.157}$$

where, for simplicity, we have only considered a single variable $u(x,t) \in \mathbb{R}$ and a single spatial dimension, represented by x.

Below, we outline the technique developed by Rudy et al. [84], which is called partial differential equation functional identification of non-linear dynamics (PDE-FIND). In keeping with equation 2.157, we only consider a single variable.

Similarly to SINDy, in PDE-FIND, snapshots of the system, i.e. snapshots of $u(x,t)$, must be collected to form a linear system of equations. For a system in which $u(x,t)$ is measured at n discrete grid points over m time steps, an example linear system of equations is as follows:

$$\underbrace{\begin{pmatrix} u_t(x_1,t_1) \\ u_t(x_2,t_1) \\ \vdots \\ u_t(x_n,t_m) \end{pmatrix}}_{\boldsymbol{U}_t} = \underbrace{\begin{pmatrix} 1 & u(x_1,t_1) & u_x(x_1,t_1) & \dots & u^2u_{xx}(x_1,t_1) \\ 1 & u(x_2,t_1) & u_x(x_2,t_1) & \dots & u^2u_{xx}(x_2,t_1) \\ \vdots & \vdots & \vdots & \ddots & \vdots \\ 1 & u(x_n,t_m) & u_x(x_n,t_m) & \dots & u^2u_{xx}(x_n,t_m) \end{pmatrix}}_{\Theta(\boldsymbol{U})} \boldsymbol{\xi}, \tag{2.158}$$

where $\boldsymbol{U}_t$ a column vector containing first order time derivatives of $u(x,t)$, $\Theta(\boldsymbol{U})$ is a library matrix comprising functions of spatial derivatives of $u(x,t)$ and $\boldsymbol{\xi}$ is a (sparse) column vector of coefficients to be found. If the snapshots of $u(x,t)$ are clean, finite differences can be used to calculate the partial derivatives. Otherwise, polynomial interpolation is an option.

In contrast to SINDy, a different approach to STLS is used to find a sparse solution to equation 2.158. A weakness of STLS is that it often fails to identify a sparse solution when the columns of the library matrix are highly correlated. Augmenting least squares with a regularising term can help avoid this issue. Therefore, Rudy et al. [84] advocate using sequential threshold ridge regression (STRidge), i.e. STLS with the least squares component replaced by ridge regression. In ridge regression, l_2-regularisation is used to penalise non-zero coefficients in the least-squares solution, driving the values of some coefficients towards zero. There are two key hyperparameters associated with STRidge: the tolerance ϵ and a tuning parameter λ. The

latter determines the strength of the regularisation. As with STLS, normalising the columns of $\Theta(\boldsymbol{U})$ is likely to be beneficial when applying STRidge.

An intrinsic limitation of PDE-FIND is related to the challenge of accurately calculating the numerical derivatives of the snapshots. For example, when the snapshots are noisy or low resolution, the task of accurately differentiating the data using numerical methods becomes increasingly difficult. As with SINDy, another limitation of PDE-FIND is that it requires the variable of interest to be measured in a coordinate system that enables a sparse representation of the dynamics. PDE-FIND is also limited by the requirement that the library of candidate functions is overcomplete.

Examples of applying PDE-FIND, including code, can be found online [86–88].

2.5.5 Parametric PDE-FIND

After developing PDE-FIND, Rudy et al. [83] generalised the technique further by incorporating the concept of group sparsity, enabling the identification of parametric PDEs, i.e models of the from of equation 2.157 but with coefficients that depend on time or space. The resulting technique is called parametric PDE-FIND.

The task at hand when applying parametric PDE-FIND is more complex than before. Instead of calculating the correct value of each non-zero coefficient, the correct value of each non-zero coefficient at each time step or grid point must be calculated. A slightly different approach to the one taken in PDE-FIND is required. We outline parametric PDE-FIND below [83].

To outline parametric PDE-FIND, we assume that the coefficients have a spatial dependency. For a system in which $u(x,t)$ is measured at n discrete grid points over m time steps, the data measured at each grid point must be considered separately to construct n linear systems of equations

$$\boldsymbol{U}_t^{(j)} = \Theta(\boldsymbol{U}^{(j)})\boldsymbol{\xi}^{(j)},\ j = 1, ..., n, \tag{2.159}$$

where, for an example library based on the one in equation 2.158,

$$\Theta(\boldsymbol{U}^{(j)}) = \begin{pmatrix} 1 & u(x_j,t_1) & u_x(x_j,t_1) & \dots & u^2u_{xx}(x_j,t_1) \\ 1 & u(x_j,t_2) & u_x(x_j,t_2) & \dots & u^2u_{xx}(x_j,t_2) \\ \vdots & \vdots & \vdots & & \vdots \\ 1 & u(x_j,t_m) & u_x(x_j,t_m) & \dots & u^2u_{xx}(x_j,t_m) \end{pmatrix}. \tag{2.160}$$

Next, the n linear systems of equations need to be assembled into a single hierarchical linear system of equations with a block diagonal structure

$$\underbrace{\begin{pmatrix} \boldsymbol{U}_t^{(1)} \\ \boldsymbol{U}_t^{(2)} \\ \vdots \\ \boldsymbol{U}_t^{(n)} \end{pmatrix}}_{\boldsymbol{U}_t} = \underbrace{\begin{pmatrix} \Theta(\boldsymbol{U}^{(1)}) & & & \\ & \Theta(\boldsymbol{U}^{(2)}) & & \\ & & \ddots & \\ & & & \Theta(\boldsymbol{U}^{(n)}) \end{pmatrix}}_{\Theta} \underbrace{\begin{pmatrix} \boldsymbol{\xi}^{(1)} \\ \boldsymbol{\xi}^{(2)} \\ \vdots \\ \boldsymbol{\xi}^{(n)} \end{pmatrix}}_{\boldsymbol{\xi}}. \tag{2.161}$$

To identify a parametric PDE from this system of equations, a sparse solution must be calculated such that each $\boldsymbol{\xi}^{(j)}$ shares the same sparsity pattern - this concept is called group sparsity. To achieve group sparsity, a modified version of STRidge

called sequential grouped threshold ridge regression (SGTR) can be applied. SGTR groups the columns in 2.161 according to the basis function they represent and thresholds whole groups at a time. Mathematically, for n grid points and d candidate monomial functions, the groups are defined by $\mathcal{G} = \{j + d \cdot i : i = 0, ..., n-1 : j = 1, ..., d\}$. SGTR is outlined in algorithm 1, which we have reproduced from [83] with permission from SIAM. As the algorithm shows, the l_2-norm of the n spatially dependent values of each coefficient is measured. If the l_2-norm is below a threshold value, then the corresponding coefficient is set to zero at all grid points. Once the active terms, i.e. the terms with non-zero coefficients, in the equation have been identified, an unbiased estimate of the coefficient values at each spatial point is obtained using least squares. Since SGTR evaluates the importance of terms that appear in the PDE based on the l_2-norm of their parametric coefficients, differences in the scale of the functions in the library must be taken into account. For this reason, each $\boldsymbol{U}_t^{(j)}$ and column of Θ must be normalised before SGTR is applied.

Algorithm 1 SGTR($\mathbf{A}$,$\mathbf{b}$,$\mathcal{G}$,λ,ϵ,maxit,$f(\mathbf{x}) = ||\mathbf{x}||_2$)

```
# Solves x ≈ A^{-1}b with sparsity imposed on groups g in G
# Initialise coefficients with ridge regression
x = arg min_w ||b − Aw||_2^2 + λ||w||_2^2
# Threshold groups with small f and repeat
for iter = 1, ...,maxit:
    # Remove groups with sufficiently small f(x^(g))
    G = {g ∈ G : f(x^(g)) > ε}
    # Refit x for groups g in G (note this sets x^(g) = 0 for g ∉ G)
    x = arg min_w ||b − Σ_{g∈G} A^(g) w^(g)||_2^2 + λ||w||_2^2
# Get unbiased estimates of coefficients after finding sparsity
x^(G) = arg min_w ||b − Σ_{g∈G} A^(g) w^(g)||_2^2
```

There are four hyperparameters associated with SGTR: the tuning parameter, λ; the tolerance, ϵ; the maximum number of iterations, maxit; and the relevance function, $f(\mathbf{x})$. The choice of these hyperparameters will affect the output of the SGTR algorithm, giving rise to the problem of model selection. To select the optimal model from a collection that have been configured with different hyperparameters, Rudy et al. suggest evaluating each model on a hold-out test data set using the following loss function:

$$\mathcal{L}(\xi) = N \ln \left(\frac{||\Theta\boldsymbol{\xi} - \boldsymbol{U}_t||_2^2}{N} + \nu \right) + 2k, \tag{2.162}$$

where N is the number of rows in Θ, k is the number of non-zero coefficients and ν is a small floor term to avoid overfitting.

When it comes to finding suitable values of the hyperparameters, λ, ϵ and maxit lend themselves to either a grid or random search. In the case of ϵ, an exhaustive range of values to search between can be defined using

$$\epsilon_{\max\,(\min)} = \max_{g \in \mathcal{G}} (\min)\ ||\boldsymbol{\xi}_{\text{ridge}}^{(g)}||_2, \tag{2.163}$$

where $\boldsymbol{\xi}_{\text{ridge}}$ denotes the ridge regression solution to the normalised version of the linear system of equations in equation 2.161. By definition, $\epsilon_{\min}$ is the minimum

tolerance that has any effect on the sparsity of the PDE and $\epsilon_{\max}$ is the minimum tolerance that guarantees all terms to be equal to zero. The choice of $f(\mathbf{x})$ could be informed by expected or desired attributes of the coefficients. For example, one might expect the coefficients of the terms in a PDE describing a physical system to have a certain level of smoothness. Setting $f(\mathbf{x}) = ||\mathbf{x}||_2$ as in algorithm 1 is a good starting point.

A limitation of parametric PDE-FIND is that it does not yield an equation for the temporal or spatial dependency of the coefficients. Other limitations of the technique are the same as those that affect PDE-FIND.

Examples of applying PDE-FIND, including code, can be found online [89].

2.6 Summary

In this chapter, we outlined the key theories and techniques in relation to the work in this thesis. We considered the following:

- The phase behaviour of polymer blends, including the free energy of mixing, the Flory-Huggins theory, free energy curves and phase diagrams
- Mechanisms of phase separation and dissolution in polymer blends, focussing on spinodal decomposition and dissolution through the lens of the CHC and CHC-FHdG theories
- Small-angle scattering, including the relationship between the scattering intensity and the structure factor, the difficulty of deriving an equation of motion for the structure factor, the approximate linear CHC-FHdG and Akcasu equations of motion for the structure factor, and the random phase approximation
- The field of system identification, including DMD, SINDy and parametric PDE-FIND

Chapter 3

Generating time series of synthetic structure factor snapshots

3.1 Introduction

We used three time series of synthetic structure factor snapshots to obtain the results in chapters 4, 5 and 6. In this chapter, we detail how we generated the time series. We include a discussion of how we determined suitable values of the discretisation parameters, Δx and $\Delta \tau$, upon which the generation of credible time series hinges. The aim of this chapter is to provide context for our results and support their credibility.

3.2 Overview and key equations

An overview of the method we used to generate each time series of synthetic structure factor snapshots is as follows:

- We simulated polymeric spinodal decomposition or dissolution using a finite difference scheme, namely a non-dimensionalised and discretised version of the CHC-FHdG equation (equation 2.62).
- During the simulations, we calculated snapshots of the power spectrum using a modified version of equation 2.93.
- After running several repeat simulations, we calculated snapshots of the structure factor by applying a modified version of equation 2.94 to the power spectrum snapshots we accumulated.

There are three key equations: the finite difference scheme and the equations we used to calculate the snapshots of the power spectrum and the structure factor. We present these equations below. In the interest of orderliness, we defer the derivations of the equations to appendix A.

Finite difference scheme

To simulate polymeric spinodal decomposition and dissolution, we applied the following finite difference scheme - a non-dimensionalised and discretised version of equation 2.62 - to a simple cubic lattice with periodic boundary conditions:

$$\begin{aligned}\phi^{m+1}_{j,k,l} =&\phi^{m}_{j,k,l} + \frac{\Delta\tau}{2\Delta x^2}\sum_{nn}\Big[\frac{\chi_c}{2|\chi-\chi_s|}\ln\Big(\frac{\phi^m_{j,k,l}}{1-\phi^m_{j,k,l}}\Big) - \frac{2\chi\phi^m_{j,k,l}}{|\chi-\chi_s|} \\ &+\frac{1}{36}\Big(\frac{1-2\phi^m_{j,k,l}}{(\phi^m_{j,k,l}(1-\phi^m_{j,k,l}))^2}\Big)\frac{1}{4\Delta x^2}\prod_{nn}\phi^m_{j,k,l} \\ &-2\Big(\frac{1}{36\phi^m_{j,k,l}(1-\phi^m_{j,k,l})}\Big)\frac{1}{\Delta x^2}\sum_{nn}\phi^m_{j,k,l}\Big] \\ &+\frac{v_0^{1/2}|\chi-\chi_s|^{1/4}}{\sigma^{3/2}} \\ &\frac{1}{\Delta x}\big[\eta^m_{1;j+1,k,l}-\eta^m_{1;j,k,l}+\eta^m_{2;j,k+1,l}-\eta^m_{2;j,k,l}+\eta^m_{3;j,k,l+1}-\eta^m_{3;j,k,l}\big],\end{aligned} \tag{3.1}$$

where m denotes the number of dimensionless time steps, $\Delta\tau$ is the duration of a dimensionless time step, j, k and l denote the coordinates of each lattice site, Δx is the dimensionless length of each lattice site, $\sum_{nn}$ and $\prod_{nn}$ are short-hand operators, and η_1, η_2 and η_3 are dimensionless Gaussian random variables. The shorthand operators are defined as

$$\sum_{nn} f_{j,k,l} = f_{j+1,k,l} + f_{j-1,k,l} + f_{j,k+1,l} + f_{j,k-1,l} + f_{j,k,l+1} + f_{j,k,l-1} - 6f_{j,k,l} \tag{3.2a}$$

$$\begin{aligned}\prod_{nn} f_{j,k,l} =& f^2_{j+1,k,l} + f^2_{j-1,k,l} + f^2_{j,k+1,l} + f^2_{j,k-1,l} + f^2_{j,k,l+1} + f^2_{j,k,l-1} - \\ &2(f_{j+1,k,l}f_{j-1,k,l} + f_{j,k+1,l}f_{j,k-1,l} + f_{j,k,l+1}f_{j,k,l-1}).\end{aligned} \tag{3.2b}$$

The first and second moments of the Gaussian random variables are given by

$$< \eta^m_{n;j,k,l} >= 0 \tag{3.3a}$$

$$< \eta^m_{n;j,k,l}\eta^{m'}_{n';j',k',l'} >= \frac{\Delta\tau}{\Delta x^3}\delta_{n,n'}\delta_{j,j'}\delta_{k,k'}\delta_{l,l'}\delta_{m,m'}. \tag{3.3b}$$

The dimensionless variables we used to obtain equation 3.1 are as follows:

$$\boldsymbol{x} = \frac{|\chi-\chi_s|^{1/2}}{\sigma}\,\boldsymbol{r} \tag{3.4a}$$

$$\tau = \frac{2Mk_BT|\chi-\chi_s|^2}{\sigma^2 v_0}\,t \tag{3.4b}$$

$$\tilde{\xi}(\boldsymbol{x},\tau) = \frac{\sigma^2 v_0}{2Mk_BT|\chi-\chi_s|^2}\,\xi(\boldsymbol{r},t). \tag{3.4c}$$

These dimensionless variables are inspired by those in [53]. They relate to the fastest growing wavelength and its growth rate during the early stage of spinodal decomposition.

In the context of lattice sites in the top row of a cubic lattice, periodic boundary conditions mean that the nearest neighbours in the vertical direction are the corresponding lattice sites in the bottom row. The nearest neighbours to the left of

lattice sites in the left-most row, to the right of lattice sites in the right-most row, and below lattice sites in the bottom row follow analogously.

For later reference, we denote the total number of time steps in a simulation as $m_{\max}$.

Snapshots of the power spectrum

To calculate snapshots of the power spectrum during the simulations, we used

$$\tilde{P}^m_{n;d} = \Delta x^6 \Big\langle \sum_{j=0}^{N_s-1}\sum_{k=0}^{N_s-1}\sum_{l=0}^{N_s-1} \delta\phi^m_{n;j,k,l}\, e^{-\frac{2\pi i}{N_s}(aj+bk)} \sum_{j'=0}^{N_s-1}\sum_{k'=0}^{N_s-1}\sum_{l'=0}^{N_s-1} \delta\phi^{m'}_{n;j',k',l'} e^{\frac{2\pi i}{N_s}(aj'+bk')} \Big\rangle_R, \tag{3.5}$$

where n allows one to distinguish between repeat simulations, N_s is the number of lattice sites in each dimension of the cubic simulation lattice, a and b are integers in the range $\frac{-(N_s-1)}{2} \leq a, b \leq \frac{N_s-1}{2}$, and $< ... >_R$ denotes a radial average. The radial average can be written explicitly as

$$< f_{a,b} >_R \equiv f_d = \frac{\sum_{a,b \text{ s.t. } \text{round}(\sqrt{a^2+b^2})=d} f_{a,b}}{\sum_{a,b \text{ s.t. } \text{round}(\sqrt{a^2+b^2})=d} 1}, \tag{3.6}$$

where d is an integer in the range $0 \leq d \leq \frac{N_s-1}{2}$.

Snapshots of the structure factor

After implementing N_r repeat simulations, we calculated snapshots of the structure factor using

$$\tilde{S}^m_d = \frac{1}{N_r N_s^3 \Delta x^3} \sum_{n=1}^{N_r} \tilde{P}^m_{n;d}. \tag{3.7}$$

Throughout the remainder of the thesis, we express snapshots of $\tilde{S}^m_d$ as $\tilde{S}(\mathrm{k}, \tau)$, where $\mathrm{k} = \frac{2\pi}{N_s \Delta x} d$ and $\tau = m\Delta\tau$. The symbol k denotes the magnitude of the dimensionless scattering vector, i.e. $\mathrm{k} = |\mathbf{k}|$.

We note that equations 3.5 and 3.7 are non-dimensional and discrete, consistent with equation 3.1. The non-dimensionalisation was performed using equation 3.4a and the dimensionless variables below:

$$\mathrm{k} = \frac{\sigma}{|\chi - \chi_s|^{\frac{1}{2}}} q \tag{3.8a}$$

$$\tilde{S}(\mathrm{k}, \tau) = \frac{|\chi - \chi_s|^{\frac{3}{2}}}{\sigma^3} S(q, t). \tag{3.8b}$$

3.3 Parameter values and initial conditions

Out of the three time series we used to obtain our results, we generated one by simulating dissolution and two by simulating spinodal decomposition. The only parameters we altered between simulations were ϕ_0 and χ. It follows that each

time series corresponds to a unique combination of ϕ_0 and χ values. For ease of reference, we devised a name for each time series based on these values - see table 3.1. There are two values of χ listed for the dissolution time series because of how we generated the initial composition when simulating dissolution - we discuss this below. We implemented five repeat simulations ($N_r = 5$) for each combination of ϕ_0 and χ values. During the simulations, we calculated snapshots of the power spectrum after the first and every 400^{th} time step, i.e. when $m = 1, 400, 800, 1200$, etc. The values of the other parameters we used in the simulations were $\Delta x = 0.25$, $\Delta\tau = 6.25 \times 10^{-5}$, $N_s = 257$, $m_{\max} = 8 \times 10^5$, $N = 2700$, and $\sigma = \sqrt{20} v_0^{\frac{1}{3}}$, where the factor of $\sqrt{20}$ is the square root of the characteristic ratio, $C_\infty = \sigma^2 / v_0^{\frac{2}{3}}$. In the case of the dissolution and the critical shallow time series, the value of χ_s corresponding to $N = 2700$ is $\chi_s = 0.000741$, while in the case of the off-critical deep time series, it is $\chi_s = 0.000814$. We based the values of N and χ on those used in [90–92]. The value of C_∞ corresponds to a relatively stiff polymer [93] - we found using larger values of C_∞ increased the stability of the simulations. We used trial and error to determine suitable values of Δx and $\Delta\tau$, i.e. values of Δx and $\Delta\tau$ that can be used in the simulations to generate time series that are independent of these values. Further details on this are provided in section 3.6. To put $\Delta x = 0.25$ into context, table 3.2 contains the value of $\Delta r / R_g$ corresponding to each time series, where Δr is the dimensional equivalent of Δx (see equation 3.4a). The ratio $\Delta r / R_g$ relates the size of a lattice site to the size of the polymers.

Time series name	ϕ_0	χ
Dissolution	0.5	$0.000765 \rightarrow 0.000716$
Critical shallow (spinodal decomposition)	0.5	0.000765
Off-critical deep (spinodal decomposition)	0.35	0.000937

Table 3.1: The values of ϕ_0 and χ corresponding to each time series we generated. The terms 'shallow' and 'deep' refer to the relative quench depth ($\chi - \chi_s$) represented by the value of χ.

Time series name	$\Delta r / R_g$
Dissolution	2.41
Critical shallow (spinodal decomposition)	2.41
Off-critical deep (spinodal decomposition)	1.06

Table 3.2: The value of $\Delta r / R_g$ corresponding to each time series we generated.

In the simulations of critical shallow and off-critical deep spinodal decomposition, we set the initial composition at each lattice site equal to the corresponding value of ϕ_0. After the first time step, the Gaussian random variable term in equation 3.1 introduced random fluctuations into the composition, initiating spinodal decomposition. In the simulations of dissolution, we generated the initial composition, i.e. the composition at the time dissolution is initiated, by simulating spinodal decomposition with $\phi_0 = 0.5$ and $\chi = 0.000765$ for the first 1.6×10^5 time steps. We then initiated dissolution by making a step change to $\chi = 0.000716$. The functions of $|\chi - \chi_s|$ in equation 3.1 are a result of the non-dimensionalisation. To avoid

the scaling between the dimensionless and real variables changing between the two stages of the dissolution simulations, we chose the initial and final values of χ such that $|0.000765 - \chi_s| = |\chi_s - 0.000716|$.

3.4 Implementing the simulations

We implemented the simulations in Julia [94]. To keep the computation time to a minimum, we made use of the CUDA.jl package [95]. This allowed us to implement equation 3.1 on a graphics processing unit (GPU), which we accessed on the University of Sheffield's high-performance computer, Stanage. The code we developed to implement the simulations is available on GitHub [96]. Text files from which the time series can be calculated using equation 3.7 are also located there.

3.5 Conforming with the small-k limit

As we have already mentioned, equation 3.1 is non-dimensionalised and discretised version of equation 2.62. Since equation 2.62 is only valid in the small-q limit (see sections 2.4.8 and 2.4.9), it follows that equation 3.1 is only valid in the corresponding small-k limit. The small-k limit is somewhat ambiguously defined as $\mathrm{k}r_g << 1$, where r_g is the dimensionless radius of gyration. To determine whether to truncate the snapshots of the synthetic structure factor we generated to conform with the small-k limit when obtaining our results, we attempted to quantify the small-k limit.

We determined inequalities that specify the small-k limit corresponding to each time series. We then compared these inequalities with the k-values associated with the constituent snapshots. In the case of the dissolution and critical-shallow time series, we determined the small-k limit corresponds to $\mathrm{k} < 5$, and in the case of the off-critical deep time series, we determined $\mathrm{k} < 3$. We outline the calculations we performed to determine these inequalities in appendix A. Given that we used $N_s = 257$ and $\Delta x = 0.25$ in the simulations, each snapshot of the synthetic structure factor we generated consists of 129 values, with the 129^{th} value corresponding to $\mathrm{k} \approx 12.5$. Therefore, we concluded that truncating the snapshots is necessary to conform with the small-k limit.

3.6 Choosing suitable values of Δx and $\Delta \tau$ to use in the simulations

3.6.1 Background

When using finite difference simulations to generate data, one must be careful in the selection of Δx and $\Delta \tau$ values [53,56,97]. A guiding principle for choosing a suitable value of Δx is that it needs to be much less than the smallest physical length scale modelled in the system. The value of Δx places an upper limit on the value of $\Delta \tau$. In general, one can be confident they have used small enough values of Δx and $\Delta \tau$ when the data generated by a simulation is independent of these values, i.e. it does not change when smaller values are used.

3.6.2 Methodology

We used trial and error to choose the values of Δx and $\Delta\tau$ listed in section 3.3. To facilitate this, we generated different versions of the dissolution, critical shallow, and off-critical deep time series using several combinations of Δx, $\Delta\tau$, N_s and $m_{\max}$. For each 'type' of time series, i.e. dissolution, critical shallow, and off-critical deep, we compared the time evolution of the synthetic structure factor snapshots corresponding to each combination of Δx, $\Delta\tau$, N_s and $m_{\max}$. We looked for consistent overlap between snapshots to determine which values of Δx and $\Delta\tau$ could be used to generate time series that are independent of these values. The specific combinations of Δx, $\Delta\tau$, N_s and $m_{\max}$ we investigated are listed in table 3.3. We chose the values of N_s and $m_{\max}$ to fix the size of the system and dimensionless timespan of the simulations, respectively.

Label	Δx	$\Delta\tau$	N_s	$m_{\max}$
A	1	1×10^{-3}	65	5×10^4
B	0.5	2.5×10^{-4}	129	2×10^5
C	0.25	6.25×10^{-5}	257	8×10^5
D	0.25	3.125×10^{-5}	257	1.6×10^6
E	0.2	4×10^{-5}	321	1.25×10^6

Table 3.3: The combinations of discretisation parameters we used to search for suitable values of Δx and $\Delta\tau$ to use in the simulations. The labels are provided to make the table easier to refer to.

3.6.3 Results

First, we focus on the different versions of the dissolution time series. Figure 3.1 compares the time evolution of the synthetic dissolution structure factor snapshots corresponding to each combination of Δx, $\Delta\tau$, N_s and $m_{\max}$ listed in table 3.3. For ease of reference, we use the labels in table 3.3 to distinguish between the different versions of the time series. The snapshots corresponding to B, C, D and E overlap at each value of τ. For $\tau < 20$, there are discrepancies between these snapshots and the snapshots corresponding to A. These observations suggest that the versions of the dissolution time series corresponding to B, C, D and E are independent of the corresponding values of Δx and $\Delta\tau$, while the version corresponding to A is not.

We mention in passing that dissolution provides a straightforward opportunity to verify that we derived and coded equations 3.1, 3.5 and 3.7 correctly. The synthetic structure factor snapshots should approach the curve given by equation 2.106, i.e. de Gennes' equation for the static structure factor, or, more specifically, a version of equation 2.106 that has been non-dimensionalised consistently with equations 3.1, 3.5 and 3.7. In figure 3.1f, the non-dimensionalised static structure factor is plotted alongside the synthetic structure factor snapshots. The static structure factor curve overlaps with the synthetic structure factor snapshots. This observation would be unlikely if we made a mistake in deriving or coding any of equations 3.1, 3.5 and 3.7, therefore it indicates no mistakes were made. For $\tau > 15$, the synthetic structure factor snapshots exhibit fluctuations. We believe this effect stems from the Gaussian random variable term in equation 3.1.

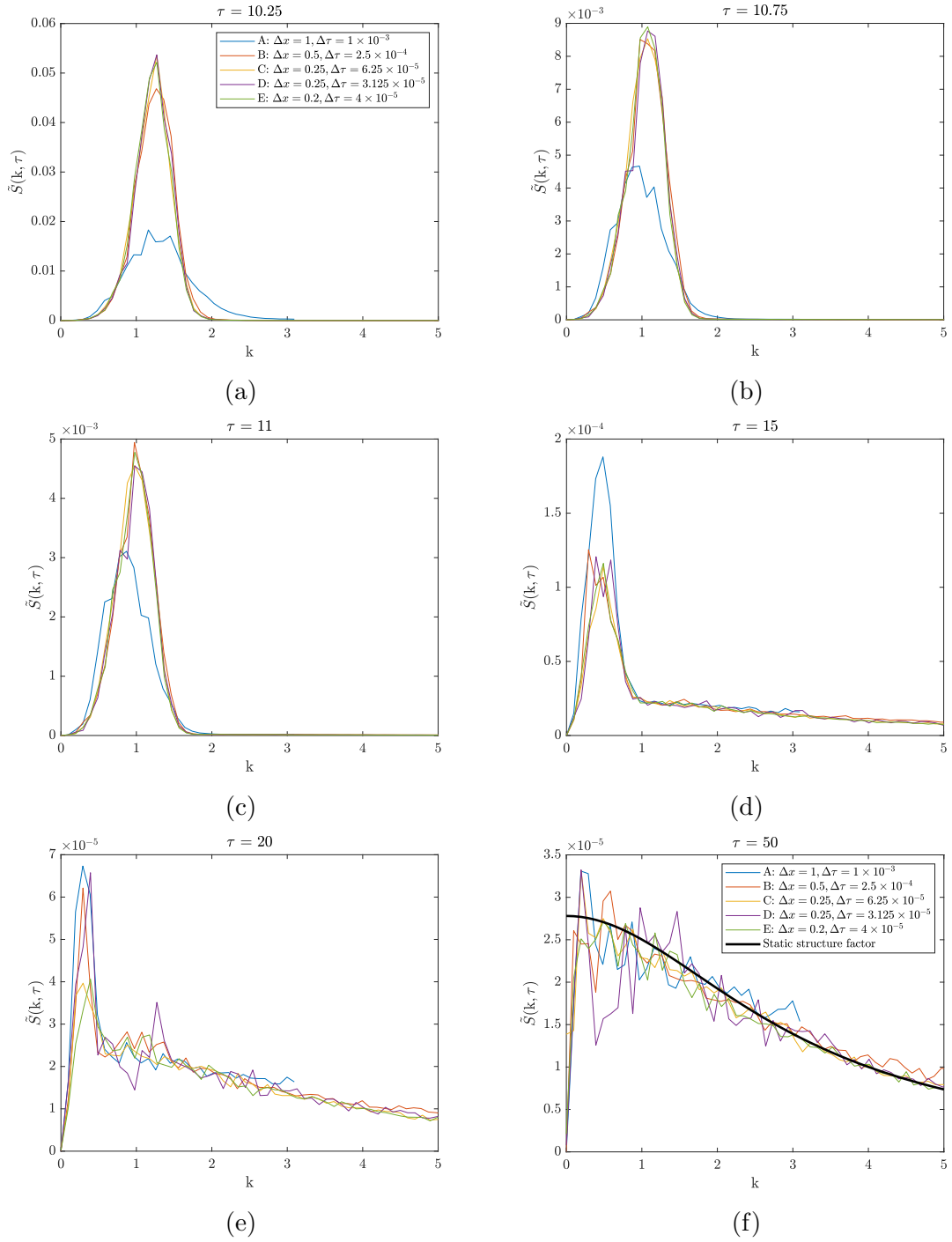

Figure 3.1: A comparison between snapshots of the synthetic structure factor generated using different combinations of Δx, $\Delta\tau$, N_s and $m_{\max}$ in the simulations of dissolution. In panel (f), a non-dimensionalised version of de Gennes' equation for the static structure factor (equation 2.106) is plotted. In the simulations of dissolution, dissolution was initiated at $\tau = 10$. The data in the figure corresponds to times that lag behind the onset of dissolution by 0.25, 2, 4, 8, 16 and 32 dimensionless time units, respectively.

We now focus on the different versions of the critical shallow time series. Figure 3.2 compares the time evolution of the synthetic critical shallow structure factor snapshots corresponding to each combination of Δx, $\Delta\tau$, N_s and $m_{\max}$ listed in table 3.3. Again, we use the labels in table 3.3 to distinguish between the different versions of the time series. The snapshots corresponding to C, D and E overlap at each value of τ. For $\tau < 5$, there are discrepancies between these snapshots and the snapshots corresponding to B, and, for all values of τ, there are discrepancies between these snapshots and the snapshots corresponding to A. These observations suggest that the versions of the critical shallow time series corresponding to C, D and E are independent of the corresponding values of Δx and $\Delta\tau$, while the versions corresponding to A and B are not. We obtained similar findings for the different versions of the off-critical deep time series.

To conclude, we found the following combinations of Δx and $\Delta\tau$ values can be used to generate versions of the dissolution, critical shallow and off-critical deep time series that are independent of these values: $\Delta x = 0.25$ & $\Delta\tau = 6.25 \times 10^{-5}$ (C), $\Delta x = 0.25$ & $\Delta\tau = 3.125 \times 10^{-5}$ (D) and $\Delta x = 0.2$ & $\Delta\tau = 4 \times 10^{-5}$ (E).

3.7 Summary

In this chapter, we detailed how we generated the time series of synthetic structure factor snapshots we used to obtain our results. We provided the following:

- An overview of the method we used to generate each time series.
- The key equations on which the method is based.
- The parameter values and initial conditions we used in the method.
- A link to the code we developed to implement the bulk of the method.
- An explanation as to how we conformed with the small-k limit.
- A discussion of how we determined suitable values of Δx and $\Delta\tau$ to use in the simulations.

In appendix A, we outline the derivations of the key equations and the calculations we performed to determine the small-k limit inequalities.

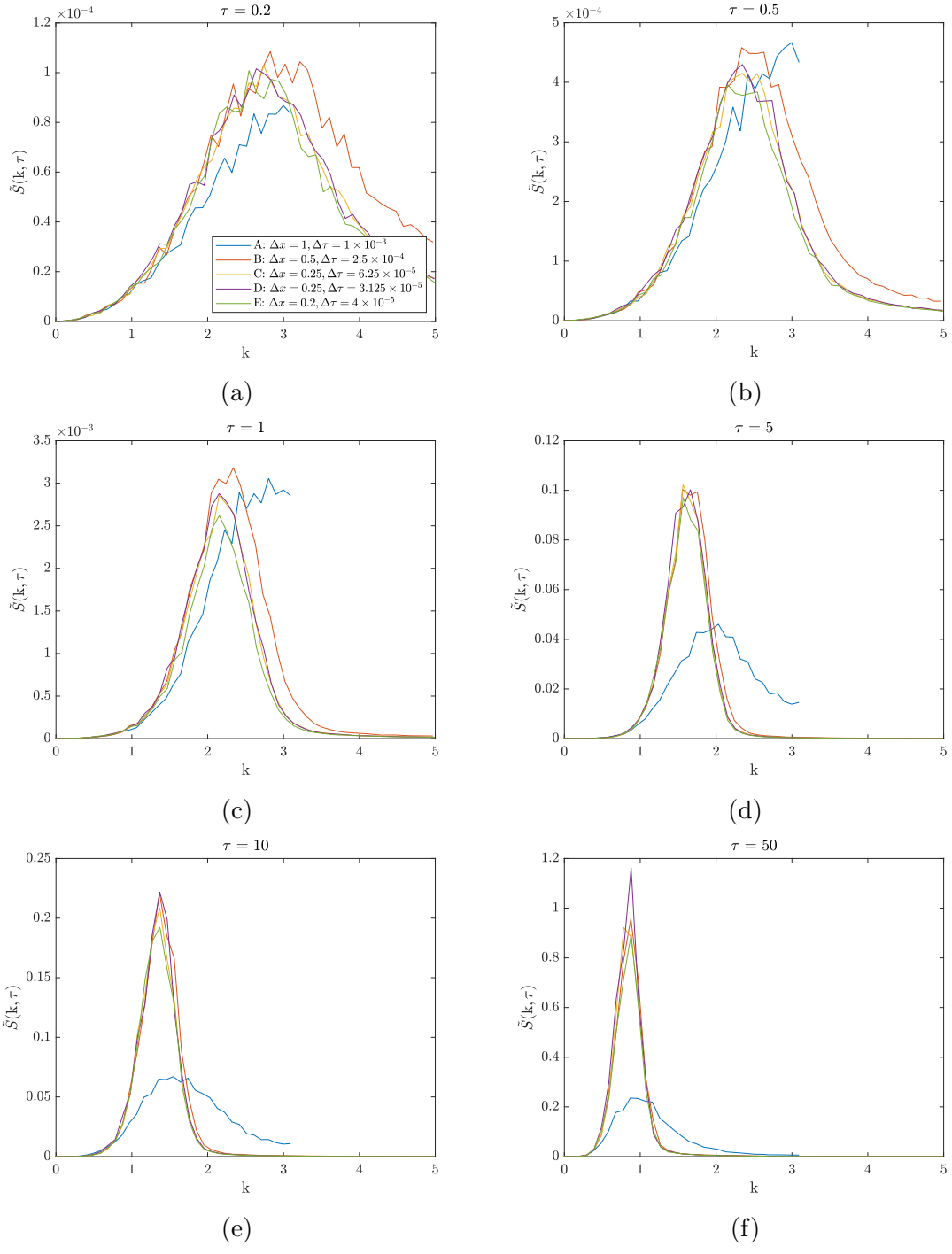

Figure 3.2: A comparison between snapshots of the synthetic structure factor generated using different combinations of Δx, $\Delta \tau$, N_s and $m_{\max}$ in the simulations of critical shallow spinodal decomposition.

Chapter 4

Testing the Akcasu equation for the time evolution of the structure factor during polymeric spinodal decomposition and dissolution

4.1 Introduction

In sections 2.4.6 and 2.4.7, we introduced two equations for modelling the time evolution of the structure factor during polymeric spinodal decomposition and dissolution: the linear CHC-FHdG equation (equation 2.104) and the Akcasu equation (equation 2.108). Since its development, the linear CHC-FHdG equation has been widely adopted to analyse scattering data [2, 10, 27–29]. However, while it has certainly proved useful, it is only valid under restrictive conditions and assumptions [8, 26, 30]. This situation motivated Akcasu et al. to develop their equation of motion, which is non-linear [19, 31, 32]. The Akcasu equation is an approximate one. Including non-linear terms in the equation of motion for the structure factor causes it to become unclosed [17–19]. Therefore, the 'full' equation of motion is an intractable hierarchy of coupled differential equations, and a truncation scheme is required to solve it.

In contrast to the linear CHC-FHdG equation, the Akcasu equation has not been widely adopted to analyse scattering data. We believe this is because of insufficient testing. There has been no reported comparison between the predictions of the Akcasu equation and numerical or experimental scattering data in the case of spinodal decomposition. In the case of dissolution, a comparison with experimental data was performed by Akcasu et al. [31]. The comparison revealed a quantitative discrepancy between theory and experiment, which worsened as the dissolution time increased. Akcasu et al. used best-guess values of the molecular and thermodynamic parameters to solve their equation since some of the parameters are hard to measure. It is unclear whether the Akcasu equation failed as a result of the equation being inadequate or incorrect parameter values being used. In this chapter, we shed light on this question by comparing the numerical solution to the Akcasu equation applied to dissolution with synthetic structure factor snapshots from the dissolution time series. We also test the Akcasu equation applied to spinodal decomposition using synthetic structure factor snapshots from the critical shallow time series.

4.2 Derivation of the Akcasu equation

To the best of our knowledge, the derivation of the Akcasu equation has not been published in its entirety. In this section, we reproduce the derivation as detailed in [19, 31, 32], including additional details where appropriate.

The starting point of the derivation is the CHC-FHdG equation (equation 2.62). Upon writing $\phi(\boldsymbol{r},t) = \phi_0 + \delta\phi(\boldsymbol{r},t)$, performing a power series expansion up to and including third order non-linearities, and gathering terms, we obtain

$$\begin{aligned}
\frac{\partial\delta\phi(\boldsymbol{r},t)}{\partial t} =& \frac{Mk_BT}{v_0}\nabla^2\Big[\frac{1}{N}\ln(\phi_0) - \frac{1}{N}\ln(1-\phi_0) + \chi(1-2\phi_0) \\
&+ \frac{\delta\phi}{N}\Big(\frac{1}{\phi_0} + \frac{1}{1-\phi_0} - 2N\chi\Big) + \frac{\delta\phi^2}{N}\Big(\frac{-1}{2\phi_0^2} + \frac{1}{2(1-\phi_0)^2}\Big) \\
&+ \frac{\delta\phi^3}{N}\Big(\frac{1}{3\phi_0^3} + \frac{1}{3(1-\phi_0)^3}\Big) - \frac{\sigma^2}{18}\nabla^2\delta\phi\Big(\frac{1}{\phi_0} + \frac{1}{1-\phi_0}\Big) \\
&- \frac{\sigma^2}{18}(\nabla^2\delta\phi)\delta\phi\Big(\frac{-1}{\phi_0^2} + \frac{1}{(1-\phi_0)^2}\Big) - \frac{\sigma^2}{18}(\nabla^2\delta\phi)\delta\phi^2\Big(\frac{1}{\phi_0^3} + \frac{1}{(1-\phi_0)^3}\Big) \\
&- \frac{\sigma^2}{36}(\nabla\delta\phi)^2\Big(\frac{-1}{\phi_0^2} + \frac{1}{(1-\phi_0)^2}\Big) - \frac{\sigma^2}{36}(\nabla\delta\phi)^2\delta\phi\Big(\frac{2}{\phi_0^3} + \frac{2}{(1-\phi_0)^3}\Big)\Big] \\
&+ \xi(\boldsymbol{r},t). \qquad (4.1)
\end{aligned}$$

As in the linear theory, to derive an equation of motion for the structure factor, we must map equation 4.1 into Fourier space. Before doing this, it is convenient to express equation 4.1 in terms of the Fourier components of $\delta\phi(\boldsymbol{r}) = \frac{1}{(2\pi)^3}\int d^3q e^{i\boldsymbol{q}\cdot\boldsymbol{r}}\delta\phi(\boldsymbol{q})$ [51]. After simplifying, we obtain

$$\begin{aligned}
\frac{\partial\delta\phi(\boldsymbol{r},t)}{\partial t} =& \frac{Mk_BT}{v_0}\nabla^2\Big[\frac{1}{(2\pi)^3N}\Big(\frac{1}{\phi_0} + \frac{1}{1-\phi_0} - 2N\chi\Big)\int d^3q_1 e^{i\boldsymbol{q}_1\cdot\boldsymbol{r}}\delta\phi(\boldsymbol{q}_1) \\
&+ \frac{1}{(2\pi)^6N}\Big(\frac{-1}{2\phi_0^2} + \frac{1}{2(1-\phi_0)^2}\Big)\prod_{j=1,2}\int d^3q_j e^{i\boldsymbol{q}_j\cdot\boldsymbol{r}}\delta\phi(\boldsymbol{q}_j) \\
&+ \frac{1}{(2\pi)^9N}\Big(\frac{1}{3\phi_0^3} + \frac{1}{3(1-\phi_0)^3}\Big)\prod_{j=1,2,3}\int d^3q_j e^{i\boldsymbol{q}_j\cdot\boldsymbol{r}}\delta\phi(\boldsymbol{q}_j) \\
&+ \frac{\sigma^2}{18(2\pi)^3}\Big(\frac{1}{\phi_0} + \frac{1}{1-\phi_0}\Big)\int d^3q_1 q_1^2 e^{i\boldsymbol{q}_1\cdot\boldsymbol{r}}\delta\phi(\boldsymbol{q}_1) \\
&+ \frac{\sigma^2}{18(2\pi)^6}\Big(\frac{-1}{\phi_0^2} + \frac{1}{(1-\phi_0)^2}\Big)\int d^3q_1 q_1^2 e^{i\boldsymbol{q}_1\cdot\boldsymbol{r}}\delta\phi(\boldsymbol{q}_1)\int d^3q_2 e^{i\boldsymbol{q}_2\cdot\boldsymbol{r}}\delta\phi(\boldsymbol{q}_2) \\
&+ \frac{\sigma^2}{18(2\pi)^9}\Big(\frac{1}{\phi_0^3} + \frac{1}{(1-\phi_0)^3}\Big)\int d^3q_1 q_1^2 e^{i\boldsymbol{q}_1\cdot\boldsymbol{r}}\delta\phi(\boldsymbol{q}_1)\prod_{j=2,3}\int d^3q_j e^{i\boldsymbol{q}_j\cdot\boldsymbol{r}}\delta\phi(\boldsymbol{q}_j) \\
&+ \frac{\sigma^2}{36(2\pi)^6}\Big(\frac{-1}{\phi_0^2} + \frac{1}{(1-\phi_0)^2}\Big)\int d^3q_1\boldsymbol{q}_1 e^{i\boldsymbol{q}_1\cdot\boldsymbol{r}}\delta\phi(\boldsymbol{q}_1)\cdot\int d^3q_2\boldsymbol{q}_2 e^{i\boldsymbol{q}_2\cdot\boldsymbol{r}}\delta\phi(\boldsymbol{q}_2) \\
&+ \frac{\sigma^2}{36(2\pi)^9}\Big(\frac{2}{\phi_0^3} + \frac{2}{(1-\phi_0)^3}\Big) \\
&\int d^3q_1\boldsymbol{q}_1 e^{i\boldsymbol{q}_1\cdot\boldsymbol{r}}\delta\phi(\boldsymbol{q}_1)\cdot\int d^3q_2\boldsymbol{q}_2 e^{i\boldsymbol{q}_2\cdot\boldsymbol{r}}\delta\phi(\boldsymbol{q}_2)\int d^3q_3 e^{i\boldsymbol{q}_3\cdot\boldsymbol{r}}\delta\phi(\boldsymbol{q}_3)\Big] \\
&+ \xi(\boldsymbol{r},t). \qquad (4.2)
\end{aligned}$$

Next, mapping equation 4.2 into Fourier space, making use of the result $\int d^3r\; e^{(i(\sum_j \boldsymbol{q}_j)\cdot \boldsymbol{r})} = (2\pi)^3\delta(\sum_j \boldsymbol{q}_j)$ [51], and simplifying, yields

$$\begin{aligned}
\frac{\partial\delta\phi(\boldsymbol{q},t)}{\partial t} = \frac{-Mk_BTq^2}{v_0}\Big[\delta\phi(\boldsymbol{q})\Big\{\frac{1}{N}\Big(\frac{1}{\phi_0}+\frac{1}{1-\phi_0}-2N\chi\Big)+\frac{\sigma^2}{18}\Big(\frac{1}{\phi_0}+\frac{1}{1-\phi_0}\Big)q^2\Big\}\\
+\frac{1}{(2\pi)^3}\Big(\int d^3q_1\int d^3q_2\;\delta(\boldsymbol{q}-\boldsymbol{q}_1-\boldsymbol{q}_2)\delta\phi(\boldsymbol{q}_1)\delta\phi(\boldsymbol{q}_2)\\
\Big\{\frac{1}{N}\Big(\frac{-1}{2\phi_0^2}+\frac{1}{2(1-\phi_0)^2}\Big)+\frac{\sigma^2}{18}\Big(\frac{-1}{\phi_0^2}+\frac{1}{(1-\phi_0)^2}\Big)q_1^2\\
+\frac{\sigma^2}{36}\Big(\frac{-1}{\phi_0^2}+\frac{1}{(1-\phi_0)^2}\Big)\boldsymbol{q}_1\cdot\boldsymbol{q}_2\Big\}\Big)\\
+\frac{1}{(2\pi)^6}\Big(\int d^3q_1\int d^3q_2\int d^3q_3\;\delta(\boldsymbol{q}-\boldsymbol{q}_1-\boldsymbol{q}_2-\boldsymbol{q}_3)\delta\phi(\boldsymbol{q}_1)\delta\phi(\boldsymbol{q}_2)\delta\phi(\boldsymbol{q}_3)\\
\Big\{\frac{1}{N}\Big(\frac{1}{3\phi_0^3}+\frac{1}{3(1-\phi_0)^3}\Big)+\frac{\sigma^2}{18}\Big(\frac{1}{\phi_0^3}+\frac{1}{(1-\phi_0)^3}\Big)q_1^2\\
+\frac{\sigma^2}{36}\Big(\frac{2}{\phi_0^3}+\frac{2}{(1-\phi_0)^3}\Big)\boldsymbol{q}_1\cdot\boldsymbol{q}_2\Big\}\Big)\Big]\\
+\xi(\boldsymbol{q},t).
\end{aligned}\tag{4.3}$$

From equation 4.3, the following vertex functions can be defined

$$\begin{aligned}
\Gamma_2(\boldsymbol{q}_1,\boldsymbol{q}_2) = \frac{1}{N}\Big(\frac{-1}{2\phi_0^2}+\frac{1}{2(1-\phi_0)^2}\Big)+\frac{\sigma^2}{18}\Big(\frac{-1}{\phi_0^2}+\frac{1}{(1-\phi_0)^2}\Big)q_1^2\\
+\frac{\sigma^2}{36}\Big(\frac{-1}{\phi_0^2}+\frac{1}{(1-\phi_0)^2}\Big)\boldsymbol{q}_1\cdot\boldsymbol{q}_2
\end{aligned}\tag{4.4a}$$

$$\begin{aligned}
\Gamma_3(\boldsymbol{q}_1,\boldsymbol{q}_2) = \frac{1}{N}\Big(\frac{1}{3\phi_0^3}+\frac{1}{3(1-\phi_0)^3}\Big)+\frac{\sigma^2}{18}\Big(\frac{1}{\phi_0^3}+\frac{1}{(1-\phi_0)^3}\Big)q_1^2\\
+\frac{\sigma^2}{36}\Big(\frac{2}{\phi_0^3}+\frac{2}{(1-\phi_0)^3}\Big)\boldsymbol{q}_1\cdot\boldsymbol{q}_2.
\end{aligned}\tag{4.4b}$$

The vertex functions capture the coupling between composition fluctuations with different wavevectors, i.e. the coupling between different fluctuation modes. As it stands, Γ_2 and Γ_3 are incomplete. The vertex function Γ_2 should capture the coupling between pairs of fluctuations modes with wavevectors that add up to $\boldsymbol{q}$. As such, Γ_2 must be a symmetric function of $\boldsymbol{q}_1$ and $\boldsymbol{q}_2$. Similarly, the vertex function Γ_3 should capture the coupling between triplets of fluctuations modes with wavevectors that add up to $\boldsymbol{q}$. As such, Γ_3 must be a symmetric function of $\boldsymbol{q}_1$, $\boldsymbol{q}_2$ and $\boldsymbol{q}_3$. The complete vertex functions are the average over all possible permutational pairs of the relevant wavevectors. For example, in the case of Γ_2:

$$\begin{aligned}
\Gamma_2(\boldsymbol{q}_1,\boldsymbol{q}_2) = \frac{1}{N}\Big(\frac{-1}{2\phi_0^2}+\frac{1}{2(1-\phi_0)^2}\Big)\\
+\frac{\sigma^2}{36}\Big(\frac{-1}{\phi_0^2}+\frac{1}{(1-\phi_0)^2}\Big)[q_1^2+q_2^2+\frac{1}{2}(\boldsymbol{q}_1\cdot\boldsymbol{q}_2+\boldsymbol{q}_2\cdot\boldsymbol{q}_1)].
\end{aligned}\tag{4.5}$$

Setting $\boldsymbol{q}=\boldsymbol{q}_1+\boldsymbol{q}_2$ and making the substitution $\boldsymbol{q}_1\cdot\boldsymbol{q}_2+\boldsymbol{q}_2\cdot\boldsymbol{q}_1 = q^2-q_1^2-q_2^2$ yields

$$\Gamma_2(\boldsymbol{q},\boldsymbol{q}_1,\boldsymbol{q}_2) = \frac{1}{N}\Big(\frac{-1}{2\phi_0^2}+\frac{1}{2(1-\phi_0)^2}\Big)+\frac{\sigma^2}{72}\Big(\frac{-1}{\phi_0^2}+\frac{1}{(1-\phi_0)^2}\Big)[q^2+q_1^2+q_2^2]. \quad (4.6)$$

Similarly, in the case of $\Gamma_3(\boldsymbol{q},\boldsymbol{q}_1,\boldsymbol{q}_2,\boldsymbol{q}_3)$, we obtain

$$\begin{aligned}\Gamma_3(\boldsymbol{q},\boldsymbol{q}_1,\boldsymbol{q}_2,\boldsymbol{q}_3) = \frac{1}{N}\Big(\frac{1}{3\phi_0^3}+\frac{1}{3(1-\phi_0)^3}\Big)& \\ +\frac{\sigma^2}{108}\Big(\frac{1}{\phi_0^3}+\frac{1}{(1-\phi_0)^3}\Big)[q^2+q_1^2+q_2^2+q_3^2].&\end{aligned} \quad (4.7)$$

In terms of these complete, symmetric vertex functions, equation 4.3 becomes

$$\begin{aligned}\frac{\partial\delta\phi(\boldsymbol{q},t)}{\partial t} &= R(q)\delta\phi(\boldsymbol{q}) \\ &- \frac{Mk_BTq^2}{v_0(2\pi)^3}\int d^3q_1\int d^3q_2\;\delta(\boldsymbol{q}-\boldsymbol{q}_1-\boldsymbol{q}_2)\delta\phi(\boldsymbol{q}_1)\delta\phi(\boldsymbol{q}_2)\Gamma_2(\boldsymbol{q},\boldsymbol{q}_1,\boldsymbol{q}_2) \\ &- \frac{Mk_BTq^2}{v_0(2\pi)^6}\int d^3q_1\int d^3q_2\int d^3q_3 \\ &\qquad \delta(\boldsymbol{q}-\boldsymbol{q}_1-\boldsymbol{q}_2-\boldsymbol{q}_3)\delta\phi(\boldsymbol{q}_1)\delta\phi(\boldsymbol{q}_2)\delta\phi(\boldsymbol{q}_3)\Gamma_3(\boldsymbol{q},\boldsymbol{q}_1,\boldsymbol{q}_2,\boldsymbol{q}_3) \\ &+ \xi(\boldsymbol{q},t),\end{aligned} \quad (4.8)$$

where we identified the coefficient of $\delta\phi(\boldsymbol{q})$ as the amplification factor, $R(q)$ (see equation 2.66). Substituting equation 4.8 and its complex conjugate into equation 2.95 yields the following equation of motion for the structure factor

$$\begin{aligned}\frac{\partial S(\boldsymbol{q},t)}{\partial t} &= 2\Big[R(q)S(\boldsymbol{q},t) \\ &- \frac{Mk_BTq^2}{v_0V(2\pi)^3}\int d^3q_1\int d^3q_2 \\ &\qquad \delta(\boldsymbol{q}-\boldsymbol{q}_1-\boldsymbol{q}_2)<\delta\phi(\boldsymbol{q}_1)\delta\phi(\boldsymbol{q}_2)\delta\phi(-\boldsymbol{q})>\Gamma_2(\boldsymbol{q},\boldsymbol{q}_1,\boldsymbol{q}_2) \\ &- \frac{Mk_BTq^2}{v_0V(2\pi)^6}\int d^3q_1\int d^3q_2\int d^3q_3 \\ &\quad \delta(\boldsymbol{q}-\boldsymbol{q}_1-\boldsymbol{q}_2-\boldsymbol{q}_3)<\delta\phi(\boldsymbol{q}_1)\delta\phi(\boldsymbol{q}_2)\delta\phi(\boldsymbol{q}_3)\delta\phi(-\boldsymbol{q})>\Gamma_3(\boldsymbol{q},\boldsymbol{q}_1,\boldsymbol{q}_2,\boldsymbol{q}_3)\Big] \\ &+ \frac{1}{V}<\xi(\boldsymbol{q},t)\delta\phi(-\boldsymbol{q})>+\frac{1}{V}<\xi(-\boldsymbol{q},t)\delta\phi(\boldsymbol{q})>.\end{aligned} \quad (4.9)$$

Equation 4.9 is not closed, as discussed in section 2.4.5. Calculating the time evolution of the structure factor using equation 4.9 would require us to solve an infinite hierarchy of coupled differential equations. To obtain a tractable equation of motion for the structure factor, Akcasu et al. approximated the composition fluctuations in Fourier space as a Gaussian process with zero mean. Making use of

Isserlis' theorem [98], the third-order correlation function can then be set equal to zero and the fourth-order correlation function can be written in terms of the second-order correlation function, i.e. $S(\boldsymbol{q},t)$. Specifically, making use of the permutational symmetry of the integrals in equation 4.9:

$$< \delta\phi(\boldsymbol{q}_1)\delta\phi(\boldsymbol{q}_2)\delta\phi(-\boldsymbol{q}) >= 0 \tag{4.10a}$$

$$< \delta\phi(\boldsymbol{q}_1)\delta\phi(\boldsymbol{q}_2)\delta\phi(\boldsymbol{q}_3)\delta\phi(-\boldsymbol{q}) >= 3(2\pi)^6 S(\boldsymbol{q},t)S(\boldsymbol{q}_2,t)\delta(\boldsymbol{q}-\boldsymbol{q}_1)\delta(\boldsymbol{q}_2+\boldsymbol{q}_3). \tag{4.10b}$$

Substituting equations 4.10a and 4.10b into equation 4.9 yields

$$\begin{aligned}\frac{\partial S(\boldsymbol{q},t)}{\partial t} &= 2\Big[R(q)S(\boldsymbol{q},t) \\ &\quad - \frac{3S(\boldsymbol{q},t)Mk_BTq^2}{v_0V}\int d^3q_1\int d^3q_2\int d^3q_3 \\ &\qquad \delta(\boldsymbol{q}-\boldsymbol{q}_1-\boldsymbol{q}_2-\boldsymbol{q}_3)S(\boldsymbol{q}_2,t)\delta(\boldsymbol{q}-\boldsymbol{q}_1)\delta(\boldsymbol{q}_2+\boldsymbol{q}_3)\Gamma_3(\boldsymbol{q},\boldsymbol{q}_1,\boldsymbol{q}_2,\boldsymbol{q}_3)\Big] \\ &\quad + \frac{1}{V}C(\boldsymbol{q}).\end{aligned} \tag{4.11}$$

Upon integrating, making use of the result $\delta(0) = \frac{1}{(2\pi)^3}\int d^3r e^{i\boldsymbol{r}\cdot 0} = \frac{V}{(2\pi)^3}$, we obtain

$$\frac{\partial S(\boldsymbol{q},t)}{\partial t} = 2R(q)S(\boldsymbol{q},t)\Big[1-\frac{3Mk_BTq^2}{(2\pi)^3 v_0 R(q)}\int d^3q_2\ \Gamma_3(\boldsymbol{q},\boldsymbol{q}_2)S(\boldsymbol{q}_2,t)\Big]+\frac{1}{V}C(\boldsymbol{q}), \tag{4.12}$$

where $\Gamma_3(\boldsymbol{q},\boldsymbol{q}_2) = \frac{1}{N}\Big(\frac{1}{3\phi_0^3}+\frac{1}{3(1-\phi_0)^3}\Big)+\frac{\sigma^2}{108}\Big(\frac{1}{\phi_0^3}+\frac{1}{(1-\phi_0)^3}\Big)(2q^2+2q_2^2)$. Equation 4.12 can be written more compactly as

$$\frac{\partial S(q,t)}{\partial t} = 2R(q)S(q,t)[1+Z(q,t)]+\frac{1}{V}C(q), \tag{4.13}$$

where we have made use of the fact that that polymer blends are, in general, isotropic by writing $S(\boldsymbol{q},t)$ as $S(q,t)$. The product $R(q)[1+Z(q,t)]$ can be thought of as a modified amplification factor.

To determine $C(q)$, we consider the $t\to\infty$ limit of equation 4.13, requiring that $S(q,t)\to S_{\text{eq}}(q)$, hence

$$C(q) = -2VR(q)S_{\text{eq}}(q)[1+Z_{\text{eq}}(q)], \tag{4.14}$$

which allows us to calculate $C(q)$ in terms of $S_{\text{eq}}(q)$ consistently with the closure approximations. The equilibrium structure factor must be specified by independent calculations. At this point in the derivation, we must specialise to either dissolution or spinodal decomposition.

4.2.1 Dissolution

In dissolution, $S_{\text{eq}}(q)$ can be set equal to de Gennes' random phase approximation for the static structure factor. In the small-q limit, this is given by equation 2.106. With an equation for $S_{\text{eq}}(q)$, we can proceed with the calculation of $Z_{\text{eq}}(q)$ to complete the specification of the noise term. We start with the equation for $Z(q,t)$, which, in full, is given by

$$Z(q,t) = \frac{-Mk_BTq^2}{(2\pi)^3 v_0 R(q)}\Big(\frac{1}{\phi_0^3} + \frac{1}{(1-\phi_0)^3}\Big) \\ \Big\{\Big(\frac{1}{N} + \frac{\sigma^2 q^2}{18}\Big)\int d^3q_2\ S(q_2,t) + \frac{\sigma^2}{18}\int d^3q_2\ q_2^2\ S(q_2,t)\Big\}. \tag{4.15}$$

Writing the integrals in terms of spherical polar coordinates and simplifying yields

$$Z(q,t) = \frac{-Mk_BTq^2}{2\pi^2 v_0 R(q)}\Big(\frac{1}{\phi_0^3} + \frac{1}{(1-\phi_0)^3}\Big) \\ \Big\{\Big(\frac{1}{N} + \frac{\sigma^2 q^2}{18}\Big)\int_0^{q_{\text{cut}}} dq_2\ q_2^2\ S(q_2,t) + \frac{\sigma^2}{18}\int_0^{q_{\text{cut}}} dq_2\ q_2^4\ S(q_2,t)\Big\}, \tag{4.16}$$

where the upper limit q_{cut} is introduced to ensure the integral is convergent at all times. The physical significance of q_{cut} is that only fluctuation modes with wavenumbers between 0 and q_{cut} are coupled together. Akcasu et al. advocate setting $q_{\text{cut}} \approx q_c$, where q_c is the inverse correlation length

$$q_c = \sqrt{\frac{36(\chi_s - \chi)(\phi_0(1-\phi_0))}{\sigma^2}}. \tag{4.17}$$

The inverse correlation length is defined by expressing equation 2.106 in the form $S_{\text{eq}}(q) = \frac{S(0)}{(1+(\frac{q}{q_c})^2)}$. Akcasu et al. introduced the parameter $\alpha = \frac{q_{\text{cut}}}{q_c}$ as a measure of the range of mode coupling. This is treated as an adjustable parameter in the theory. Rewriting the integrals in equation 4.16 in terms of $\tilde{q} = \frac{q}{q_c}$ yields

$$Z(q,t) = \frac{-Mk_BTq^2q_c^3}{2\pi^2 v_0 R(q)}\Big(\frac{1}{\phi_0^3} + \frac{1}{(1-\phi_0)^3}\Big) \\ \Big\{\Big(\frac{1}{N} + \frac{\sigma^2 q^2}{18}\Big)\int_0^{\alpha} d\tilde{q}_2\ \tilde{q}_2^2\ S(\tilde{q}_2 q_c,t) + \frac{\sigma^2 q_c^2}{18}\int_0^{\alpha} d\tilde{q}_2\ \tilde{q}_2^4\ S(\tilde{q}_2 q_c,t)\Big\}. \tag{4.18}$$

In the limit $t \to \infty$, replacing $S(q,t)$ with $S_{\text{eq}}(q)$, we obtain

$$Z_{\text{eq}}(q) = \frac{-Mk_BTq^2q_c^3}{2\pi^2 R(q)}\Big(\frac{1}{\phi_0^3} + \frac{1}{(1-\phi_0)^3}\Big)(2\chi_s - 2\chi)^{-1} \\ \Big\{\Big(\frac{1}{N} + \frac{\sigma^2 q^2}{18}\Big)\int_0^{\alpha} d\tilde{q}_2\ \tilde{q}_2^2\ (1+\tilde{q}_2^2)^{-1} + \frac{\sigma^2 q_c^2}{18}\int_0^{\alpha} d\tilde{q}_2\ \tilde{q}_2^4\ (1+\tilde{q}_2^2)^{-1}\Big\}. \tag{4.19}$$

Upon evaluating the integrals, we arrive at

$$Z_{\text{eq}}(q) = \frac{-Mk_BTq^2q_c^3}{2\pi^2 R(q)}\Big(\frac{1}{\phi_0^3} + \frac{1}{(1-\phi_0)^3}\Big)(2\chi_s - 2\chi)^{-1} \\ \Big\{\Big(\frac{1}{N} + \frac{\sigma^2 q^2}{18}\Big)(\alpha - \tan^{-1}(\alpha)) + \frac{\sigma^2 q_c^2}{18}\Big(\frac{1}{3}\alpha^3 - \alpha + \tan^{-1}(\alpha)\Big)\Big\}. \tag{4.20}$$

Substituting equations 2.66, 2.106 and 4.20 into equation 4.14, the noise term in the case of dissolution is given by

$$C(q) = 2Mk_BTVq^2\Big[1 + \frac{q_c^3 v_0}{8\pi^2}\Big(\frac{1}{\phi_0^3} + \frac{1}{(1-\phi_0)^3}\Big)(\chi_s - \chi)^{-2}\Big(1 + \Big(\frac{q}{q_c}\Big)^2\Big)^{-1} \\ \Big\{\Big(\frac{1}{N} + \frac{\sigma^2 q^2}{18}\Big)(\alpha - \tan^{-1}(\alpha)) + \frac{\sigma^2 q_c^2}{18}\Big(\frac{1}{3}\alpha^3 - \alpha + \tan^{-1}(\alpha)\Big)\Big\}\Big], \tag{4.21}$$

where we made use of equation 2.105.

Putting everything together, the Akcasu equation applied to dissolution is given by equation 4.13, where $R(q)$ is given by equation 2.66, $Z(q,t)$ is given by equation 4.18, and $C(q)$ is given by equation 4.21.

The linear CHC-FHdG equation applied to dissolution is recovered from the Akcasu equation when we set $Z(q,t) = Z_{\text{eq}}(q) = 0$.

4.2.2 Small temperature jump spinodal decomposition

In the case of spinodal decomposition, Akcasu et al. argued that the static structure factor at the final temperature is unknown [99, 100], meaning equation 4.14 cannot be applied. They suggested a workaround for this in the case of small changes in χ, i.e. small temperature jumps. Namely, assuming we know the value of χ in the one-phase region before the initiation of spinodal decomposition, denoted χ_i, we could make the approximation $C(q,\chi_f) \approx C(q,\chi_i)$, where χ_f is the value of χ inside the spinodal.

Since $\chi = \chi_f > \chi_s$ in spinodal decomposition, we must define the inverse correlation length in a different way to equation 4.17. Following Akcasu et al., we define

$$q_{c,2} = \sqrt{\frac{36(\chi - \chi_s)(\phi_0(1-\phi_0))}{\sigma^2}}. \tag{4.22}$$

Putting everything together, the Akcasu equation applied to spinodal decomposition under the assumption of a small temperature jump is given by equation 4.13, where $R(q)$ is given by equation 2.66 with $\chi = \chi_f$, $Z(q,t)$ is given by equation 4.18 with $q_c = q_{c,2}$ and $\chi = \chi_f$, and $C(q)$ is given by equation 4.21 with $\chi = \chi_i$.

The linear CHC-FHdG equation applied to spinodal decomposition is recovered from the Akcasu equation when we set $Z(q,t) = Z_{\text{eq}}(q) = 0$.

4.2.3 General spinodal decomposition

Contrary to Akcasu et al., we argue that, in the case of spinodal decomposition, the static structure factor is known at the final temperature. The equilibrium state consists of two coexisting phases with compositions given by the coexistence curve [6, 101]. This situation is shown on a phase diagram in figure 4.1. The coexisting phases are stable, hence the random phase approximation for the static structure factor can be applied to each phase and the overall static structure factor is the average of the two:

$$S_{\text{eq}}(q) = \frac{1}{2}(S_{\text{eq}}(q,\phi_{A'}) + S_{\text{eq}}(q,\phi_{A''})). \tag{4.23}$$

We have assumed that the contribution of the interface to the scattering is negligible in a fully phase-separated system. Making use of equation 2.106, we obtain

$$S_{\text{eq}}(q) = v_0\Big[2(\chi_s' - \chi) + \frac{\sigma^2}{18}\Big(\frac{1}{\phi_{A'}(1-\phi_{A'})}\Big)q^2\Big]^{-1}, \tag{4.24}$$

where $\chi_s' = \frac{2}{4N\phi_{A'}(1-\phi_{A'})}$ is the value of the interaction parameter on the spinodal at the coexistence compositions. In line with equation 4.17, we define the inverse

correlation length as

$$q_c' = \sqrt{\frac{36(\chi_s' - \chi)(\phi_{A'}(1-\phi_{A'}))}{\sigma^2}}. \tag{4.25}$$

Putting everything together, the Akcasu equation applied to general spinodal decomposition is given by equation 4.13, where $R(q)$ is given by equation 2.66, $Z(q,t)$ is given by equation 4.18 with $q_c = q_c'$ and $\chi_s = \chi_s'$, and

$$\begin{aligned} C(q) =& 2Mk_BTVq^2 \\ & \Big[\Big((\chi_s - \chi) + \frac{\sigma^2}{36}\Big(\frac{1}{\phi_0(1-\phi_0)}\Big)q^2\Big)\Big((\chi_s' - \chi) + \frac{\sigma^2}{36}\Big(\frac{1}{\phi_{A'}(1-\phi_{A'})}\Big)q^2\Big)^{-1} \\ & + \frac{q_c'^3 v_0}{8\pi^2}\Big(\frac{1}{\phi_0^3} + \frac{1}{(1-\phi_0)^3}\Big)(\chi_s' - \chi)^{-2}\Big(1 + \Big(\frac{q}{q'_c}\Big)^2\Big)^{-1} \\ & \Big\{\Big(\frac{1}{N} + \frac{\sigma^2 q^2}{18}\Big)(\alpha - \tan^{-1}(\alpha)) + \frac{\sigma^2 q_c'^2}{18}\Big(\frac{1}{3}\alpha^3 - \alpha + \tan^{-1}(\alpha)\Big)\Big\}\Big], \end{aligned} \tag{4.26}$$

which follows from substituting $R(q)$, $S_{\text{eq}}(q)$ (equation 4.24) and the corresponding equation for $Z_{\text{eq}}(q)$, i.e. equation 4.20 with $q_c = q_c'$ and $\chi_s = \chi_s'$, into equation 4.14.

The linear CHC-FHdG equation applied to spinodal decomposition is not recovered from the Akcasu equation when we set $Z(q,t) = Z_{\text{eq}}(q) = 0$. We refer to the resulting linear equation as the linear Akcasu equation applied to general spinodal decomposition.

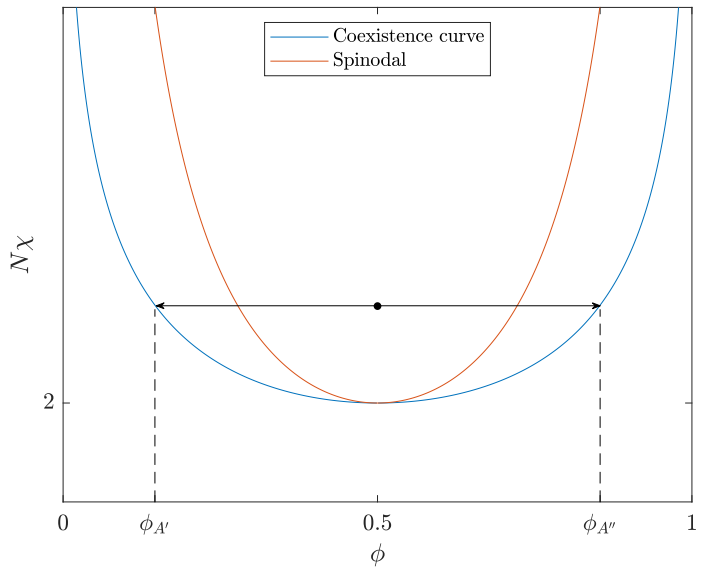

Figure 4.1: A phase diagram illustrating the evolution of the average composition of a critical, binary, symmetric polymer blend during spinodal decomposition. The black dot denotes the state of the blend at the start of spinodal decomposition. The compositions $\phi_{A'}$ and $\phi_{A''}$ define the equilibrium state of the blend and, therefore, the limit of phase separation.

4.3 Methodology

To test the Akcasu equation applied to dissolution, we compared its numerical solution with synthetic structure factor snapshots from the dissolution time series and the numerical solution to the linear CHC-FHdG equation applied to dissolution. To test the Akcasu equation applied to spinodal decomposition under the assumption of a small temperature jump, we compared its numerical solution with synthetic structure factor snapshots from the critical shallow time series and the numerical solution to the linear CHC-FHdG equation applied to spinodal decomposition. Finally, to test the Akcasu equation applied to general spinodal decomposition, we compared its numerical solution with synthetic structure factor snapshots from the critical shallow time series and the numerical solution to the linear Akcasu equation applied to general spinodal decomposition.

4.3.1 Dimensionless equations

In order to compare their numerical solutions with the synthetic structure factor snapshots, we substituted the dimensionless variables in equations 3.4b, 3.8a and 3.8b into the aforementioned equations.

Dissolution

The dimensionless Akcasu equation applied to dissolution is given by

$$\frac{\partial \tilde{S}(\mathrm{k},\tau)}{\partial \tau} = r(\mathrm{k})\tilde{S}(\mathrm{k},\tau)[1+Z(\mathrm{k},\tau)] + C(\mathrm{k}), \tag{4.27}$$

where

$$r(\mathrm{k}) = \frac{-2\mathrm{k}^2}{|\chi-\chi_s|}\Big((\chi_s-\chi)+\frac{|\chi-\chi_s|\mathrm{k}^2}{36\phi_0(1-\phi_0)}\Big) \tag{4.28a}$$

$$\begin{aligned} Z(\mathrm{k},\tau) =& \frac{-\mathrm{k}^2}{2\pi^2|\chi-\chi_s|r(\mathrm{k})}\Big(\frac{1}{\phi_0^3}+\frac{1}{(1-\phi_0)^3}\Big) \\ & \Big\{\Big(\frac{1}{N}+\frac{|\chi-\chi_s|}{18}\mathrm{k}^2\Big)\int_0^{\mathrm{k_{cut}}} d\mathrm{k}\mathrm{k}^2\tilde{S}(\mathrm{k},\tau) + \frac{|\chi-\chi_s|}{18}\int_0^{\mathrm{k_{cut}}} d\mathrm{k}\mathrm{k}^4\tilde{S}(\mathrm{k},\tau)\Big\} \end{aligned} \tag{4.28b}$$

$$\begin{aligned} C(\mathrm{k}) =& \frac{v_0|\chi-\chi_s|^{\frac{1}{2}}\mathrm{k}^2}{\sigma^3}\Big[1 \\ & + \frac{v_0 q_c^3}{8\pi^2(\chi_s-\chi)^2}\Big(\frac{1}{\phi_0^3}+\frac{1}{(1-\phi_0)^3}\Big)\Big(1+\frac{|\chi-\chi_s|\mathrm{k}^2}{36(\chi_s-\chi)\phi_0(1-\phi_0)}\Big)^{-1} \\ & \Big\{\Big(\frac{1}{N}+\frac{|\chi-\chi_s|}{18}\mathrm{k}^2\Big)(\alpha-\tan^{-1}(\alpha)) + \frac{\sigma^2 q_c^2}{18}\Big(\frac{1}{3}\alpha^3-\alpha+\tan^{-1}(\alpha)\Big)\Big\}\Big]. \end{aligned} \tag{4.28c}$$

The upper limit in the integrals is given by $\mathrm{k_{cut}} = \alpha \mathrm{k}_c$, where k_c is related to q_c via equation 3.8a.

In the dimensionless linear CHC-FHdG equation applied to dissolution, $r(\mathrm{k})$ is given by equation 4.28a, $Z(\mathrm{k},\tau)=0$ and $C(\mathrm{k})$ is given by equation 4.28c but with the second term, i.e. the term after the plus sign inside the square brackets, set equal to zero.

Small temperature jump spinodal decomposition

In the dimensionless Akcasu equation applied to spinodal decomposition under the assumption of a small temperature jump, $r(\mathrm{k})$, $Z(\mathrm{k},\tau)$ and $C(\mathrm{k})$ are given by

$$r(\mathrm{k}) = \frac{-2\mathrm{k}^2}{|\chi-\chi_s|}\Big((\chi_s-\chi_f)+\frac{|\chi-\chi_s|\mathrm{k}^2}{36\phi_0(1-\phi_0)}\Big) \tag{4.29a}$$

$$\begin{aligned} Z(\mathrm{k},\tau) =& \frac{-\mathrm{k}^2}{2\pi^2|\chi-\chi_s|r(\mathrm{k})}\Big(\frac{1}{\phi_0^3}+\frac{1}{(1-\phi_0)^3}\Big) \\ & \Big\{\Big(\frac{1}{N}+\frac{|\chi-\chi_s|}{18}\mathrm{k}^2\Big)\int_0^{\mathrm{k_{cut}}} d\mathrm{k}\mathrm{k}^2\tilde{S}(\mathrm{k},\tau)+\frac{|\chi-\chi_s|}{18}\int_0^{k_{\mathrm{cut}}} d\mathrm{k}\mathrm{k}^4\tilde{S}(\mathrm{k},\tau)\Big\} \end{aligned} \tag{4.29b}$$

$$\begin{aligned} C(\mathrm{k}) =& \frac{v_0|\chi-\chi_s|^{\frac{1}{2}}\mathrm{k}^2}{\sigma^3}\Big[1 \\ & + \frac{v_0 q_c^3}{8\pi^2(\chi_s-\chi_i)^2}\Big(\frac{1}{\phi_0^3}+\frac{1}{(1-\phi_0)^3}\Big)\Big(1+\frac{|\chi-\chi_s|\mathrm{k}^2}{36(\chi_s-\chi_i)\phi_0(1-\phi_0)}\Big)^{-1} \\ & \Big\{\Big(\frac{1}{N}+\frac{|\chi-\chi_s|}{18}\mathrm{k}^2\Big)(\alpha-\tan^{-1}(\alpha))+\frac{\sigma^2 q_c^2}{18}\Big(\frac{1}{3}\alpha^3-\alpha+\tan^{-1}(\alpha)\Big)\Big\}\Big]. \end{aligned} \tag{4.29c}$$

The upper limit in the integrals is given by $\mathrm{k_{cut}} = \alpha \mathrm{k}_{c,2}$, where $\mathrm{k}_{c,2}$ is related to $q_{c,2}$ via equation 3.8a.

In the dimensionless linear CHC-FHdG equation applied to spinodal decomposition, $r(\mathrm{k})$ is given by equation 4.29a, $Z(\mathrm{k},\tau) = 0$ and $C(\mathrm{k})$ is given by equation 4.29c but with the second term set equal to zero.

General spinodal decomposition

In the dimensionless Akcasu equation applied to general spinodal decomposition, $r(\mathrm{k})$, $Z(\mathrm{k},\tau)$ and $C(\mathrm{k})$ are given by

$$r(\mathrm{k}) = \frac{-2\mathrm{k}^2}{|\chi-\chi_s|}\Big((\chi_s-\chi)+\frac{|\chi-\chi_s|\mathrm{k}^2}{36\phi_0(1-\phi_0)}\Big) \tag{4.30a}$$

$$\begin{aligned} Z(\mathrm{k},\tau) =& \frac{-\mathrm{k}^2}{2\pi^2|\chi-\chi_s|r(\mathrm{k})}\Big(\frac{1}{\phi_0^3}+\frac{1}{(1-\phi_0)^3}\Big) \\ & \Big\{\Big(\frac{1}{N}+\frac{|\chi-\chi_s|}{18}\mathrm{k}^2\Big)\int_0^{k_{\mathrm{cut}}} d\mathrm{k}\mathrm{k}^2\tilde{S}(\mathrm{k},\tau)+\frac{|\chi-\chi_s|}{18}\int_0^{\mathrm{k_{cut}}} d\mathrm{k}\mathrm{k}^4\tilde{S}(\mathrm{k},\tau)\Big\} \end{aligned} \tag{4.30b}$$

$$\begin{aligned} C(\mathrm{k}) =& \frac{v_0|\chi-\chi_s|^{\frac{1}{2}}\mathrm{k}^2}{\sigma^3}\Big[\Big((\chi_s-\chi)+\frac{|\chi-\chi_s|\mathrm{k}^2}{36\phi_0(1-\phi_0)}\Big)\Big((\chi_s'-\chi)+\frac{|\chi-\chi_s|\mathrm{k}^2}{36\phi_{A'}(1-\phi_{A'})}\Big)^{-1} \\ & + \frac{v_0 q_c'^3}{8\pi^2(\chi_s'-\chi)^2}\Big(\frac{1}{\phi_0^3}+\frac{1}{(1-\phi_0)^3}\Big)\Big(1+\frac{|\chi-\chi_s|\mathrm{k}^2}{36(\chi_s'-\chi)\phi_{A'}(1-\phi_{A'})}\Big)^{-1} \\ & \Big\{\Big(\frac{1}{N}+\frac{|\chi-\chi_s|}{18}\mathrm{k}^2\Big)(\alpha-\tan^{-1}(\alpha))+\frac{\sigma^2 q_c'^2}{18}\Big(\frac{1}{3}\alpha^3-\alpha+\tan^{-1}(\alpha)\Big)\Big\}\Big]. \end{aligned} \tag{4.30c}$$

The upper limit in the integrals is given by $\mathrm{k}_{\mathrm{cut}} = \alpha \mathrm{k}'_c$, where k'_c is related to q'_c via equation 3.8a.

In the dimensionless linear Akcasu equation applied to general spinodal decomposition, $r(\mathrm{k})$ is given by equation 4.30a, $Z(\mathrm{k}, \tau) = 0$ and $C(\mathrm{k})$ is given by equation 4.30c but with the second term set equal to zero.

4.3.2 Solving the dimensionless equations

To calculate the numerical solutions to the dimensionless equations, we made approximations consistent with those used to solve equation A.2. Namely, we approximated continuous time as a series of discrete time steps of duration $\Delta\tau$ and the continuous wavenumber as $\mathrm{k} = \frac{2\pi}{N\Delta x} d$, where d is an integer in the range $0 \leq d \leq \frac{N_s - 1}{2}$. We approximated the time derivative as a forward finite difference scheme and calculated the integrals using the trapezoidal method. The numerical solutions to the resulting discretised equations were calculated by integrating both sides of the equations over a single time step, approximating the integration as a Riemann sum with a single term. We ensured the numerical solutions were independent of the value of $\Delta\tau$.

We set $N = 2700$, $\phi_0 = 0.5$ and $\sigma = \sqrt{20} v_0^{\frac{1}{3}}$, and we investigated three different values of α: 0.5, 1 and 1.5.

In the equations corresponding to dissolution, we set $\chi = 0.000716$. The initial condition was the snapshot corresponding to $\tau = 10$ in the dissolution time series. We note that in the simulations of dissolution used to generate the dissolution time series, dissolution was initiated at $\tau = 10$.

In the equations corresponding to spinodal decomposition under the assumption of a small temperature jump, we set $\chi_i = 0.000716$ and $\chi_f = \chi = 0.000765$. In the equations corresponding to general spinodal decomposition, we set $\chi = 0.000765$ and $\phi_{A'} = 0.348$. We calculated the value of $\phi_{A'}$ using a phase diagram. For both sets of spinodal decomposition equations, the initial condition was the snapshot corresponding to $\tau = 6.25 \times 10^{-5}$ in the critical shallow time series, i.e. the first snapshot in the time series.

4.4 Results and analysis

4.4.1 Dissolution

We now present our findings from testing the Akcasu equation applied to dissolution. Figure 4.2 compares synthetic structure factor snapshots from the dissolution time series with the numerical solutions to the dimensionless Akcasu equation and the dimensionless linear CHC-FHdG equation. Three solutions to the Akcasu equation were calculated, corresponding to $\alpha = 0.5$, 1 and 1.5. These values of α relate to $\mathrm{k}_{\mathrm{cut}} = 1.5$, $\mathrm{k}_{\mathrm{cut}} = 3$ and $\mathrm{k}_{\mathrm{cut}} = 4.5$, respectively.

The Akcasu equation describes the time evolution of the synthetic structure factor snapshots more accurately than the linear CHC-FHdG equation for $10 < \tau < 18$: there is more overlap between the synthetic structure factor snapshots and the solutions to the Akcasu equation than there is between the synthetic structure factor snapshots and the solution to the linear CHC-FHdG equation. For $\tau \geq 18$, the solutions to the Akcasu equation more or less coincide with the solution to the

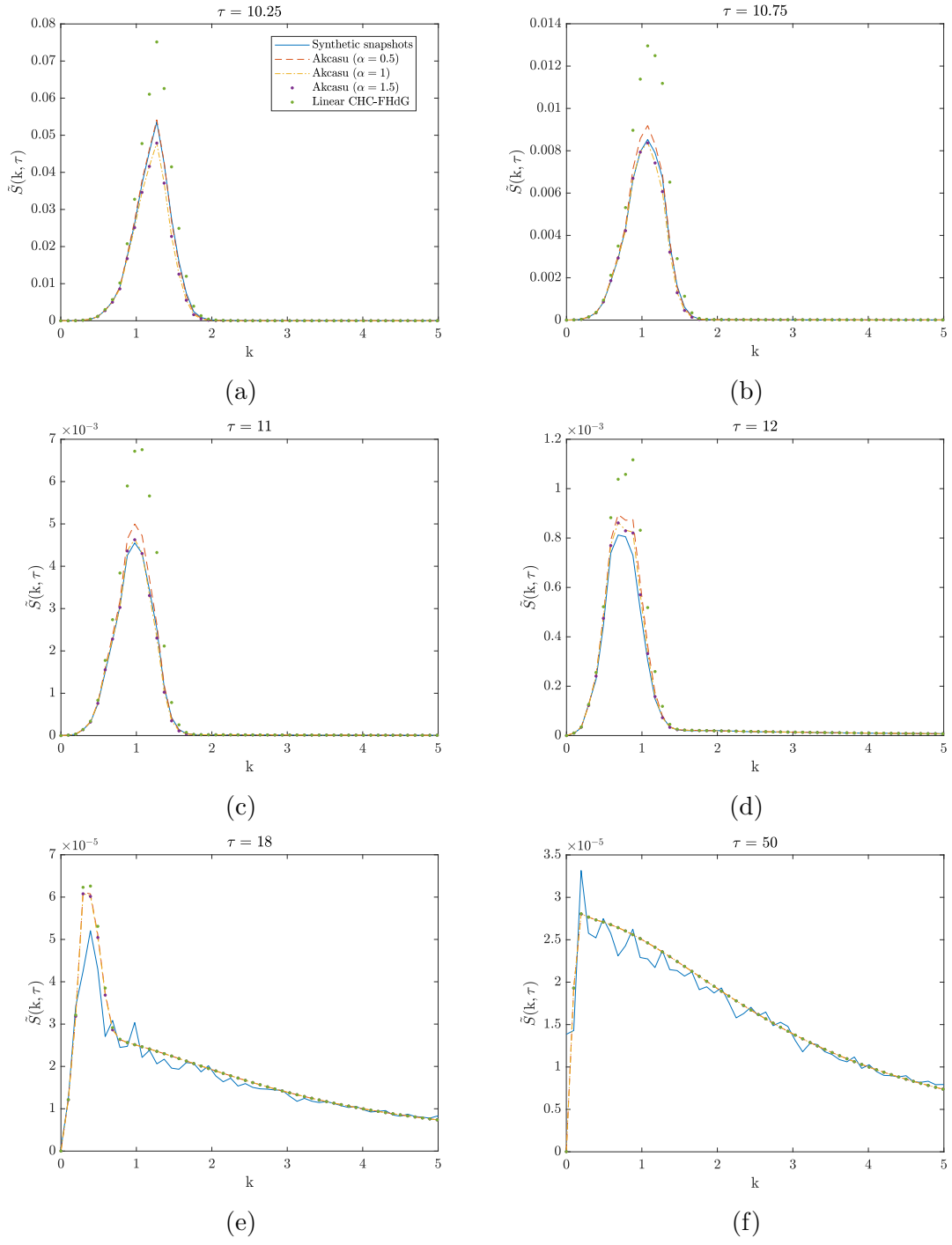

Figure 4.2: A comparison between synthetic structure factor snapshots from the dissolution time series and the numerical solutions to the dimensionless Akcasu equation applied to dissolution and the linear CHC-FHdG equation applied to dissolution. Three solutions to the Akcasu equation were calculated, corresponding to $\alpha = 0.5$, 1 and 1.5. These values of α relate to $k_{cut} = 1.5$, $k_{cut} = 3$ and $k_{cut} = 4.5$, respectively. We note that in the simulations of dissolution used to generate the dissolution time series, dissolution was initiated at $\tau = 10$. The data corresponds to times that lag behind the onset of dissolution by 0.25, 0.75, 1, 2, 8 and 40 dimensionless time units, respectively.

linear CHC-FHdG equation. We infer that the increased accuracy of the Akcasu equation compared to the linear CHC-FHdG equation for $10 < \tau < 18$ is a result of the mode-coupling term, $Z(\mathrm{k}, \tau)$, in the former, which is the distinguishing feature between the two equations.

Mode-coupling affects the rate at which the solutions to the Akcasu equation grow and/or decay: in equation 4.27, the product $r(\mathrm{k})[1 + Z(\mathrm{k}, \tau)]$ can be thought of as a modified amplification factor. Figure 4.3 compares the time evolution of the modified amplification factors associated with the different solutions in figure 4.2. There is only a short period for which the different amplification curves do not overlap. This suggests there is only a short period for which mode-coupling has an appreciable effect on the dynamics predicted by the Akcasu equation. The idea that mode-coupling becomes less appreciable during dissolution is consistent with the fact that dissolution causes the magnitudes of the composition fluctuations to decrease. As can be verified using figure 4.2, the effect of mode-coupling is to enhance the decay rate of the solutions to the Akcasu equation, and, up to $\alpha = 1$, the decay rate increases with α. The latter of these findings suggests that, during the period that mode-coupling is appreciable, only the coupling between modes with $0 < \mathrm{k} < \mathrm{k}_c$ ($\mathrm{k}_c = 3$) affects the decay rate.

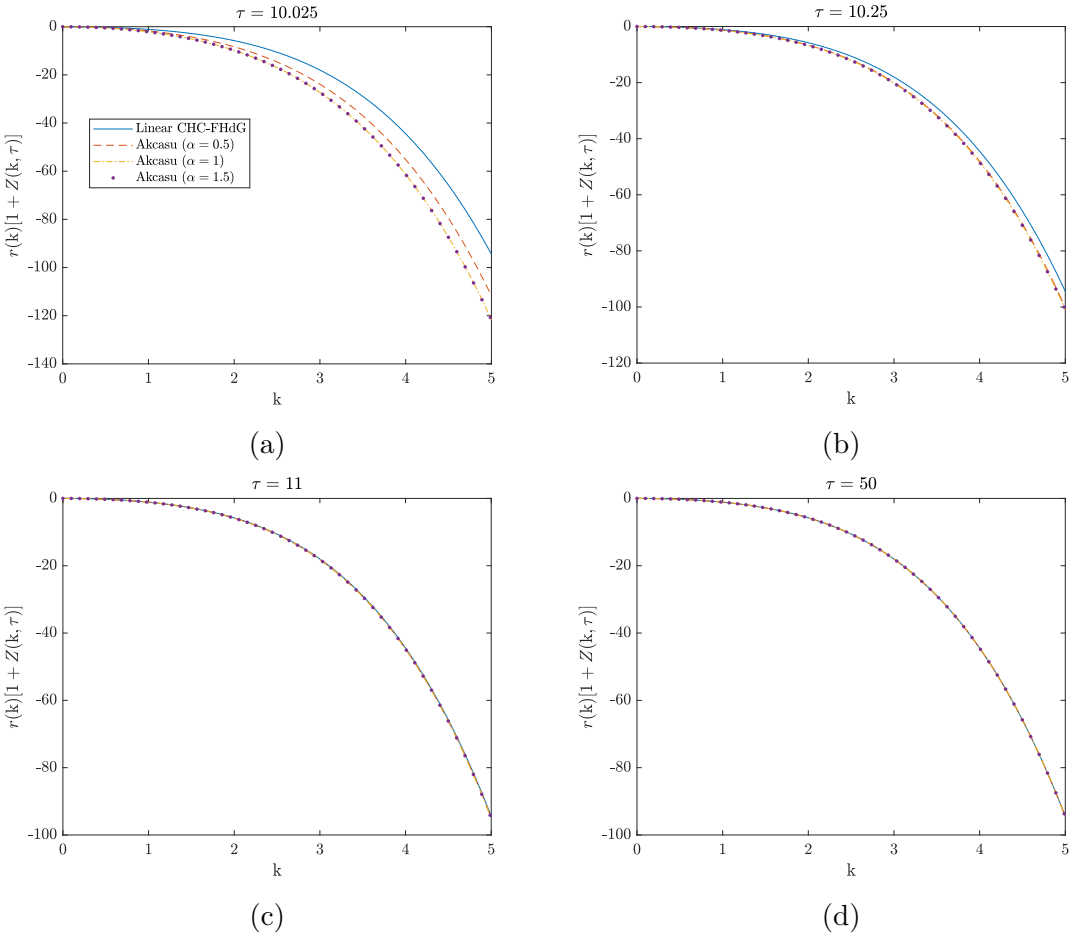

Figure 4.3: A comparison between the amplification factors associated with the different solutions in figure 4.2 at various values of τ.

Turning our attention back to figure 4.2, we can see that, around $\tau = 12$, the three solutions to the Akcasu equation coincide. Later on, around $\tau = 18$, these solutions coincide with the solution to the linear CHC-FHdG equation. We think the most probable explanation for this phenomenon is that the noise term, $C(\mathrm{k})$, begins to dominate the dynamics predicted by the Akcasu equation. Consider the equation that results from substituting equation 4.14 into equation 4.13. As the first term on the right-hand side approaches the second term on the right-hand side, the rate of change of the solution will decrease. Based on the data in figures 4.2 and 4.3, we propose that this will happen earlier for larger values of α, allowing the curves corresponding to the other solutions to 'catch up'. In this context, we can think of the linear CHC-FHdG equation as the Akcasu equation in which $\alpha = 0$.

We believe the idea that the noise begins to dominate the dynamics predicted by the Akcasu equation might also explain the temporary discrepancy that develops between the peaks of the synthetic structure factor snapshots and those of the solutions to the Akcasu equation around $\tau = 12$. We are not entirely sure how we could reduce this artefact. Including more mode-coupling terms in the Akcasu equation seems unlikely to help. This would mean including more terms in the power series expansion in equation 4.1. We expect higher-order terms can be ignored as τ increases.

Both the Akcasu equation and the linear CHC-FHdG equation accurately predict the locations of the peaks of the synthetic structure factor snapshots, i.e. $\mathrm{k}_m(\tau)$. Furthermore, as expected, both the Akcasu equation and the linear CHC-FHdG equation capture the correct equilibrium behaviour.

The Akcasu equation performed much better here, when tested using synthetic structure factor snapshots, than it did when tested using experimental scattering data by Akcasu et al. [31]. Since the parameter values corresponding to the synthetic structure factor snapshots are known, this suggests that part of the reason for the experimental discrepancy could be poor estimates of the hard-to-measure thermodynamic and molecular parameters.

4.4.2 Spinodal decomposition

Under the assumption of a small temperature jump

Next, we present our findings from testing the Akcasu equation applied to spinodal decomposition under the assumption of a small temperature jump. Figure 4.4 compares synthetic structure factor snapshots from the critical shallow time series with the numerical solutions to the dimensionless Akcasu equation and the dimensionless linear CHC-FHdG equation. Three solutions to the Akcasu equation were calculated, corresponding to $\alpha = 0.5$, 1 and 1.5. These values of α relate to $\mathrm{k}_{\mathrm{cut}} = 1.5$, $\mathrm{k}_{\mathrm{cut}} = 3$ and $\mathrm{k}_{\mathrm{cut}} = 4.5$, respectively. For $\tau > 5$, the solution to the linear CHC-FHdG equation is not plotted since it grows exponentially.

During the early stage of spinodal decomposition, i.e. up to about $\tau = 0.2$, both the Akcasu equation and the linear CHC-FHdG equation describe the time evolution of the synthetic structure factor snapshots fairly accurately. As expected in this regime, the Akcasu equation reduces to the linear CHC-FHdG equation: the solutions to both equations overlap. Just after $\tau = 0.2$, the solutions to both equations start to diverge from one another, and both equations over-predict the synthetic structure factor snapshots, but, in the cases where it was solved with

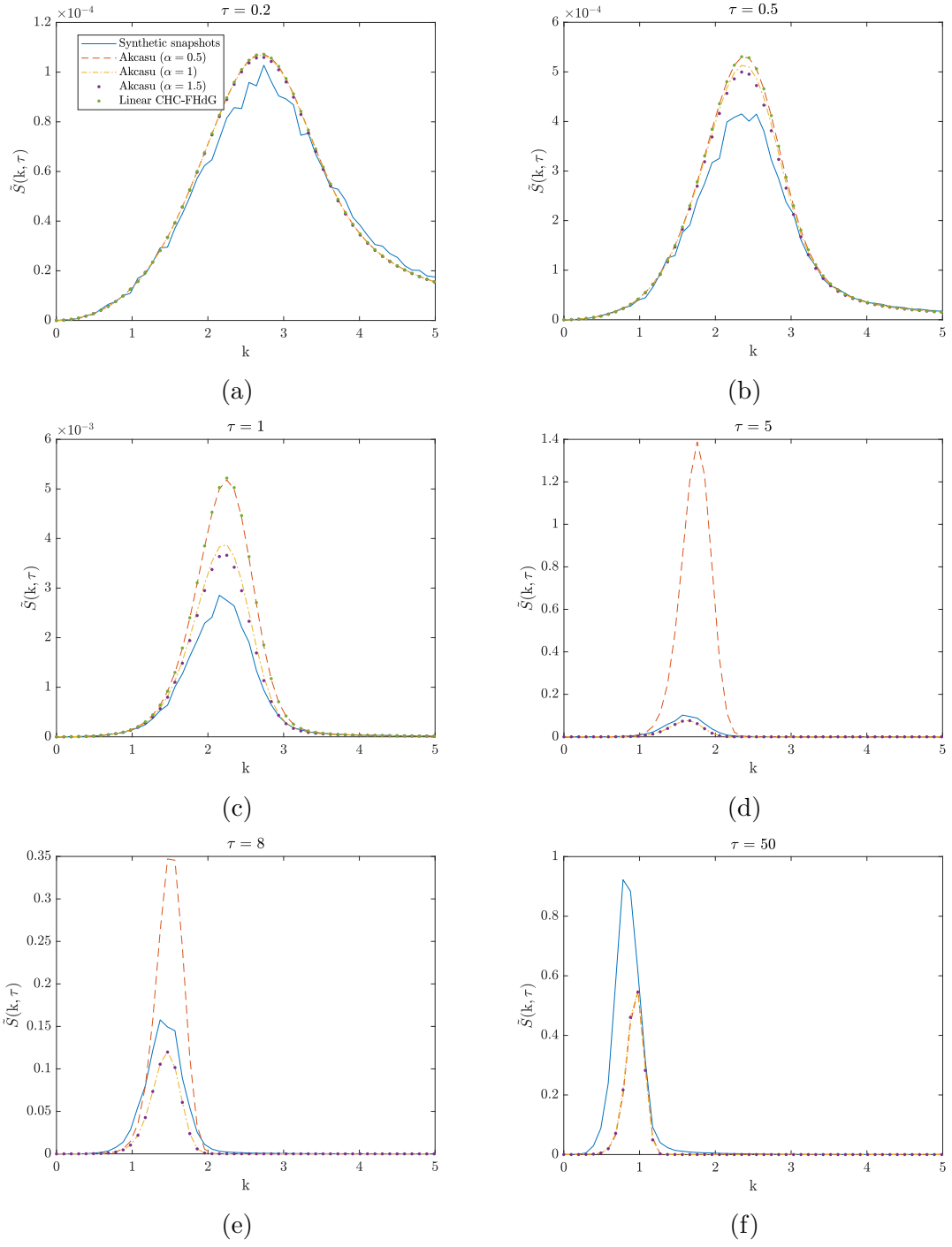

Figure 4.4: A comparison between synthetic structure factor snapshots from the critical shallow time series and the numerical solutions to the dimensionless Akcasu equation applied to spinodal decomposition under the assumption of a small temperature jump and the linear CHC-FHdG equation applied to spinodal decomposition. Three solutions to the Akcasu equation were calculated, corresponding to $\alpha = 0.5$, 1 and 1.5. These values of α relate to $k_{cut} = 1.5$, $k_{cut} = 3$ and $k_{cut} = 4.5$, respectively. For $\tau > 5$, the solution to the linear CHC-FHdG equation is not plotted since it grows exponentially.

$\alpha = 1$ and $\alpha = 1.5$, the Akcasu equation does so less dramatically. We infer that this improvement of the Akcasu equation over the linear CHC-FHdG equation is rooted in the mode-coupling term of the former. At a time $\tau > 1$, the solutions to the Akcasu equation calculated with $\alpha = 1$ and $\alpha = 1.5$ coincide and begin to underpredict the synthetic structure factor snapshots. Later on, these solutions coincide with the solution calculated with $\alpha = 0.5$. Interestingly, the curves corresponding to the $\alpha = 0.5$ solution decrease and move towards the curves corresponding to the $\alpha = 1$ and $\alpha = 1.5$ solutions. While we believe this behaviour to be unphysical, it can be explained by considering the modified amplification factor.

Figure 4.5 compares the time evolution of the modified amplification factors associated with the different solutions in figure 4.4. The x-axis is truncated at π to aid the distinguishability of the amplification curves. For a while after the onset of spinodal decomposition, the amplification curves corresponding to the $\alpha = 0.5$ solution to the Akcasu equation overlap with the amplification curves corresponding to the solution of the linear CHC-FHdG equation, i.e. $r(\mathrm{k})$. This suggests that, during this period, the coupling between modes with $0 < \mathrm{k} < 0.5\mathrm{k}_c$ ($\mathrm{k}_c = 3$) has no appreciable effect on the dynamics predicted by the Akcasu equation. Contrary to this, the amplification curves corresponding to the $\alpha = 1$ and $\alpha = 1.5$ solutions to the Akcasu equation shift below $r(\mathrm{k})$. As can be verified using figure 4.4, the effect of the mode-coupling is to slow the growth rate of the $\alpha = 1$ and $\alpha = 1.5$ solutions to the Akcasu equation. Furthermore, we note that the mode coupling enhances the decay rate of these solutions at larger k-values. Around $\tau = 5$, the amplification curve corresponding to the $\alpha = 0.5$ solution to the Akcasu equation shifts below those corresponding to the $\alpha = 1$ and $\alpha = 1.5$ solutions, with the former having a larger range of negative k-values (associated with decay). Based on equation 4.29b ($Z(\mathrm{k}, \tau)$ depends on $\tilde{S}(\mathrm{k}, \tau)$), we believe the reason for this shift is that the initial unconstrained growth of the $\alpha = 0.5$ solution to the Akcasu equation eventually leads to appreciable mode-coupling between modes with $0 < \mathrm{k} < 0.5\mathrm{k}_c$. As a result, the $\alpha = 0.5$ solution to the Akcasu equation tends towards the $\alpha = 1$ and $\alpha = 1.5$ solutions, eventually coinciding. As this happens, the amplification curve corresponding to the $\alpha = 0.5$ solution to the Akcasu equation shifts towards and eventually coincides with the amplification curves corresponding to the $\alpha = 1$ and $\alpha = 1.5$ solutions.

The fact that the different solutions to the Akcasu equation end up coinciding (as do the corresponding amplification curves) implies that the range of k-values for which the effects of mode-coupling are appreciable on the dynamics predicted by the Akcasu equation shifts to $0 < \mathrm{k} < 0.5\mathrm{k}_c$. This is consistent with coarsening, which causes $k_m(\tau)$ to shift to smaller values. Indeed, the Akcasu equation captures this effect of coarsening fairly accurately - a well-known pitfall of the linear CHC-FHdG equation.

Unlike in the case of dissolution, the noise term does not begin to dominate the dynamics of the solutions to the Akcasu equation as τ increases. Instead, the solutions to the Akcasu equation continue to grow, albeit at a slower rate than the synthetic structure factor snapshots. We believe this slower growth rate to be a consequence of mode-coupling. It seems that the approximation $C(\mathrm{k}, \chi_f) \approx C(\mathrm{k}, \chi_i)$ under the assumption of a small temperature jump does not apply to the critical shallow time series.

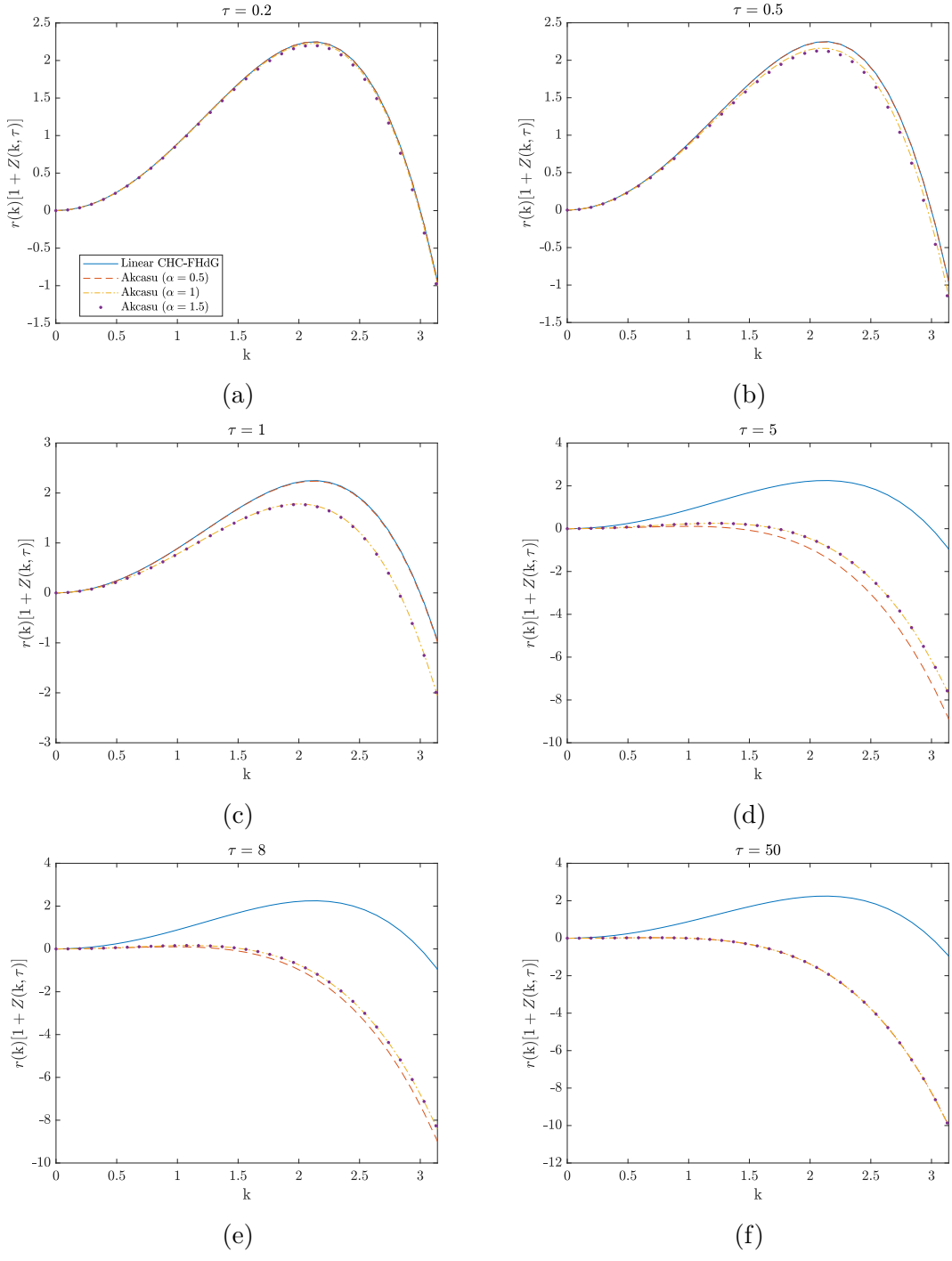

Figure 4.5: A comparison between the amplification factors associated with the different solutions in figure 4.4 at various values of τ. The x-axis is truncated at π to aid the distinguishability of the amplification curves.

Relaxing the assumption of a small temperature jump

Finally, we present our findings from testing the Akcasu equation applied to general spinodal decomposition. Figure 4.6 compares synthetic structure factor snapshots from the critical shallow time series with the numerical solutions to the non-linear and linear versions of the dimensionless Akcasu equation. Only one solution to the non-linear equation was calculated, corresponding to $\alpha = 1$. This value of α relates to $k_{cut} = 3$.

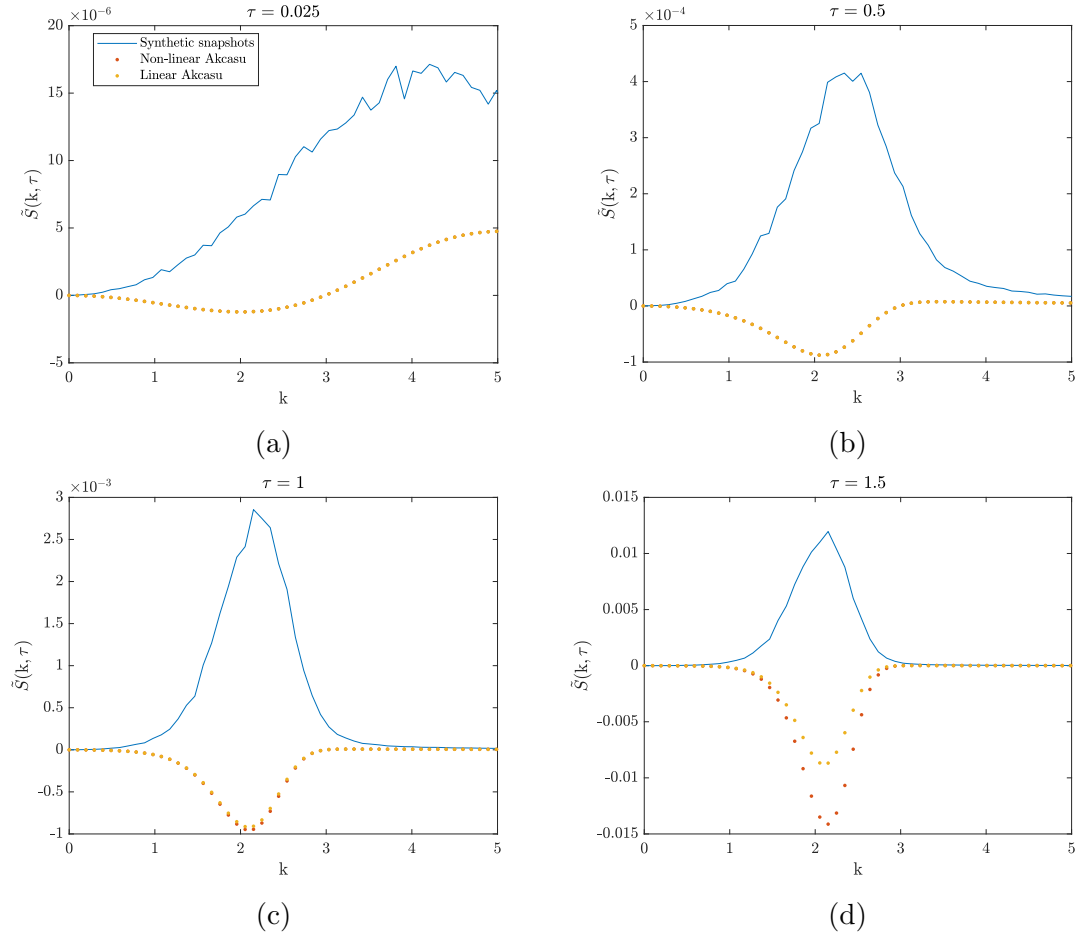

Figure 4.6: A comparison between synthetic structure factor snapshots from the critical shallow time series and the numerical solutions to the linear and non-linear versions of the dimensionless Akcasu equation applied to general spinodal decomposition. A single solution to the non-linear Akcasu equation was calculated, corresponding to $\alpha = 1$. This value of α relates to $k_{cut} = 3$.

Clearly, both the non-linear and linear versions of the Akcasu equation completely fail to describe the time evolution of the synthetic structure factor snapshots. There is no overlap between the synthetic structure factor snapshots and the solutions to the non-linear and linear Akcasu equations. Moreover, the solutions to the non-linear and linear Akcasu equations both contain negative values, which is unphysical. We believe the source of the problem must lie in the noise terms of the respective equations. This is because both equations fail in a similar fashion, which suggests the source of the problem does not lie in the mode-coupling term of the non-linear equation, or at least it does not lie solely with the mode-coupling

term. Figure 4.7 compares the noise terms in the non-linear and linear equations. The noise terms are more or less identical, which implies that $Z_{\text{eq}}(\text{k}) \approx 0$ in the non-linear equation. This is consistent with the assumed equilibrium state consisting of two stable coexisting phases. More significantly, the noise terms are negative at k-values in the approximate range $0 < \text{k} < 3$. Therefore, we believe that when we solve the non-linear and linear equations, the negative values in the noise term cause the solutions to the equations to be negative at the corresponding k-values.

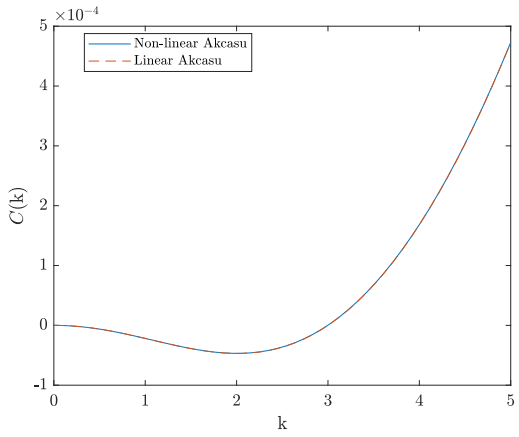

Figure 4.7: A comparison between the noise terms in the linear and non-linear versions of the dimensionless Akcasu equation applied to general spinodal decomposition.

We hypothesise that the noise term might need to be time-dependent for the Akcasu equation applied to general spinodal decomposition to accurately describe the time evolution of the synthetic structure factor snapshots. Initially, the noise term should be $C(\text{k}) = \frac{v_0|\chi-\chi_s|\frac{1}{2}\text{k}^2}{\sigma^3}$ such that the linear Akcasu equation coincides with the linear CHC-FHdG equation, which we know describes the early stage of spinodal decomposition fairly accurately. In the $t \to \infty$ limit, we believe the noise term should tend towards equation 4.30c for the reasons outlined in section 4.2.3.

4.5 Summary

We tested the Akcasu equation applied to dissolution and spinodal decomposition using synthetic structure factor snapshots and the linear CHC-FHdG equation. Based on different assumptions, we defined two versions of the Akcasu equation applied to spinodal decomposition: the Akcasu equation applied to spinodal decomposition under the assumption of a small temperature jump and the Akcasu equation applied to general spinodal decomposition. In the case of dissolution, the synthetic structure factor snapshots came from the dissolution time series. In the case of spinodal decomposition, they came from the critical shallow time series.

For the most part, the Akcasu equation applied to dissolution accurately described the dynamics of the synthetic structure factor snapshots, outperforming the linear CHC-FHdG equation. The increased accuracy of the Akcasu equation over the linear CHC-FHdG equation can be traced back to the mode-coupling term in the former. We hope these findings motivate further testing of the Akcasu equation

applied to dissolution using experimental data. Contrasting our results, obtained using synthetic structure factor snapshots, with those of Akcasu et al. [31], obtained using experimental scattering data, we note that a pre-requisite of any test using experimental data will be the ability to accurately determine the molecular and thermodynamic parameters contained in the equation.

While the Akcasu equation applied to spinodal decomposition under the assumption of a small temperature jump did not accurately describe the dynamics of the synthetic structure factor snapshots, it did capture some important qualitative features. For example, the decrease in the growth rate of the synthetic structure factor snapshots after the early stage and coarsening. The ability of the Akcasu equation to capture these features can be traced back to the mode-coupling term. In contrast to the Akcasu equation, the linear CHC-FHdG equation predicts the structure factor to grow exponentially and does not predict coarsening.

The Akcasu equation applied to general spinodal decomposition completely failed to describe the dynamics of the synthetic structure factor snapshots. We believe the problem with the equation lies with the noise term. For the Akcasu equation applied to general spinodal decomposition to accurately describe the time evolution of the structure factor, we hypothesise that the noise term might need to be time-dependent, shifting between two limiting values. We hope our findings from testing the Akcasu equation applied to spinodal decomposition motivate further theoretical work aimed towards the development of an approximate equation of motion for the structure factor during spinodal decomposition. As far as we know, these are the first reported findings for testing the Akcasu equation applied to spinodal decomposition.

Chapter 5

Modelling the time evolution of the structure factor during polymeric spinodal decomposition using dynamic mode decomposition

5.1 Introduction

In the previous chapter, we showed that one cannot use the Akcasu equation to accurately model the time evolution of the structure factor during polymeric spinodal decomposition. Coupled with the fact that the full equation of motion for the structure factor is unclosed, this illustrates that the time evolution of the structure factor is difficult to model using traditional, theory-driven modelling. In contrast to this, the structure factor can be measured relatively easily using small-angle scattering. Embracing this duality, we propose the application of system identification techniques to the problem of modelling the time evolution of the structure factor during spinodal decomposition.

In this chapter, we investigate the use of dynamic mode decomposition (DMD) to predict future snapshots of the structure factor during spinodal decomposition based on the knowledge of previous snapshots. Using synthetic structure factor snapshots from both the critical shallow and off-critical deep time series, we assess the accuracy and range of the predictions obtained using DMD, and we investigate the hyperparameter choices required to construct good models.

5.2 Methodology

Two features of DMD that appealed to us are its simple formulation in terms of a best-fit linear model and its computational efficiency. We believe these features make it a good choice of technique to benchmark other, more complex techniques against. In addition to these features, the fact that no knowledge of governing equations or system parameters is required suggests that DMD has the potential to work well in a control system. Indeed, among the many extensions of the DMD algorithm is

dynamic mode decomposition with control (DMDc) [70], which can disambiguate between the natural and forced components of the dynamics in an actuated system. Another extension of interest is bagging, optimised DMD (BOP-DMD) [71], which overcomes two key weaknesses of DMD: sensitivity to measurement noise and a lack of uncertainty quantification. Measurement noise has been shown to cause DMD to calculate a spurious eigendecomposition of $\mathbf{A}$ (defined in equation 2.141) [33, 66, 71, 72]. The synthetic structure factor snapshots used in this thesis are free of measurement noise, but this is unlikely to be the case for experimental data.

Another pertinent limitation of DMD is its inability to handle translations and scaling [33, 66]. It is well known that snapshots of the structure factor measured during spinodal decomposition translate and grow, while also changing shape, as the phase-separated microstructure coarsens [15, 44, 102]. It might then seem ill-judged to use DMD to model the time evolution of the structure factor. However, our rationale for doing so is that the slow dynamics of polymeric spinodal decomposition might lead to the localised decoupling of time and space, potentially opening the door for DMD to be applied recursively to make predictions of the structure factor at different points in time.

Using synthetic structure factor snapshots from both the critical shallow and off-critical deep time series, we trained and tested two batches of 50 DMD models - one to predict the snapshot of the synthetic structure factor at each integer value of τ in the range $1 \leq \tau \leq 50$. We implemented the training and testing of the DMD models using MATLAB code adapted from [66]. The performance of DMD depends on the careful selection of several hyperparameters [33, 66]: the number of snapshots, m; the (dimensionless) time between the snapshots, $\Delta\tau$; the rank of the reduced SVD, $\tilde{r}$; and the predictive horizon, τ_{ph}. Based on trial and error, we used $m = 10$, $\Delta\tau = 0.025$, $\tilde{r} = 3$ and $\tau_{\mathrm{ph}} = 0.75$ to obtain the majority of our results. We also present results obtained using different values of τ_{ph}. We chose $\tilde{r} = 3$ since this value seemed to be the most consistent for accurately predicting the time evolution of the synthetic structure factor snapshots. To put the listed hyperparameter values into context, the DMD models were trained on ten uniformly synthetic structure factor snapshots in the range $\tau - 1 < \tau' \leq \tau - 0.750$, and the predictions they made extended beyond the last training snapshot by three times the length of the training range. For example, the model that predicted the snapshot of the synthetic structure factor at $\tau = 9$ was trained on the snapshots at $\tau = 8.025,\ 8.050, ...,$ and 8.250.

To quantify how well the DMD models were able to predict the synthetic structure factor snapshots, the percentage errors associated with each prediction were calculated as a function of the wavenumber using

$$PE(k, \tau) = \frac{|\tilde{S}(\mathrm{k}, \tau) - \tilde{S}_{DMD}(\mathrm{k}, \tau)|}{\tilde{S}(\mathrm{k}, \tau)} \times 100, \tag{5.1}$$

where $\tilde{S}(\mathrm{k}, \tau)$ is the value of the synthetic structure factor snapshot to be predicted and $\tilde{S}_{DMD}(\mathrm{k}, \tau)$ is the prediction of the corresponding DMD model. To analyse the errors, box plots describing the summary statistics of $PE(\mathrm{k}, \tau)$ at different values of τ were plotted and compared.

In section 3.5, we argued that the small-k limit in the case of the critical shallow time series corresponds to $\mathrm{k} < 5$, while in the case of the off-critical deep time series, it corresponds to $\mathrm{k} < \pi$. For simplicity, we used the latter limit when working with

both time series. This corresponds to only using the first 33 k-values associated with each synthetic structure factor snapshot in the time series.

Compared to fields such as fluid dynamics [33,66], the synthetic structure factor snapshots we used to obtain the results in this thesis are not high-dimensional. Given the small-k limit and the size of Δx required to perform accurate and discretisation-independent simulations, it is hard to generate high-dimensional synthetic structure factor snapshots using the method outlined in section 3.2. Nevertheless, we were motivated to apply DMD because of the increased likelihood of our findings generalising to higher-dimensional snapshots compared with simply applying linear regression. Furthermore, successfully demonstrating DMD might open the door to applying extensions of the algorithm, which could shift the focus of research towards working with experimental data and perhaps even the control of phase separation.

5.3 Results and discussion

We now present our results from using DMD to model the time evolution of the synthetic structure factor snapshots from the critical shallow and off-critical deep time series. We obtained similar results using the two time series. In light of this, we only present the results corresponding to the critical shallow time series in this chapter. The results corresponding to the off-critical deep time series can be found in appendix B.

Figure 5.1 compares synthetic structure factor snapshots from the critical shallow time series with those predicted by DMD models for values of τ in the range $1 \leq \tau \leq 10$. The hyperparameters used in the DMD models are listed in section 5.2. We opted not to use a log scale on the y-axis since this makes the curves less distinguishable. However, without a log-scale on the y-axis, it is hard to see how good the predictions are at k-values where the values of the synthetic structure factor snapshots are small. Therefore, the same comparison is presented with a log-scale (base 10) on the y-axis in figure B.1. For $\tau \leq 3$, there is a low level of agreement between the synthetic structure factor snapshots and those predicted by the DMD models. The level of agreement improves for $4 \leq \tau \leq 10$. These observations are confirmed by figure 5.2, which shows a box plot of the percentage errors associated with the predictions of each DMD model. The solid blue line shows the time evolution of the mean percentage error, which starts off high for $\tau \leq 3$ but decreases over $4 \leq \tau \leq 10$, eventually reaching a plateau around $3 - 5\%$.

Another comparison between synthetic structure factor snapshots from the critical shallow time series and those predicted by DMD models is shown in figure 5.3, this time for values of τ in the range $10 \leq \tau \leq 50$. Again, the hyperparameters used in the DMD models are listed in section 5.2. The same comparison is presented with a log-scale (base 10) on the y-axis in figure B.2. For all values of τ, there is a high level of agreement between the synthetic structure factor snapshots and those predicted by the DMD models. This is confirmed by figure 5.4, which shows a box plot of the percentage errors associated with the predictions of each DMD model. The mean percentage error line is more or less flat, fluctuating between values of $1 - 5\%$.

From figures 5.1-5.4, we infer that, with the exception of $\tau < 3$, DMD can be used to accurately model the time evolution of the synthetic structure factor snapshots.

To investigate whether more accurate predictions of the synthetic structure factor

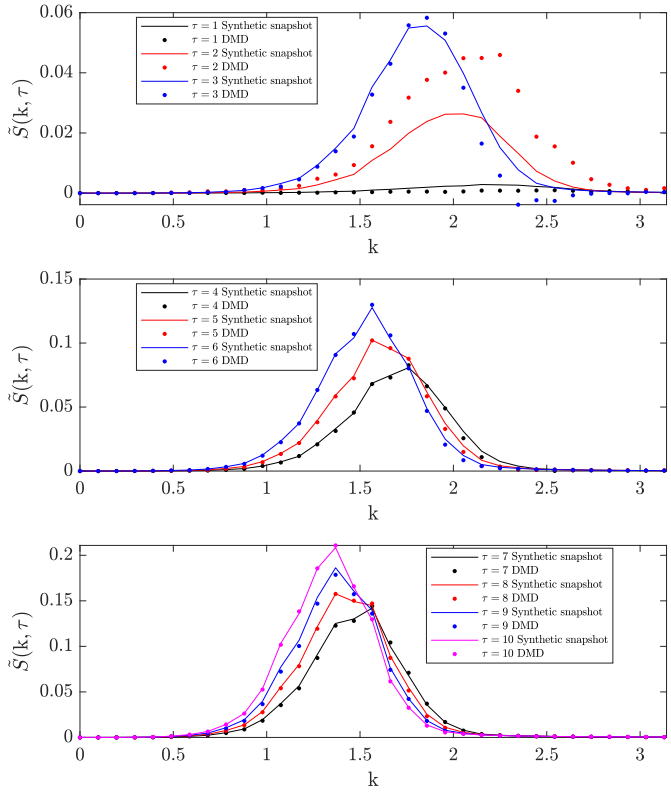

Figure 5.1: A comparison between synthetic structure factor snapshots from the critical shallow time series and those predicted by DMD models for values of τ in the range $1 \leq \tau \leq 10$. The hyperparameters used in the DMD models are listed in section 5.2.

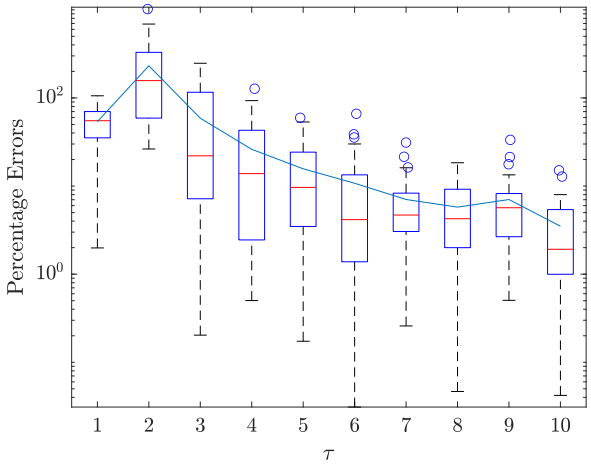

Figure 5.2: Box plots of the percentage errors associated with the predictions of each DMD model in figure 5.1. In each box plot, the red line shows the median, the blue box outlines the interquartile range, the black dotted lines extend beyond the box by 1.5 times the interquartile range, and the blue circles denote outliers. The solid blue line shows the time evolution of the mean.

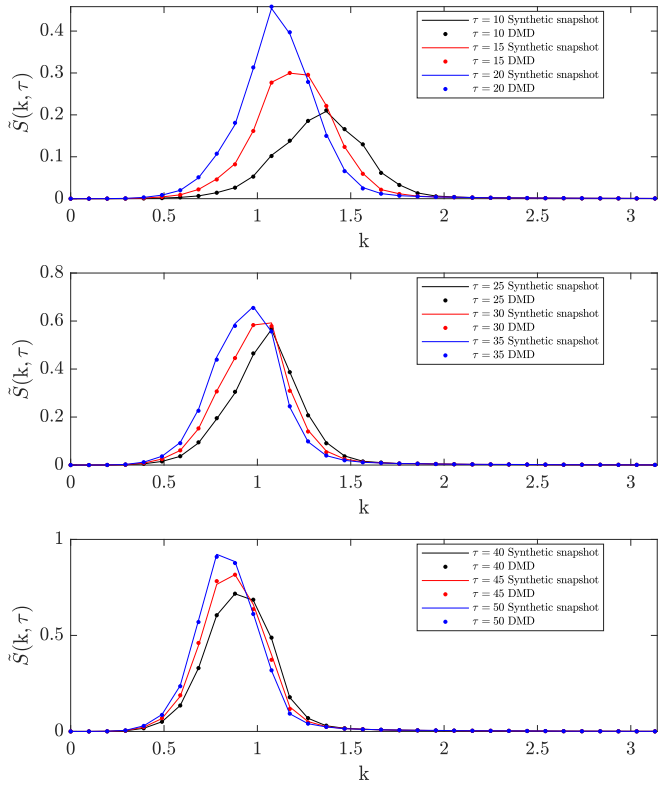

Figure 5.3: A comparison between synthetic structure factor snapshots from the critical shallow time series and those predicted by DMD models for values of τ in the range $10 \leq \tau \leq 50$. The hyperparameters used in the DMD models are listed in section 5.2.

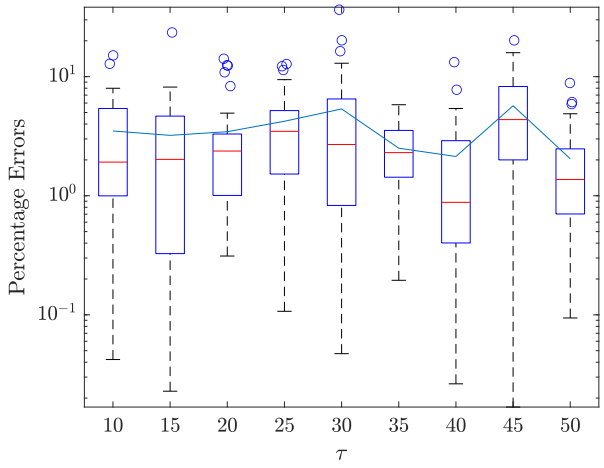

Figure 5.4: Box plots of the percentage errors associated with the predictions of each DMD model in figure 5.3. In each box plot, the red line shows the median, the blue box outlines the interquartile range, the black dotted lines extend beyond the box by 1.5 times the interquartile range, and the blue circles denote outliers. The solid blue line shows the time evolution of the mean.

snapshots could be made for $\tau \leq 3$, we tested the predictions of several DMD models with values of $\tau_{\text{ph}} < 0.75$ at $\tau = 1$ and $\tau = 3$. Figure 5.5 compares the predictions of these models with the corresponding synthetic structure factor snapshots. The figure reveals that the level of agreement between the synthetic structure factor snapshots and those predicted by the DMD models increases as the value of τ_{ph} decreases. A greater reduction in the value of τ_{ph} is required at $\tau = 1$ than at $\tau = 3$ to achieve this effect. These findings suggest that there is a trade-off between the accuracy and extrapolation of the DMD predictions. Furthermore, the trade-off seems to be coupled to the value of τ for which a prediction is made: to make accurate predictions at smaller values of τ, one is constrained by having to use a smaller value of τ_{ph}.

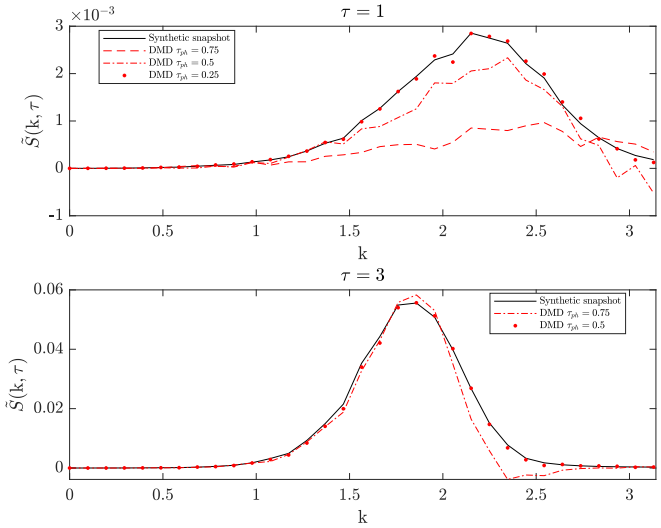

Figure 5.5: A comparison between synthetic structure factor snapshots from the critical shallow time series and those predicted by DMD models with values of $\tau_{\text{ph}} < 0.75$ at $\tau = 1$ (top panel) and $\tau = 3$ (bottom panel). The values of the other hyperparameters used in the DMD models are the same as those listed in section 5.2.

To test whether the trade-off between the accuracy and extrapolation of the DMD predictions is indeed time-dependent, we tested the predictions of DMD models with values of $\tau_{\text{ph}} > 0.75$ at $\tau = 20, 30, 40$ and 50. We used increasingly large values of τ_{ph} to predict the synthetic structure factor snapshots corresponding to increasingly large values of τ. Figure 5.6 compares the predictions of these models with the corresponding synthetic structure factor snapshots. The figure reveals that there is a high level of agreement between the synthetic structure factor snapshots and those predicted by the DMD models. This is confirmed by figure 5.7, which shows a box plot of the percentage errors associated with the predictions of each DMD model. The percentage errors in figure 5.7 are comparable with those in figure 5.4. The results in figures 5.6 and 5.7 verify that the trade-off between the accuracy and extrapolation is time dependent. Specifically, the trade-off is more important early on and becomes less important as τ increases. In other words, as τ increases, one can maintain a certain level of accuracy while predicting further into the future.

The time-dependent accuracy-extrapolation trade-off can be linked to the growth rate of the structure factor during spinodal decomposition, which is a diffusion-like

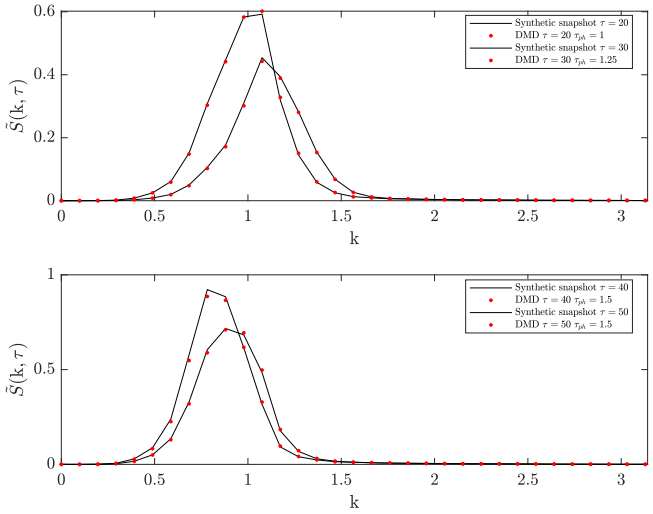

Figure 5.6: A comparison between synthetic structure factor snapshots from the critical shallow time series and those predicted by DMD models with values of $\tau_{\text{ph}} > 0.75$ at $\tau = 20$ and 30 (top panel) and $\tau = 40$ and 50 (bottom panel). The values of the other hyperparameters used in the DMD models are the same as those listed in section 5.2.

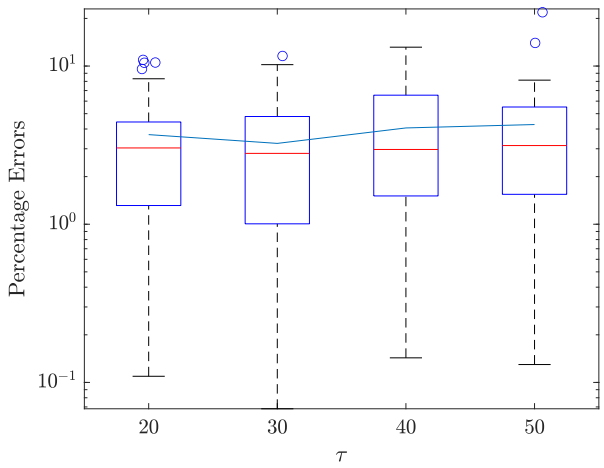

Figure 5.7: Box plots of the percentage errors associated with the predictions of each DMD model in figure 5.6. In each box plot, the red line shows the median, the blue box outlines the interquartile range, the black dotted lines extend beyond the box by 1.5 times the interquartile range, and the blue circles denote outliers. The solid blue line shows the time evolution of the mean.

process. Early on in the process, the growth rate of the structure factor is rapid (indeed, it is exponential for a short period at the start). As time goes on, the growth rate decreases. To capture the rapid early growth of the structure factor, the eigenvalues of $\mathbf{A}$ must be highly unstable, which means the resulting DMD models are only suitable for very short-term predictions. This is exemplified in figure 5.8, which compares the eigenvalues of the DMD models used to make the predictions of the synthetic structure factor snapshots at $\tau = 3$ and $\tau = 10$ in figure 5.1. The

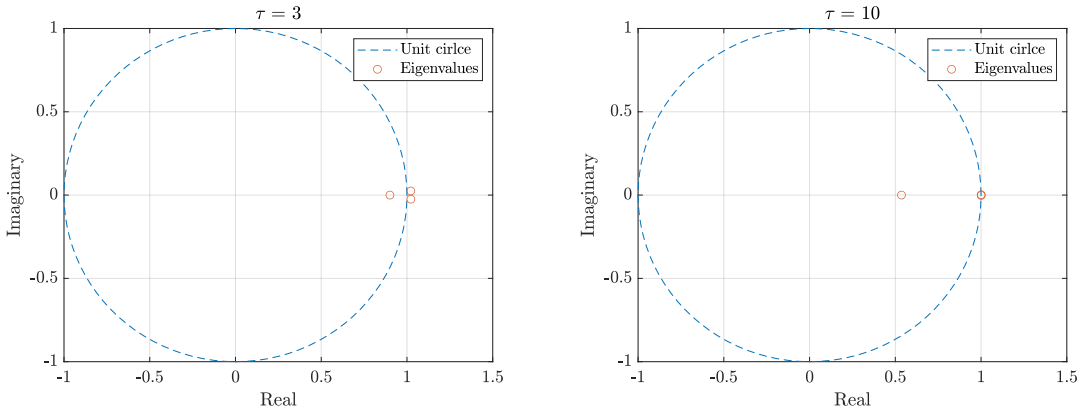

(a) (b)

Figure 5.8: The eigenvalues of the DMD models used to make the predictions of the synthetic structure factor snapshots at (a) $\tau = 3$ and (b) $\tau = 10$ in figure 5.1.

model corresponding to $\tau = 3$ has eigenvalues that extend beyond the unit circle further than those belonging to the model corresponding to $\tau = 10$. This indicates that they are more unstable.

As mentioned in section 5.2, DMD models with $\tilde{r} = 3$ seemed to be the most consistent at accurately predicting the time evolution of the synthetic structure factor snapshots. We believe that the DMD models with $\tilde{r} < 3$ often did not capture enough of the dynamics, while models with $\tilde{r} > 3$ had an increased likelihood of containing unstable eigenvalues.

The practicality of DMD in an experimental setting depends on how the dimensionless time used to demonstrate the technique scales to physical time. Using equations 3.4b and 2.64, one can estimate a range of values of the mutual diffusion coefficient, D, for which the technique is likely to work well. Using equation 3.4b, it can be seen that for one dimensionless time unit to correspond to more than one second, $M < \frac{v_0\sigma^2}{2k_BT(\chi-\chi_s)^2}$. Substituting this inequality into equation 2.64, one obtains $|D| < \frac{\sigma^2}{(\chi-\chi_s)}$. In the case of the critical shallow time series, $\sigma = 20^{\frac{1}{2}} v_0^{\frac{1}{3}}$ and $(\chi - \chi_s) \approx 2 \times 10^{-5}$. A typical value of v_0 is 10^{-28} m^3 [2, 31]. Substituting these values of σ, $(\chi - \chi_s)$ and v_0 into the inequality for $|D|$ yields $|D| < 10^{-13}$ $m^2 s^{-1}$. For a meaningful comparison between this value and an experimental value of the mutual diffusion coefficient to be made, the experimental blend should be analogous to the synthetic blend. Specifically, the Kuhn lengths, degrees of polymerisation, average volume fraction and quench depth $(\chi - \chi_s)$ associated with the experimental blend should be similar to the synthetic blend. We searched the literature to find a suitable blend to compare with but did not find anything satisfactory. For the time being, we used the representative data in [2] to calculate the following 'experimental' value of the diffusion coefficient: $|D_{\text{exp}|} \approx 10^{-16}$ $m^2 s^{-1}$. This compares favourably with $|D| < 10^{-13}$ $m^2 s^{-1}$, which is an encouraging sign.

Given the results above, we propose combining DMD with the technique we presented in [57] to predict the future characteristics of phase-separated microstructures as they evolve. DMD lends itself to real-time usage due to its low computational cost. Real-time predictions of the structure factor and microstructure characteristics during spinodal decomposition could be useful in a control system, affecting

the quench depth based on microstructure requirements, for example, thus opening the door to the control of phase separation as a means of tailoring and tuning the microstructures of materials derived from polymer blends.

5.4 Summary

Using DMD models constructed from batches of synthetic structure factor snapshots from the critical shallow and off-critical deep time series, we modelled the time evolution of the structure factor in two simulated polymer blends undergoing spinodal decomposition. Apart from early on in the process ($\tau < 3$), the DMD models were able to make accurate future predictions of the synthetic structure factor snapshots that extended beyond the last training snapshot by three times the length of the training range. We identified a trade-off between the accuracy and extrapolation of the DMD predictions. The trade-off was coupled to the value of τ for which the prediction was made, i.e. the trade-off was more important early on, decreasing in importance as τ increased. Using smaller values of τ_{ph} to make predictions of the synthetic structure factor snapshots at $\tau = 1$ and $\tau = 3$, we showed that one could improve the accuracy of the predictions at these times. We also showed that one could maintain the accuracy of predictions made at later times, specifically at $\tau = 20$, 30, 40 and 50, while increasing the value of τ_{ph}. We sought to explain the accuracy-extrapolation trade-off by making a connection with the diffusion-like nature of spinodal decomposition and the eigenvalues required by the DMD models to capture the dynamics of the synthetic structure factor snapshots. The practicality of DMD in an experimental setting will likely depend on the mutual diffusion coefficient of the blend in question.

We believe our results are promising for the development of an experimental technique to predict structure factor snapshots and microstructure characteristics corresponding to materials derived from the phase separation of polymer blends in real time. Such predictions could be useful in a control system. Of course, this will hinge on being able to replicate our results using experimental data. A limitation of our investigation is that we used idealised synthetic structure factor snapshots. To address this, a logical next step should be to demonstrate whether our findings can be replicated with more realistic synthetic structure factor snapshots, which, for example, could be corrupt with external noise, have missing values or be sampled irregularly. There is an extension to DMD for dealing with noise, BOP-DMD, which might be appropriate to consider. BOP-DMD also offers the ability to quantify the uncertainty in the predictions, which could make DMD more practical to use in an experimental setting. It would also be interesting to work with data from multi-step spinodal decomposition [9, 101, 103]. Multi-step spinodal decomposition would mimic a process in which the temperature is changed by a control system in response to predictions of the structure factor and microstructure characteristics. One might also consider investigating the application of DMDc to such a system, i.e. one with actuation. Finally, since DMD is equation-free and linear, it would be interesting to apply algorithms that offer the opportunity to learn a non-linear equation of motion for the structure factor during spinodal decomposition. We have made some progress in this direction. This is the focus of the next chapter.

Chapter 6

Towards modelling the time evolution of the structure factor during polymeric spinodal decomposition using parsimonious non-linear system identification techniques

6.1 Introduction

In the previous chapter, we showed that DMD can be applied recursively to accurately model the time evolution of the structure factor during polymeric spinodal decomposition. A natural way to build on this work would be to investigate the application of parsimonious non-linear system identification techniques. In this chapter, we investigate the application of parametric PDE-FIND and SINDy combined with the SVD. The relevant sections for each investigation feature tailored introductions, so we will not go into any more details here. The work in this chapter is focussed on building foundations and we hope it will provide a solid starting point for future research.

6.2 Parametric PDE-FIND

6.2.1 Introduction

At first glance, parametric PDE-FIND [83] might seem to be a promising technique for modelling the time evolution of the structure factor during polymeric spinodal decomposition. However, after some thought, two issues become apparent:

- To apply parametric PDE-FIND, the structure factor must be represented in a coordinate system that enables a sparse representation of the dynamics. This is not the case in the experimental coordinate system since the full equation of motion is unclosed.

- The Akcasu equation [19] suggests that integral basis functions are more appropriate than differential basis functions. This raises the question as to whether parametric PDE-FIND can be used to identify parametric integro-differential equations.

Naively, we began by neglecting the first issue. Instead, we set out to investigate whether parametric PDE-FIND can be used to identify parametric integro-differential equations. Our hope was that we might be able to apply the resulting modified technique to learn an accurate approximate equation of motion for the structure factor. In hindsight, we now know that learning approximate equations is outside of the scope of parametric PDE-FIND. In the case of PDE-FIND, there is evidence of spurious terms being identified when the library of candidate basis functions is incomplete [84].

6.2.2 Methodology

In theory, modifying parametric PDE-FIND to identify integro-differential equations is straightforward: one simply needs to construct the library of candidate basis functions out of integral functions instead of differential functions. The functions we considered for inclusion in the library are shown in table 6.1.

Number	Function
1	$\tilde{S}(\mathrm{k},\tau)$
2	$\tilde{S}(\mathrm{k},\tau)\int_0^{\mathrm{k_{cut}}} d\mathrm{k}'\ \mathrm{k}'^2\tilde{S}(\mathrm{k}',\tau)$
3	$\tilde{S}(\mathrm{k},\tau)\int_0^{\mathrm{k_{cut}}} d\mathrm{k}'\ \mathrm{k}'^4\tilde{S}(\mathrm{k}',\tau)$
4	1
5	$\tilde{S}(\mathrm{k},\tau)^2$
6	$(\tilde{S}(\mathrm{k},\tau)\int_0^{\mathrm{k_{cut}}} d\mathrm{k}'\ \mathrm{k}'^2\tilde{S}(\mathrm{k}',\tau))^2$
7	$(\tilde{S}(\mathrm{k},\tau)\int_0^{\mathrm{k_{cut}}} d\mathrm{k}'\ \mathrm{k}'^4\tilde{S}(\mathrm{k}',\tau))^2$
8	$\tilde{S}(\mathrm{k},\tau)^2\int_0^{\mathrm{k_{cut}}} d\mathrm{k}'\ \mathrm{k}'^2\tilde{S}(\mathrm{k}',\tau)$
9	$\tilde{S}(\mathrm{k},\tau)^2\int_0^{\mathrm{k_{cut}}} d\mathrm{k}'\ \mathrm{k}'^4\tilde{S}(\mathrm{k}',\tau)$
10	$\tilde{S}(\mathrm{k},\tau)^2\int_0^{\mathrm{k_{cut}}} d\mathrm{k}'\ \mathrm{k}'^2\tilde{S}(\mathrm{k}',\tau)\int_0^{\mathrm{k_{cut}}} d\mathrm{k}'\ \mathrm{k}'^4\tilde{S}(\mathrm{k}',\tau)$
11	$\tilde{S}(\mathrm{k},\tau)(\int_0^{\mathrm{k_{cut}}} d\mathrm{k}'\ \mathrm{k}'^2\tilde{S}(\mathrm{k}',\tau))^2$
12	$\tilde{S}(\mathrm{k},\tau)(\int_0^{\mathrm{k_{cut}}} d\mathrm{k}'\ \mathrm{k}'^4\tilde{S}(\mathrm{k}',\tau))^2$
13	$\tilde{S}(\mathrm{k},\tau)\int_0^{\mathrm{k_{cut}}} d\mathrm{k}'\ \mathrm{k}'^2\tilde{S}(\mathrm{k}',\tau)\int_0^{\mathrm{k_{cut}}} d\mathrm{k}'\ \mathrm{k}'^4\tilde{S}(\mathrm{k}',\tau)$

Table 6.1: The candidate integral basis functions we considered for inclusion in the library matrix when applying parametric PDE-FIND. Functions 1 and 4 appear in the linear CHC-FHdG equation for the structure factor during spinodal decomposition. Function 4 corresponds to the noise term. Functions 1 - 4 appear in the Akcasu equation applied to spinodal decomposition. Functions 4 - 10 are the squares and cross terms of functions 1 -3 . Functions 11 - 13 are inspired by the derivation of the Akcasu equation. Specifically, they are truncated higher-order terms.

We tested the modified technique on several tasks, each increasing in complexity:

- Identify the linear CHC-FHdG equation for the structure factor during spinodal decomposition with an exact library, i.e. a library containing only the terms that appear in the linear CHC-FHdG equation

- Identify the linear CHC-FHdG equation with an overcomplete library, i.e. a library containing the terms that appear in the linear CHC-FHdG equation and terms that do not
- Identify the Akcasu equation applied to spinodal decomposition under the assumption of a small temperature jump with an exact library
- Identify the Akcasu equation with an overcomplete library

To facilitate the above tests, we constructed a time series out of snapshots of the numerical solution to the dimensionless Akcasu equation applied to spinodal decomposition under the assumption of a small temperature jump - we refer to this time series as the equation learning (EQL) time series. We calculated the numerical solution using $N = 2700$, $\phi_0 = 0.5$, $\sigma = \sqrt{20}v_0^{\frac{1}{3}}$, $\alpha = 1$, $\chi_i = 0.000716$, $\chi_f = 0.000765$, $N_s = 257$, $m_{\max} = 400000$, $\Delta x = 0.25$ and $\Delta\tau = 0.00001$. The initial condition was the snapshot corresponding to $\tau = 6.25 \times 10^{-5}$ in the critical shallow time series, i.e. the first snapshot in the time series. The EQL time series comprises snapshots of the numerical solution corresponding to the first and every 125^{th} time step.

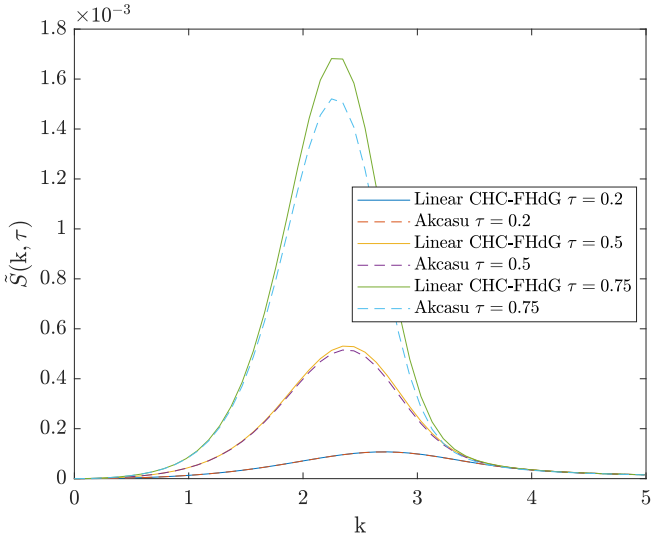

Figure 6.1: Snapshots of the numerical solution to the dimensionless linear CHC-FHdG for the structure factor during spinodal decomposition and the dimensionless Akcasu equation applied to spinodal decomposition under the assumption of a small temperature jump (EQL time series) at $\tau = 0.2, 0.5$ and 0.75. The time at which the two sets of snapshots begin to diverge corresponds to the end of the early stage of spinodal decomposition. We determined this to be around $\tau = 0.25$.

In the case of trying to identify the linear CHC-FHdG equation, we only used snapshots corresponding to the early stage of spinodal decomposition. To determine the time at which the early stage ends, we compared snapshots from the EQL time series with snapshots of the numerical solution to the dimensionless linear CHC-FHdG equation for the structure factor during spinodal decomposition. The time at which the two sets of snapshots begin to diverge corresponds to the end of the early stage. We determined this to be around $\tau = 0.25$. Figure 6.1 compares a selection

of snapshots from the EQL time series with those of the numerical solution to the linear CHC-FHdG equation.

6.2.3 Results and discussion

First, we set out to identify the linear CHC-FHdG equation for the structure factor during spinodal decomposition with an exact library. We constructed the library such that it only contained functions 1 and 4 in table 6.1. With this library, we applied parametric PDE-FIND to the first 200 snapshots in the EQL time series. Figure 6.2 compares the best predictions of the coefficients made by parametric PDE-FIND with the true values. The figure reveals an excellent match between the predicted and true values.

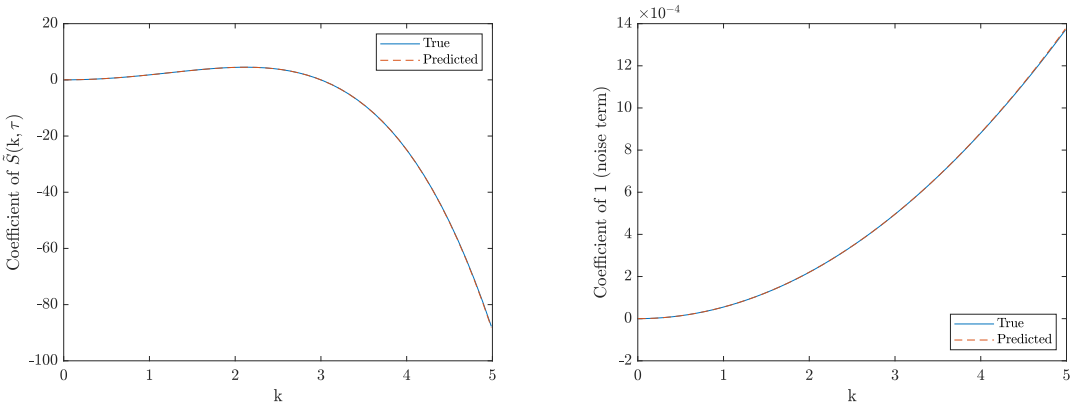

(a) (b)

Figure 6.2: A comparison between the theoretical ('true') values of the parametric coefficients in the dimensionless linear CHC-FHdG equation for the structure factor during spinodal decomposition and the best values calculated by parametric PDE-FIND ('predicted') using an exact library and the first 200 snapshots in the EQL time series. Frames (a) and (b) correspond to functions 1 and 4 in table 6.1, respectively.

Next, we set out to identify the linear CHC-FHdG equation with an overcomplete library. We constructed the library such that it contained all of the functions in table 6.1. With this library, we applied parametric PDE-FIND to the first 200 snapshots in the EQL time series. Only the correct functions were identified as having non-zero coefficients. Again, there was an excellent match between the predicted and true values of the coefficients.

Next, we set out to identify the Akcasu equation applied to spinodal decomposition under the assumption of a small temperature jump with an exact library. We constructed the library such that it contained functions 1 - 4 in table 6.1. With this library, we applied parametric PDE-FIND to all of the snapshots in the EQL time series. Figure 6.3 compares the best predictions of the coefficients made by parametric PDE-FIND with the true values. The figure reveals an excellent match between the predicted and true values.

Finally, we set out to identify the Akcasu equation with an overcomplete library. We constructed the library such that it contained all of the functions in table 6.1. With this library, we applied parametric PDE-FIND to all of the snapshots in the

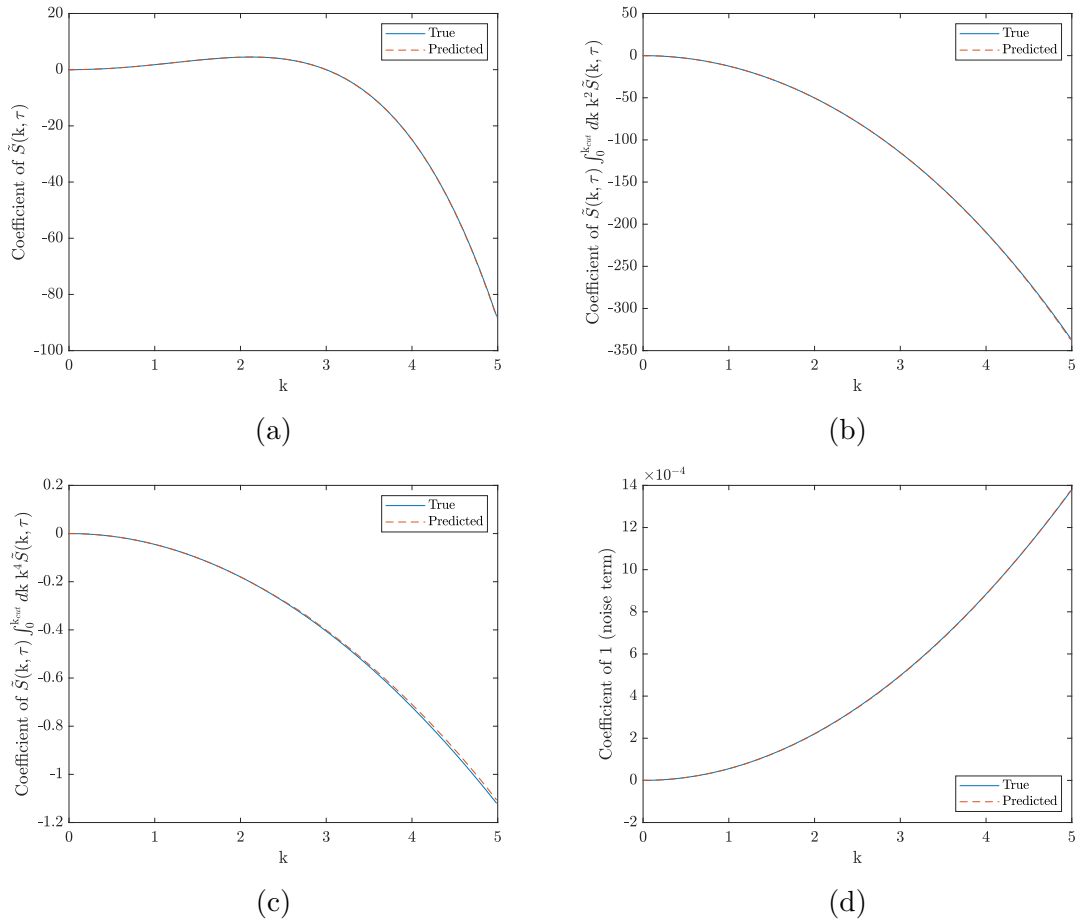

Figure 6.3: A comparison between the theoretical ('true') values of the parametric coefficients in the dimensionless Akcasu equation applied to spinodal decomposition under the assumption of a small temperature jump and the best values calculated by parametric PDE-FIND ('predicted') using an exact library and the EQL time series. Frames (a), (b), (c) and (d) correspond to functions 1,2,3 and 4 in table 6.1, respectively.

EQL time series. The correct functions were identified as having non-zero coefficients, however so were some incorrect functions, namely functions 11 - 13. This result was reproduced for a range of hyperparameter combinations. We note that the incorrectly identified functions are linearly dependent with some of the correct functions, specifically functions 1 - 3. This linear dependency makes the sparse regression problem difficult to solve accurately, likely resulting in misidentified terms.

The issue of linear dependency between functions in the library suggests that parametric PDE-FIND cannot be used to reliably and accurately identify integro-differential equations. We believe the most promising work around for this issue is transforming the time series into a coordinate system in which the dynamics are described by linearly independent basis functions. A good coordinate transformation would also enable a sparse representation of the dynamics, addressing the first issue highlighted in section 6.2.1.

6.3 SINDy combined with the SVD

6.3.1 Introduction

With regards to parsimonious non-linear system identification, coordinate transformations have the potential to kill two birds with one stone, relieving the issue of linear dependency between basis functions and enabling a sparse representation of the dynamics.

In general, the SVD is a good technique to start with when considering coordinate transformations in the context of dynamical systems [79]. As outlined in section 2.5.2, the reduced SVD allows one to approximate spatio-temporal time series in terms of a few dominant modes (patterns) whose amplitudes evolve with time. SVD modes are orthogonal and optimally tailored to the time series.

When the underlying governing equation is known (we note that this is not a requirement), one can perform a Galerkin expansion with the reduced SVD - a process in which one converts the governing equation (a non-linear PDE) into a non-linear ODE in terms of the mode amplitudes [33]. This motivates using SINDy to model the time evolution of the reduced SVD mode amplitudes in cases where the Galerkin expansion is unknown. Combining SINDy with the SVD was demonstrated in the original SINDy paper [76].

A prerequisite to using SINDy to model the time evolution of reduced SVD mode amplitudes is understanding how well the reduced SVD captures the time series under consideration. As previously discussed in section 2.5.2, SVD is known not to handle translations and scaling well. This is at odds with the fact that snapshots of the structure factor measured during spinodal decomposition are known to translate and grow, while also changing shape, as coarsening occurs. Not wanting to leave any stones unturned, we set out to investigate how well the synthetic structure factor snapshots in the critical shallow and off-critical deep time series can be reconstructed using the reduced SVD.

6.3.2 Methodology

We calculated the SVD of the critical shallow and off-critical deep time series, one time series at a time. For various ranks $\tilde{r}$, we compared reconstructions of the snapshots in each time series with the originals. We visually assessed the accuracy of the reconstructions.

To facilitate the construction of sparse SINDy models, we looked for accurate reconstructions with low ranks. As the number of modes required to accurately reconstruct the time series increases, so too does the number of variables to model with SINDy.

6.3.3 Results and discussion

First, we calculated the SVD of the critical shallow time series and investigated a five-mode reconstruction of the synthetic structure factor snapshots. Figure 6.4 compares the reconstructed snapshots with the originals at integer values of τ between 1 and 5. In the interest of orderliness, we present supplementary results in appendix B. Figures B.9a and B.9b present the same comparison at earlier and later times, respectively. We note that the snapshots in the figures are presented with a

log scale on the y-axis to make it easier to assess the accuracy of the reconstructions at k-values where the values of the synthetic structure factor snapshots are small. The figures reveal that the level of agreement between the reconstructed and original snapshots is low, although it does seem to improve for higher values of τ.

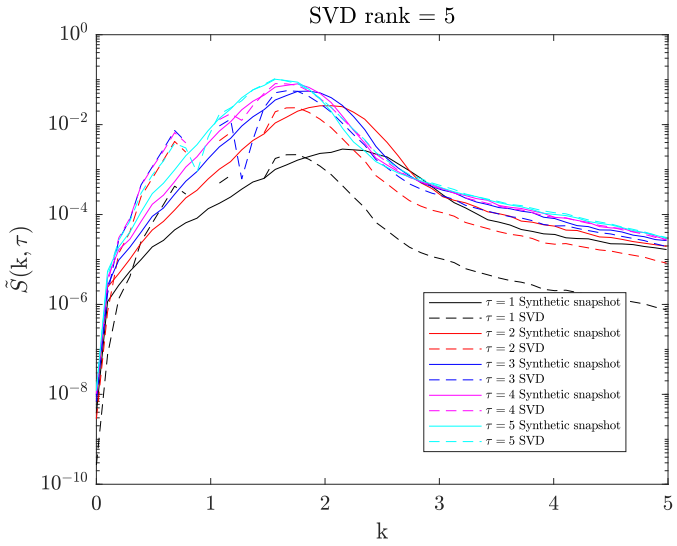

Figure 6.4: A comparison between the five-mode SVD reconstruction of synthetic structure factor snapshots from the critical shallow time series and the originals at $\tau = 1, 2, 3, 4$ and 5. The snapshots are presented with a log scale on the y-axis. Some of the reconstructed values were negative. These values are not plotted.

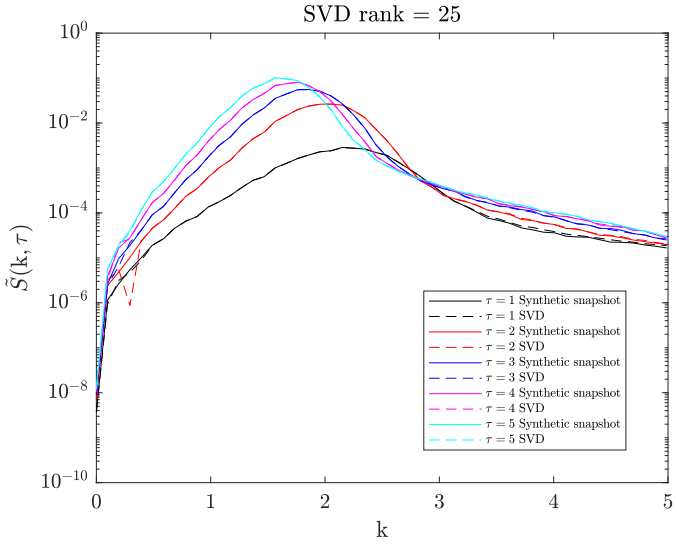

Figure 6.5: A comparison between the 25-mode SVD reconstruction of synthetic structure factor snapshots from the critical shallow time series and the originals at $\tau = 1, 2, 3, 4$ and 5. The snapshots are presented with a log scale on the y-axis. Some of the reconstructed values were negative. These values are not plotted.

Next, we investigated a 25-mode reconstruction of the synthetic structure factor snapshots in the critical shallow time series. Figure 6.5 compares the reconstructed snapshots with the originals at integer values of τ between 1 and 5. Figures B.10a

and B.10b present the same comparison at earlier and later times, respectively. Again, we note that the snapshots in the figures are presented with a log scale on the y-axis. The figures reveal a much improved level of agreement between the reconstructed and original snapshots relative to the five-mode reconstruction. This finding is an indicator of a translation and scaling-induced breakdown of the reduced SVD [33, 104].

A rudimentary fix for the scaling is to take the log of the time series before calculating the SVD. We first applied this fix to the critical shallow time series and investigated a five-mode reconstruction of the synthetic structure factor snapshots. Figure 6.6 compares the reconstructed snapshots with the originals (now the log (base 10) of the synthetic structure factor snapshots in the critical shallow time series) at integer values of τ between 1 and 5. Figures B.11a and B.11b present the same comparison at earlier and later times, respectively. The figures reveal an improved level of agreement between the reconstructed and original snapshots relative to the five-mode reconstruction where the scaling was not accounted for. These findings generalise to the off-critical deep time series. In this case, figure 6.7 compares the reconstructed snapshots with the originals (now the log (base 10) of the synthetic structure factor snapshots in the off-critical deep time series) at integer values of τ between 1 and 5. Figures B.12a and B.12b present the same comparison at earlier and later times, respectively.

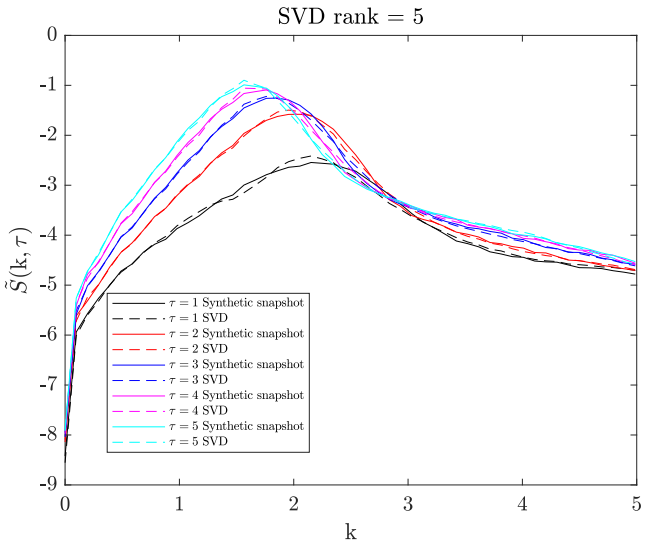

Figure 6.6: A comparison between the five-mode SVD reconstruction of the log (base 10) of synthetic structure factor snapshots from the critical shallow time series and the originals at $\tau = 1, 2, 3, 4$ and 5.

Due to time constraints, we did not attempt to construct SINDy models for the reduced SVD mode amplitudes corresponding to the log of the critical shallow and off-critical deep time series. For context, figure 6.8 shows the time evolution of the mode amplitudes corresponding to the reconstructed synthetic structure factor snapshots in figures 6.6, B.11a and B.11b. If an appropriate SINDy model can be identified, this would suggest that the reduced SVD enables a sparse representation of the dynamics. However, there is no guarantee that the SVD will enable a sparse representation of the dynamics.

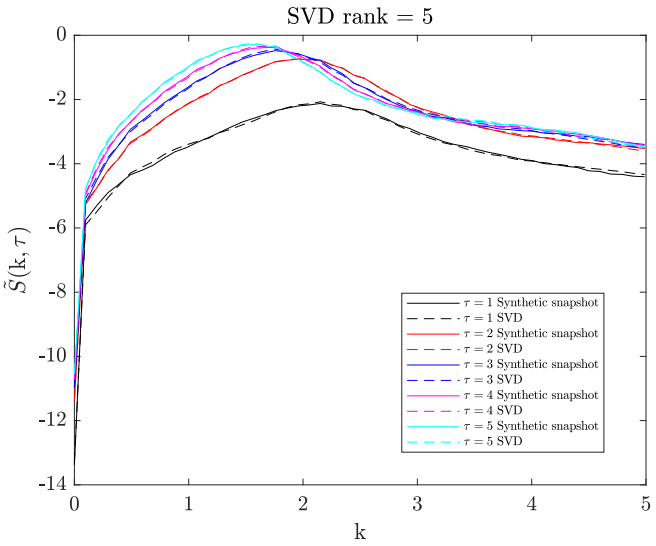

Figure 6.7: A comparison between the five-mode SVD reconstruction of the log (base 10) of synthetic structure factor snapshots from the off-critical deep time series and the originals at $\tau = 1, 2, 3, 4$ and 5.

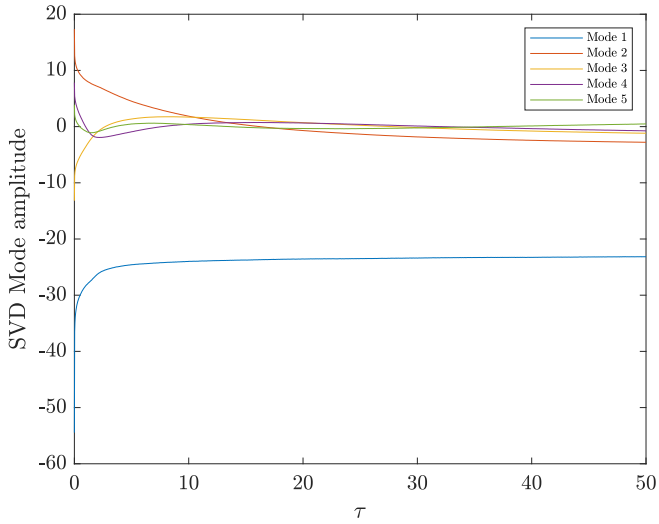

Figure 6.8: The time evolution of the mode amplitudes corresponding to the snapshots in figures 6.6, B.11a and B.11b.

When applying parsimonious non-linear system identification techniques, if a given coordinate system does not enable a sparse representation of the dynamics, the task at hand is not simply model discovery but rather the joint discovery of suitable coordinates and a model. To address this, Champion et al. developed the SINDy autoencoder (AE) [82] - an extension of SINDy that combines the SINDy optimisation procedure with the optimisation of an autoencoder. The role of the autoencoder is to discover a coordinate transformation that enables a sparse representation of the dynamics. The SINDy model is constructed in terms of the latent variables of the autoencoder (the middle layer). An autoencoder can be thought of as a non-linear generalisation of the SVD [79]. Like the SVD, there is no guarantee an autoencoder will learn a suitable coordinate transformation when trained in iso-

lation. Hence, the innovation of SINDy AE is the joint optimisation of the SINDy model and the autoencoder. This is facilitated by a combined loss function, which promotes an accurate autoencoder reconstruction and a sparse, accurate dynamical model. We believe the application of SINDy AE to the problem of modelling the time evolution of the structure factor during polymeric spinodal decomposition to be a promising avenue of future research.

Whether using SINDy combined with the SVD or SINDy AE, an important consideration is ensuring that the resulting dynamical model is generalisable. In the case of SINDy AE, the structure of the SINDy model has the potential to generalise to new time series corresponding to different system parameters (thermodynamic and molecular parameters in the context of polymer blends). However, the coordinate transformation, i.e. the autoencoder, is unlikely to generalise. To remedy this, one can retrain the autoencoder using a new time series while keeping the structure of the SINDy model fixed. This optimisation problem is more straightforward than the original joint optimisation problem and should, therefore, be quicker to solve [82]. Retraining the autoencoder is analogous to redefining a coordinate system when drawing free-body diagrams. For example, Newton's laws are equally applicable to objects on a flat or an inclined plane, but for each type of plane, it is convenient to define a different coordinate system. In the case of SINDy combined with the SVD, we are not entirely sure how one might go about ensuring that the resulting dynamical model is generalisable. It would be interesting to see whether the ideas outlined above can be applied, i.e. perhaps a SINDy model structure can be identified with one time series and then refit to a new time series - recalibrating the coefficients. Here, instead of retraining an autoencoder, one would calculate a new SVD. If there is any success applying SINDy combined with the SVD or SINDy AE, it would be interesting to investigate the possibility of characterising the coefficients in the SINDy model in terms of the molecular and thermodynamic parameters corresponding to each time series.

To end this discussion of potential avenues for future research, we wish to highlight that we only addressed the scaling of the synthetic structure factor snapshots in the time series and not the translation phenomena. Since accounting for the scaling of the snapshots led to such an improvement in the five-mode SVD reconstructions, we are inclined to believe that the scaling was the main issue regarding our initial attempts at reconstructing the snapshots, i.e. the effects of translations were not as detrimental. However, if it is deemed that the effects of translations need addressing, a potentially useful technique might be Unsupervised Travelling Wave Identification with Shifting and Truncation (UnTWIST) [104]. This technique automatically identifies and shifts travelling waves such that they appear stationary in a new reference frame. The technique also allows one to learn an interpretable model describing the, in general, non-constant speed of the reference frame. Shifting the travelling wave snapshots should aid one in obtaining accurate low-rank SVD reconstructions of the snapshots.

6.4 Summary

We investigated the application of two parsimonious non-linear system identification techniques - parametric PDE-FIND and SINDy combined with the SVD - to the problem of modelling the time evolution of the structure factor during polymeric

spinodal decomposition.

The application of parametric PDE-FIND to the problem is not well-founded. This technique requires that the state vector is represented in a coordinate system that enables a sparse representation of the dynamics and that the library of candidate functions is overcomplete. Clearly, in the experimental coordinate system, this is not possible - the full equation of motion for the structure factor during spinodal decomposition is unclosed. Naively, we neglected this and sought to investigate whether parametric PDE-FIND can be used to identify parametric integro-differential equations. We were motivated by the idea of learning an approximate equation of motion for the structure factor during spinodal decomposition. The Akcasu equation suggests that integral basis functions are more appropriate than differential basis functions, hence our interest in parametric integro-differential equations. We found that the linear dependency between integral basis functions makes the sparse regression problem difficult to solve accurately.

To make progress, we believe the use of coordinate transformations will be vital. Coordinate transformations have the potential to enable a sparse representation of the dynamics in terms of linearly independent basis functions. In this direction, we considered SINDy combined with the SVD. We sought to investigate how well the synthetic structure factor snapshots in the critical shallow and off-critical deep time series can be reconstructed using the SVD - a prerequisite task for using SINDy to model the dynamics of the structure factor in the space spanned by reduced SVD modes. A successful application of SINDy combined with the SVD would likely require accurate SVD reconstructions using as few modes as possible. We found that many modes were required to reconstruct the synthetic structure factor snapshots. Noting that the SVD breaks down when there are translations and scaling, we addressed scaling in the time series by taking the log of the constituent snapshots. We found that fairly accurate low-rank reconstructions of the snapshots are possible when the scaling of the snapshots has been accounted for in this way.

A natural next step would be to try to construct SINDy models for the reduced SVD mode amplitudes corresponding to the log of the critical shallow and off-critical deep time series. If this fails, a promising technique to consider is SINDy AE, which combines both coordinate and model discovery via the joint optimisation of an autoencoder and a SINDy model in terms of the latent variables of the autoencoder. We are excited to see how this work develops in the future, especially as the field of system identification grows and matures. Indeed, we believe this problem could be a stimulating test bed for future system identification techniques.

Chapter 7

Conclusions and future work

The time evolution of the structure factor during polymeric spinodal decomposition and dissolution is relatively easy to measure but hard to model. We believe the latter could be impeding our ability to control these processes, preventing us from tailoring and tuning the microstructures of materials derived from polymer blends. In an attempt to rectify this, we set out to

- Test the Akcasu equation for describing the time evolution of the structure factor
- Explore the application of system identification techniques to the problem of modelling the time evolution of the structure factor

To allow us to have as much control as possible in our investigations, we worked with synthetic time series of structure factor snapshots. In chapter 3, we detailed how we generated these time series. The method we used involves a finite difference scheme for simulating polymeric spinodal decomposition and dissolution. When using finite difference simulations, one must be careful in the selection of Δx and $\Delta\tau$ values. We discussed how we chose suitable values of Δx and $\Delta\tau$, demonstrating that the time series we generated are independent of these values. Furthermore, we showed that the snapshots in the dissolution time series tend towards de Gennes' random phase approximation for the static structure factor, indicating our method for generating the time series was derived and implemented correctly. The code and data we developed is available on GitHub [96].

In chapter 4, we tested the Akcasu equation. One of our aims was to shed light on the quantitative discrepancy between the predictions of the Akcasu equation and experimental scattering data reported by Akcasu et al. [31] in the case of dissolution. It was unclear whether the Akcasu equation failed as a result of the equation being inadequate or incorrect parameter values being used. We found that the Akcasu equation applied to dissolution performed much better when tested on the synthetic structure factor snapshots in the dissolution time series than it did when tested using experimental scattering data. Since the parameter values corresponding to the synthetic structure factor snapshots are known, this suggests that the experimental discrepancy could have been due to incorrect parameter values. We hope these findings motivate further testing of the Akcasu equation applied to dissolution using experimental data.

Based on different assumptions, we defined and tested two versions of the Akcasu equation applied to spinodal decomposition: the Akcasu equation applied to

spinodal decomposition under the assumption of a small temperature jump and the Akcasu equation applied to general spinodal decomposition. The former captured some important qualitative features of the dynamics of the synthetic structure factor snapshots in the critical shallow time series but lacked accuracy. The latter completely failed to describe the dynamics of the synthetic structure factor snapshots. We traced this failure back to the noise term and hypothesise that this term may need to be time-dependent, shifting between two limiting values. We hope our findings from testing the Akcasu equation applied to spinodal decomposition motivate further theoretical work aimed towards the development of an approximate equation of motion for the structure factor during spinodal decomposition. As far as we know, these are the first reported findings for testing the Akcasu equation applied to spinodal decomposition.

In chapter 5, we turned our attention towards the application of system identification techniques to the problem of modelling the time evolution of the structure factor during spinodal decomposition. Specifically, we investigated the use of DMD to predict future snapshots of the synthetic structure factor based on the knowledge of previous snapshots. For both the critical shallow and off-critical deep time series, DMD was able to accurately model the time evolution of the synthetic structure factor snapshots when applied recursively. We identified a trade-off between the accuracy and extrapolation of the DMD predictions, which seemed to be time-dependent: as spinodal decomposition proceeds, it becomes less important.

We believe our findings are promising for the development of an experimental technique to predict structure factor snapshots and microstructure characteristics during spinodal decomposition. Such predictions could be useful in a control system. A limitation of our DMD investigation is that the synthetic structure factor snapshots we used are idealised. To address this, we propose that future research should aim to demonstrate whether our findings can be replicated with more realistic (e.g. noisy and incomplete) synthetic time series of structure factor snapshots and, eventually, experimental scattering data. Extensions to DMD, such as BOP-DMD, which was developed to handle noise, might need to be considered.

In chapter 6, we investigated the application of parametric PDE-FIND and SINDy combined with the SVD to the problem of modelling the time evolution of the structure factor during spinodal decomposition. Contrary to DMD, which is linear and equation-free, parametric PDE-FIND and SINDy combined with the SVD output parsimonious non-linear governing equations.

We determined that the application of parametric PDE-FIND to the problem is not well-founded. Among several issues is that parametric PDE-FIND requires the structure factor to be represented in a coordinate system that enables a sparse representation of the dynamics - this is not the case in the experimental coordinate system since the full equation of motion is unclosed. To make progress, we believe the use of coordinate transformations will be vital, which led us to consider SINDy combined with the SVD. The reduced SVD allows one to approximate spatio-temporal time series in terms of a few dominant modes whose amplitudes evolve with time. SINDy can be used to model the time evolution of the reduced SVD mode amplitudes.

Before applying SINDy to model the time evolution of the reduced mode amplitudes, a prerequisite task is to investigate how well the reduced SVD can reconstruct the synthetic structure factor snapshots under consideration. For both the critical shallow and off-critical deep time series, we found that fairly accurate low-rank re-

constructions of the synthetic structure factor snapshots were possible when the scaling of the snapshots was accounted for by taking the log of the snapshots. Due to time constraints, we did not attempt to construct any SINDy models for the time evolution of the reduced SVD mode amplitudes. This would be a natural next step. If this were to fail, we identified SINDy AE as a promising technique to investigate. SINDy AE combines both coordinate and model discovery via the joint optimisation of an autoencoder and a SINDy model in terms of the latent variables of the autoencoder.

As far as we know, our work in chapters 5 and 6 is the first to attempt applying system identification techniques to the problem of modelling the time evolution of the structure factor during spinodal decomposition. We believe this problem could be a stimulating test bed for future system identification techniques, and we hope our findings provide a solid starting point for future research.

Appendix A

Supplementary information for chapter 3

This appendix contains supplementary information for chapter 3 and is split into two sections. In section A.1, we derive equations 3.1, 3.5 and 3.7. In section A.2, we attempt to quantify the small-k limit of equation 3.1.

A.1 Deriving the key equations

Finite difference scheme (equation 3.1)

To begin the derivation, we nondimensionalise equation 2.62. We make use of the dimensionless variables in equations 3.4a - 3.4c. Upon substituting these dimensionless variables into equation 2.62, we obtain, after rearranging,

$$\frac{\partial\phi(\boldsymbol{x},\tau)}{\partial\tau} = \frac{1}{2}\tilde{\nabla}^2\Big[\frac{\chi_c}{2|\chi-\chi_s|}\ln\Big(\frac{\phi}{1-\phi}\Big) - \frac{2\chi\phi}{|\chi-\chi_s|} + \frac{1}{36}\Big(\frac{1-2\phi}{(\phi(1-\phi))^2}\Big)(\tilde{\nabla}\phi)^2 - 2\Big(\frac{1}{36\phi(1-\phi)}\Big)\tilde{\nabla}^2\phi\Big] + \tilde{\xi}(\boldsymbol{x},\tau). \quad \text{(A.1)}$$

Next, we write equation A.1 in a slightly different form. A rescaled dimensionless noise term $\nu(\boldsymbol{x},\tau) = \frac{\sigma^{3/2}}{v_0^{1/2}|\chi-\chi_s|^{1/4}}\tilde{\xi}(\boldsymbol{x},\tau)$ can be identified by substituting equations 3.4a - 3.4c into equation 2.54b. Upon substituting $\tilde{\xi}(\boldsymbol{x},\tau) = \frac{v_0^{1/2}|\chi-\chi_s|^{1/4}}{\sigma^{3/2}}\nu(\boldsymbol{x},\tau)$ into equation A.1, we obtain

$$\frac{\partial\phi(\boldsymbol{x},\tau)}{\partial\tau} = \frac{1}{2}\tilde{\nabla}^2\Big[\frac{\chi_c}{2|\chi-\chi_s|}\ln\Big(\frac{\phi}{1-\phi}\Big) - \frac{2\chi\phi}{|\chi-\chi_s|} + \frac{1}{36}\Big(\frac{1-2\phi}{(\phi(1-\phi))^2}\Big)(\tilde{\nabla}\phi)^2 - 2\Big(\frac{1}{36\phi(1-\phi)}\Big)\tilde{\nabla}^2\phi\Big] + \frac{v_0^{1/2}|\chi-\chi_s|^{1/4}}{\sigma^{3/2}}\nu(\boldsymbol{x},\tau). \quad \text{(A.2)}$$

The first and second moments of $\nu(\boldsymbol{x},\tau)$ are given by

$$< \nu(\boldsymbol{x},\tau) >= 0 \quad \text{(A.3a)}$$

$$< \nu(\boldsymbol{x},\tau)\nu(\boldsymbol{x}',\tau') >= -\tilde{\nabla}^2\delta(\boldsymbol{x}-\boldsymbol{x}')\delta(\tau-\tau'). \quad \text{(A.3b)}$$

We note that a common simplification to equation A.2 used in previous theoretical and computational studies of spinodal decomposition is to set v_0 equal to unity [26,53,105,106]. Similarly, in some studies, σ has also been set equal to unity [90–92].

Ultimately, we want to write down the numerical solution to equation A.2. Therefore, following [53], we introduce some discretisation approximations. Specifically, we approximate continuous time as a series of discrete time steps of duration $\Delta\tau$ and continuous space as a simple cubic lattice (with periodic boundary conditions) comprising N_s^3 lattice sites of length Δx. We label the lattice sites with the indices (j,k,l) and the time steps with the index m. To approximate the spatial derivatives, we use central finite difference schemes. After integrating the resulting discretised equation over a single time step, we write the numerical solution as [53, 107–109]

$$\begin{aligned}\phi_{j,k,l}^{m+1} =& \phi_{j,k,l}^{m} + \frac{\Delta\tau}{2\Delta x^2}\sum_{nn}\Big[\frac{\chi_c}{2|\chi-\chi_s|}\ln\Big(\frac{\phi_{j,k,l}^{m}}{1-\phi_{j,k,l}^{m}}\Big) - \frac{2\chi\phi_{j,k,l}^{m}}{|\chi-\chi_s|} \\ &+ \frac{1}{36}\Big(\frac{1-2\phi_{j,k,l}^{m}}{(\phi_{j,k,l}^{m}(1-\phi_{j,k,l}^{m}))^2}\Big)\frac{1}{4\Delta x^2}\prod_{nn}\phi_{j,k,l}^{m} \\ &- 2\Big(\frac{1}{36\phi_{j,k,l}^{m}(1-\phi_{j,k,l}^{m})}\Big)\frac{1}{\Delta x^2}\sum_{nn}\phi_{j,k,l}^{m}\Big] + \frac{v_0^{1/2}|\chi-\chi_s|^{1/4}}{\sigma^{3/2}}M_{j,k,l}^{m},\end{aligned} \tag{A.4}$$

where $\sum_{nn}$ and $\prod_{nn}$ are the short-hand operators in equations 3.2a and 3.2b and $M_{j,k,l}^{m} = \int_{\tau}^{\tau+\Delta\tau}\nu(\boldsymbol{x},\tau)d\tau$. We approximated the integral of the term with the square brackets as a Riemann sum with a single term.

To make use of equation A.4, we must specify how to implement $M_{j,k,l}^{m}$. Following [108, 109], we use equation A.3 to compute

$$< M_{j,k,l}^{m} >= 0 \tag{A.5a}$$

$$< M_{j,k,l}^{m} M_{j',k',l'}^{m'} >= -\tilde{\nabla}^2\delta(\boldsymbol{x}-\boldsymbol{x}')\delta_{m,m'}\Delta\tau. \tag{A.5b}$$

Approximating the Laplacian using central finite differences and $\delta(\boldsymbol{x}-\boldsymbol{x}')$ as $\frac{\delta_{j,j'}\delta_{k,k'}\delta_{l,l'}}{\Delta x^3}$, we obtain

$$< M_{j,k,l}^{m} M_{j',k',l'}^{m'} >= -\frac{1}{\Delta x^2}\sum_{nn}\Big(\frac{\delta_{j,j'}\delta_{k,k'}\delta_{l,l'}}{\Delta x^3}\Big)\delta_{m,m'}\Delta\tau. \tag{A.6}$$

It can be shown that

$$< M_{j,k,l}^{m} M_{j',k',l'}^{m'} >= \begin{cases} \frac{6\Delta\tau}{\Delta x^5} & \text{if } (j,k,l) = (j',k',l') \text{ and } m = m' \\ \frac{-\Delta\tau}{\Delta x^5} & \text{if } (j,k,l) \text{ and } (j',k',l') \text{ are NN and } m = m' \\ 0 & \text{otherwise} \end{cases}, \tag{A.7}$$

where NN is an abbreviation for nearest neighbours. When $m = m'$, the second line on the right-hand side of this equation reveals the covariance of $M_{j,k,l}^{m}$ is negative for lattice sites that are nearest neighbours. Therefore, positive values of $M_{j,k,l}^{m}$ at one lattice site, which correspond to an increase in $\phi_{j,k,l}^{m}$, are compensated by negative values at the neighbouring lattice sites and vice versa. It follows that material is conserved. Ultimately, this conservation property stems from the presence of ∇^2

in equation 2.56. Replacing ∇^2 in equation 2.56 with a numerical factor results in the covariance term in the second line of equation A.7 becoming zero. In this case, material would no longer be conserved.

To generate values of $M^m_{j,k,l}$ in accordance with equations A.5a and A.6, we follow [97, 105, 108] in defining

$$M^m_{j,k,l} = \frac{1}{\Delta x}\big[\eta^m_{1;j+1,k,l} - \eta^m_{1;j,k,l} + \eta^m_{2;j,k+1,l} - \eta^m_{2;j,k,l} + \eta^m_{3;j,k,l+1} - \eta^m_{3;j,k,l}\big], \tag{A.8}$$

where the η_n are independent Gaussian random variables with the following statistical properties:

$$< \eta^m_{n;j,k,l} >= 0 \tag{A.9a}$$

$$< \eta^m_{n;j,k,l}\eta^{m'}_{n';j',k',l'} >= \frac{\Delta\tau}{\Delta x^3}\delta_{n,n'}\delta_{j,j'}\delta_{k,k'}\delta_{l,l'}\delta_{m,m'}. \tag{A.9b}$$

Finally, upon substituting equation A.8 into equation A.4, we obtain equation 3.1.

Snapshots of the power spectrum and the structure factor (equations 3.5 and 3.7)

To begin the derivation, we nondimensionalise equation 2.92. We make use of the dimensionless variables in equations 3.4a, 3.8a, and 3.8b. Upon substituting these dimensionless variables into equation 2.92, we obtain, after rearranging,

$$\tilde{S}(\mathrm{k},\tau) = \frac{1}{\tilde{V}}\Big\langle \int d^3x\; e^{-i\mathbf{k}\cdot\boldsymbol{x}}\delta\phi(\boldsymbol{x},\tau)\int d^3x'\; e^{i\mathbf{k}\cdot\boldsymbol{x}'}\delta\phi(\boldsymbol{x}',\tau)\Big\rangle, \tag{A.10}$$

where $\tilde{V} = \frac{V|\chi-\chi_s|^{\frac{3}{2}}}{\sigma^3}$. We note that the expression inside the angle brackets is the dimensionless power spectrum $\tilde{P}(\mathrm{k},\tau)$, i.e. a dimensionless version of equation 2.93.

Next, consistently with the derivation of the finite difference scheme, we introduce discretisation approximations into equation A.10. Most significantly, we approximate the Fourier transforms as discrete Fourier transforms. The resulting discretised equation can be expressed in two parts:

$$\tilde{S}^m_d = \frac{1}{N_s^3\Delta x^3} < \tilde{P}^m_d > \tag{A.11a}$$

$$\begin{aligned}\tilde{P}^m_d =& \Delta x^6\Big\langle \sum_{j=0}^{N_s-1}\sum_{k=0}^{N_s-1}\sum_{l=0}^{N_s-1}\delta\phi^m_{j,k,l}\; e^{-\frac{2\pi i}{N_s}(aj+bk+cl)} \\ & \sum_{j'=0}^{N_s-1}\sum_{k'=0}^{N_s-1}\sum_{l'=0}^{N_s-1}\delta\phi^{m'}_{j',k',l'}e^{\frac{2\pi i}{N_s}(aj'+bk'+cl')}\Big\rangle_R,\end{aligned} \tag{A.11b}$$

where a, b and c are integers in the range $\frac{-(N_s-1)}{2} \le a,b,c \le \frac{N_s-1}{2}$, and $< ... >_R$ denotes a radial average. The radial average can be written explicitly as

$$< f_{a,b,c} >_R \equiv f_d = \frac{\sum_{a,b,c \text{ s.t. } \mathrm{round}(\sqrt{a^2+b^2+c^2})=d} f_{a,b,c}}{\sum_{a,b,c \text{ s.t. } \mathrm{round}(\sqrt{a^2+b^2+c^2})=d} 1}, \tag{A.12}$$

where d is an integer in the range $0 \leq d \leq \frac{N_s-1}{2}$. We introduce the radial average since $\tilde{P}(\mathrm{k},\tau)$ depends only on the magnitude of $\mathbf{k}$ - we expect polymer blends to be isotropic during dissolution and spinodal decomposition. The integers a, b and c are related to $\mathbf{k}$ via $\mathbf{k} = \frac{2\pi}{N_s\Delta x}(a,b,c)$. The integer d is related to $\mathrm{k} = |\mathbf{k}|$ via $\mathrm{k} = \frac{2\pi}{N_s\Delta x}d$.

Next, we propose approximating $c \approx 0$ to make equation A.11b consistent with a small-angle scattering experiment. This corresponds to approximating $q_z \approx 0$, where q_z is the z-component of $\boldsymbol{q}$, and reduces the three-dimensional discrete Fourier transforms in equation A.11b to two-dimensional discrete Fourier transforms:

$$\tilde{P}_d^m = \Delta x^6 \Big\langle \sum_{j=0}^{N_s-1}\sum_{k=0}^{N_s-1}\sum_{l=0}^{N_s-1} \delta\phi_{j,k,l}^m \, e^{-\frac{2\pi i}{N_s}(aj+bk)} \sum_{j'=0}^{N_s-1}\sum_{k'=0}^{N_s-1}\sum_{l'=0}^{N_s-1} \delta\phi_{j',k',l'}^{m'} e^{\frac{2\pi i}{N_s}(aj'+bk')} \Big\rangle_R. \tag{A.13}$$

The radial average becomes

$$< f_{a,b} >_R \equiv f_d = \frac{\sum_{a,b \text{ s.t. } \mathrm{round}(\sqrt{a^2+b^2})=d} f_{a,b}}{\sum_{a,b \text{ s.t. } \mathrm{round}(\sqrt{a^2+b^2})=d} 1}. \tag{A.14}$$

Our logic behind approximating $q_z \approx 0$ is as follows. Consider figure 1.2, which shows a schematic of a typical small-angle scattering experiment. Defining the z-axis to be parallel to the incident beam, the scattering vector of an arbitrary scattering event is given by

$$\boldsymbol{q} = \boldsymbol{q}_f - \boldsymbol{q}_i = \begin{pmatrix} q_{f,x} \\ q_{f,y} \\ q_{f,z} \end{pmatrix} - \begin{pmatrix} 0 \\ 0 \\ q_{i,z} \end{pmatrix} = \begin{pmatrix} q_{f,x} \\ q_{f,y} \\ q_{f,z} - q_{i,z} \end{pmatrix}. \tag{A.15}$$

Assuming that the scattering is elastic (therefore $|\boldsymbol{q}_i| = |\boldsymbol{q}_f|$), it can be deduced using trigonometry that

$$q_z = |q_f|(\cos(\theta) - 1). \tag{A.16}$$

By definition, the scattering angle in small-angle scattering is small, therefore

$$q_z = |q_f|\Big(1 - \frac{\theta^2}{2!} + \frac{\theta^4}{4!} - ... - 1\Big) \approx 0. \tag{A.17}$$

Finally, for simplicity, we propose neglecting the time average represented by $< ... >$ in equation A.11a. Instead, noting that the sizes of simulated blends are significantly smaller than the sizes of blends studied experimentally, we propose taking $< ... >$ to mean an ensemble average [15, 16]. This allows us to model the scattering throughout a 'large' experimental blend using N_r simulations of 'small' blends:

$$\tilde{S}_d^m = \frac{1}{N_r N_s^3 \Delta x^3} \sum_{n=1}^{N_r} \tilde{P}_{n;d}^m \tag{A.18a}$$

$$\tilde{P}_{n;d}^m = \Delta x^6 \Big\langle \sum_{j=0}^{N_s-1}\sum_{k=0}^{N_s-1}\sum_{l=0}^{N_s-1} \delta\phi_{n;j,k,l}^m \, e^{-\frac{2\pi i}{N_s}(aj+bk)} \sum_{j'=0}^{N_s-1}\sum_{k'=0}^{N_s-1}\sum_{l'=0}^{N_s-1} \delta\phi_{n;j',k',l'}^{m'} e^{\frac{2\pi i}{N_s}(aj'+bk')} \Big\rangle_R. \tag{A.18b}$$

These equations are equivalent to equations 3.7 and 3.5, respectively.

A.2 Quantifying the small-k limit of equation 3.1

The small-k limit of equation 3.1 stems from deriving the square gradient coefficient to be consistent with the small-q limit of de Gennes' random phase approximation (see section 2.4.9). Specifically, instead of using complete Debye functions in the derivation of the square gradient coefficient, de Gennes used its linear expansion, which is only valid in the limit $qR_g = \mathrm{k}r_g << 1$. We attempt to quantify this limit below.

The dimensionless radius of gyration is given by

$$r_g = \sqrt{\frac{N|\chi - \chi_s|}{6}}. \tag{A.19}$$

Therefore, the limit $\mathrm{k}r_g << 1$ can be written as

$$\mathrm{k}\sqrt{\frac{N|\chi - \chi_s|}{6}} << 1. \tag{A.20}$$

Substituting $N = 2700$ and the values of χ and χ_s corresponding to each time series into equation A.19, we determine that

- $r_g \approx 0.10 \implies \mathrm{k} << 10$ in the case of the critical shallow and dissolution time series
- $r_g \approx 0.24 \implies \mathrm{k} << 4.2$ in the case of the off-critical deep time series

In an attempt to quantify what is meant by '<<', we turn to the Debye function and its linear expansion:

$$f_D(x) = \frac{2}{x^2}\Big(x - 1 + e^{-x}\Big) \approx 1 - \frac{x}{3}, \tag{A.21}$$

where $x = (qR_g)^2 = (\mathrm{k}r_g)^2$. Figure A.1 shows the percentage error between the Debye function and its linear expansion as a function of x. At $x = 0.5$, the percentage error is approximately 2.22 %, which suggests the linear expansion is a good approximation to the full Debye function when $x \leq 0.5$. Using $x \leq 0.5$ and the values of r_g listed above, we determine the following small-k limit inequalities:

- $\mathrm{k} < 7$ in the case of the critical shallow and dissolution time series
- $\mathrm{k} < 3$ in the case of the off-critical deep time series

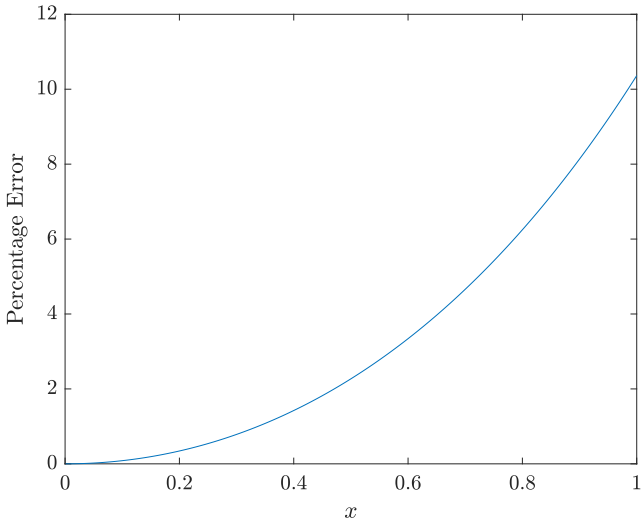

Figure A.1: The percentage error between the full Debye function and its linear expansion as a function of $x = (qR_g)^2 = (\mathrm{k}r_g)^2$.

Appendix B

Supplementary results for chapters 5 and 6

B.1 Supplementary results for chapter 5

B.1.1 Critical shallow time series

Figures B.1 and B.2 present the same comparison as figures 5.1 and 5.3, respectively, but with a log scale (base 10) on the y-axis.

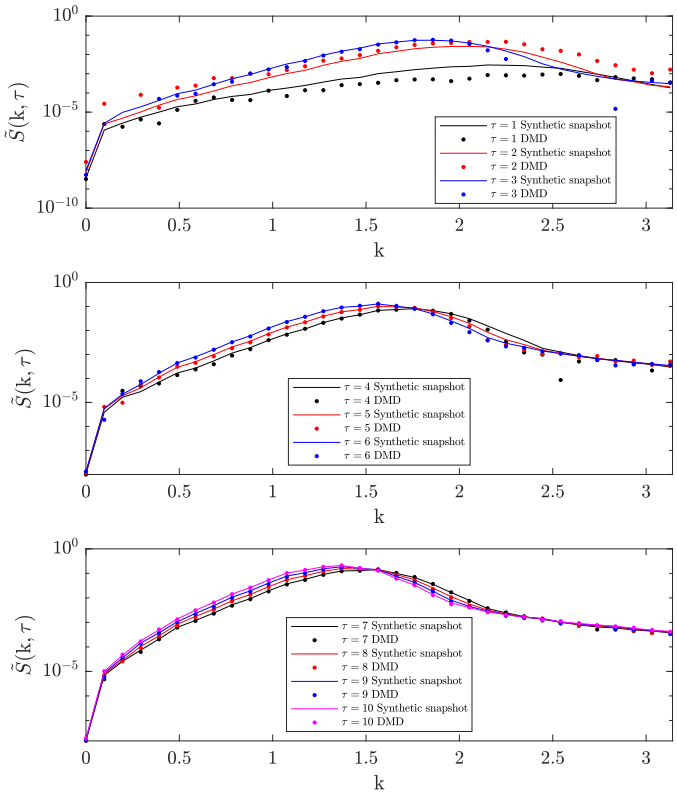

Figure B.1: A reproduction of figure 5.1 with a log-scale (base 10) on the y-axis.

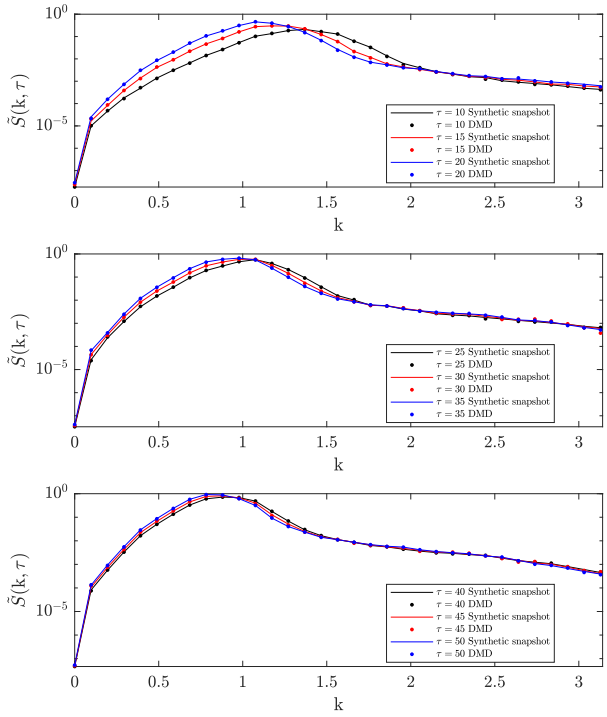

Figure B.2: A reproduction of figure 5.3 with a log-scale (base 10) on the y-axis.

B.1.2 Off-critical deep time series

Figures B.3 and B.4 compare several synthetic structure factor snapshots from the off-critical deep time series with those predicted by DMD models. The snapshots in figure B.3 correspond to values of τ in the range $1 \leq \tau \leq 10$, while the snapshots in figure B.4 correspond to values of τ in the range $10 \leq \tau \leq 50$. The hyperparameters used in the DMD models are listed in section 5.2. Figures B.5 and B.6 show a box plot of the percentage errors associated with the predictions of each DMD model in figures B.3 and B.4, respectively. From figures B.3 - B.6 we infer that, with the exception of the early stage of the process ($\tau < 3$), DMD can be used to accurately model the time evolution of the synthetic structure factor snapshots.

Figure B.7 compares the predictions of DMD models obtained using values of $\tau_{ph} < 0.75$ at $\tau = 1$ and $\tau = 3$ with the corresponding synthetic structure factor snapshots. Figure B.8 compares the predictions of DMD models obtained using values of $\tau_{ph} > 0.75$ at $\tau = 20, 30, 40$ and 50 with the corresponding synthetic structure factor snapshots. The results in figures B.7 - B.8 illustrate the trade-off between the accuracy and extrapolation of the DMD predictions, which is coupled to the value of τ.

Overall, the results presented in this section, which we obtained with the off-critical deep time series, are consistent with the results presented in section 5.3, which we obtained using the critical shallow time series.

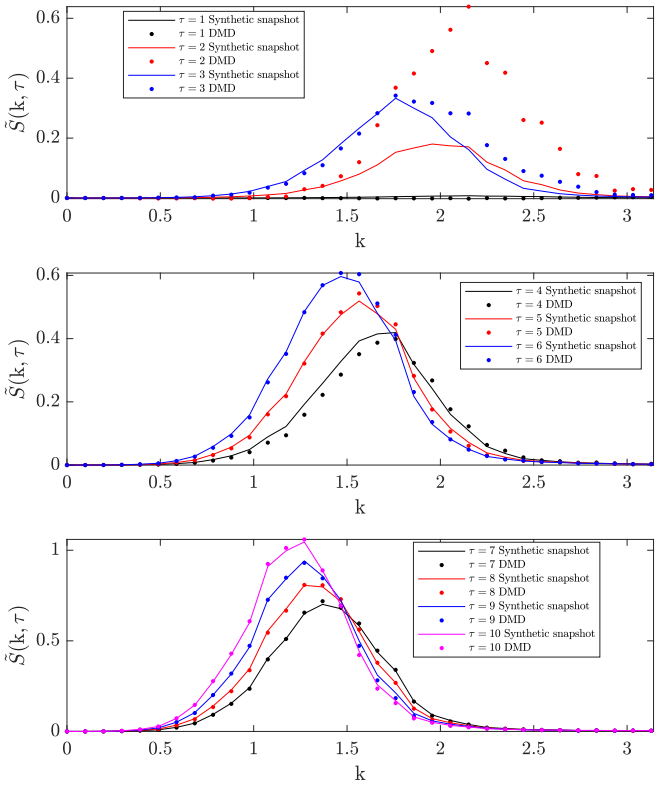

Figure B.3: A comparison between synthetic structure factor snapshots from the off-critical deep time series and those predicted by the DMD models for values of τ in the range $1 \leq \tau \leq 10$. The hyperparameters used in the DMD models are listed in section 5.2.

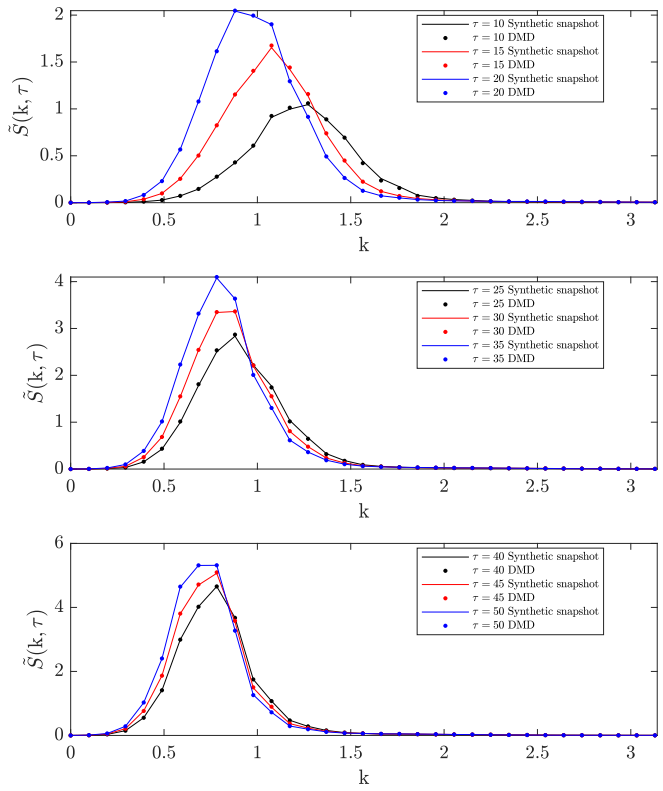

Figure B.4: A comparison between synthetic structure factor snapshots from the off-critical deep time series and those predicted by the DMD models for values of τ in the range $10 \leq \tau \leq 50$. The hyperparameters used in the DMD models are listed in section 5.2.

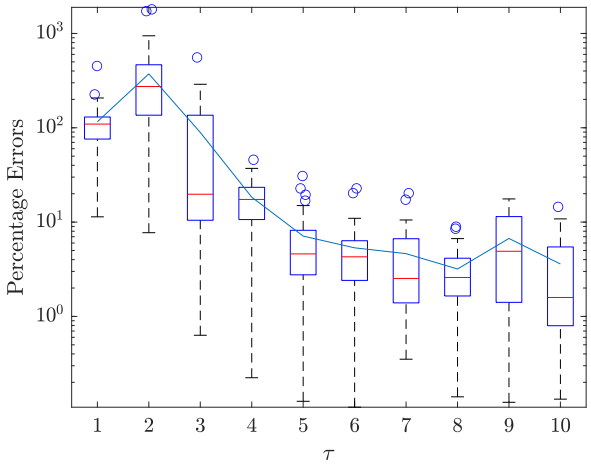

Figure B.5: Box plots of the percentage errors associated with the predictions of each DMD model in figure B.3. In each box plot, the red line shows the median, the blue box outlines the interquartile range, the black dotted lines extend beyond the box by 1.5 times the interquartile range, and the blue circles denote outliers. The solid blue line shows the time evolution of the mean.

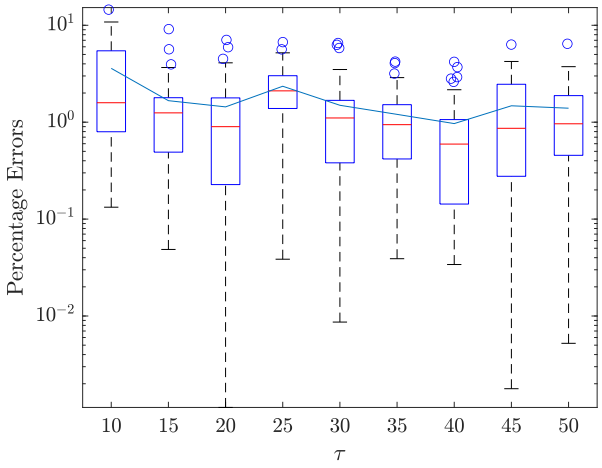

Figure B.6: Box plots of the percentage errors associated with the predictions of each DMD model in figure B.4. In each box plot, the red line shows the median, the blue box outlines the interquartile range, the black dotted lines extend beyond the box by 1.5 times the interquartile range, and the blue circles denote outliers. The solid blue line shows the time evolution of the mean.

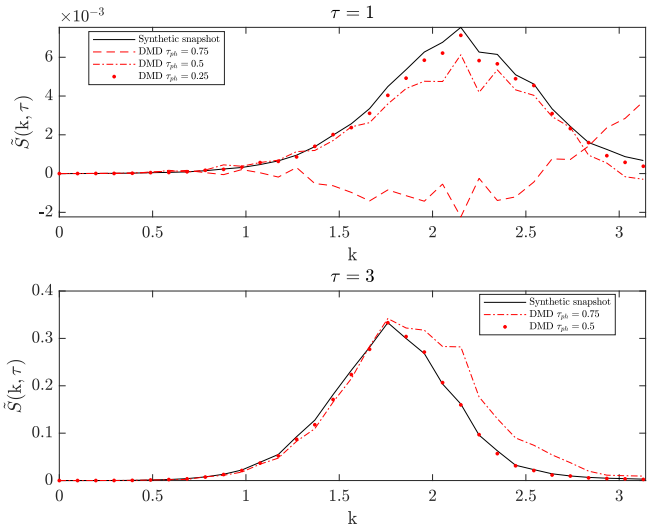

Figure B.7: A comparison between synthetic structure factor snapshots from the off-critical deep time series and those predicted by DMD models with values of $\tau_{ph} < 0.75$ at $\tau = 1$ (top panel) and $\tau = 3$ (bottom panel). The values of the other hyperparameters used in the DMD models are the same as those listed in section 5.2.

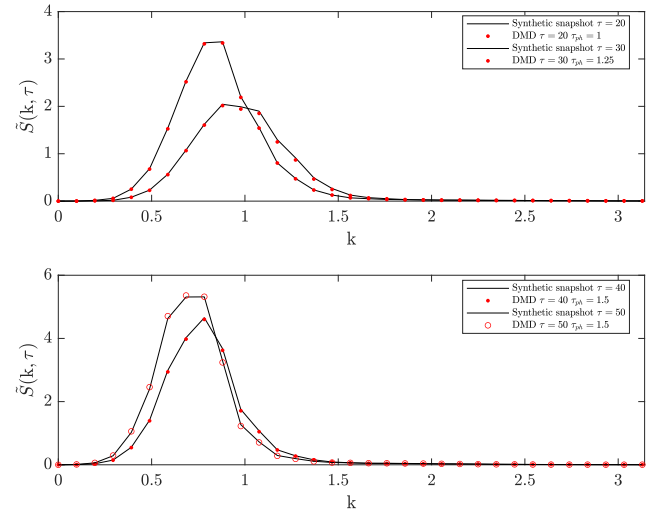

Figure B.8: A comparison between synthetic structure factor snapshots from the off-critical deep time series and those predicted by DMD models with values of $\tau_{ph} > 0.75$ at $\tau = 20$ and 30 (top panel) and $\tau = 40$ and 50 (bottom panel). The values of the other hyperparameters used in the DMD models are the same as those listed in section 5.2.

B.2 Supplementary results for chapter 6

In the case of the critical shallow time series, figures B.9a and B.9b compare the five-mode reconstruction of synthetic structure factor snapshots with the originals at $\tau = 0.25, 0.5, 0.75, 1$ and $\tau = 10, 20, 30, 40, 50$, respectively. Similarly, figures B.10a and B.10b compare the 25-mode reconstruction of synthetic structure factor snapshots with the originals at $\tau = 0.25, 0.5, 0.75, 1$ and $\tau = 10, 20, 30, 40, 50$, respectively. We note that the snapshots in the figures are presented with a log scale on the y-axis.

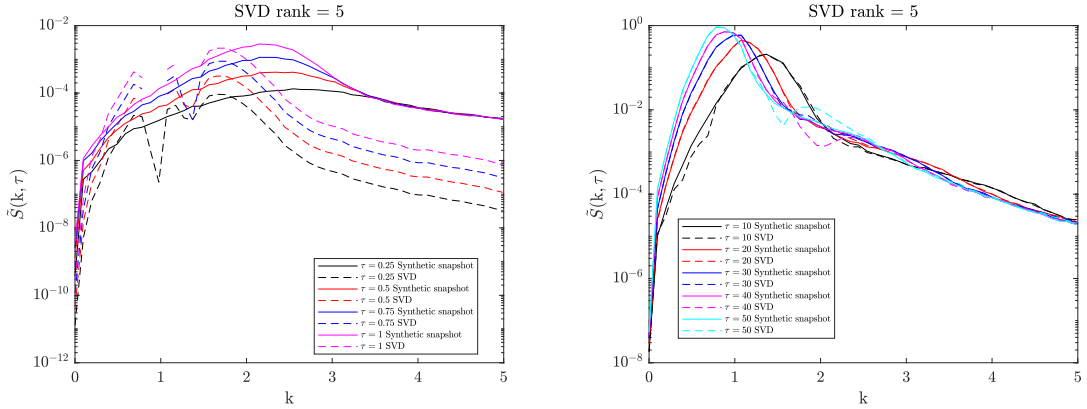

(a) (b)

Figure B.9: A comparison between the five-mode SVD reconstruction of synthetic structure factor snapshots from the critical shallow time series and the originals at (a) $\tau = 0.25, 0.5, 0.75, 1$ and (b) $\tau = 10, 20, 30, 40, 50$. The snapshots are presented with a log scale on the y-axis. Some of the reconstructed values were negative. These values are not plotted.

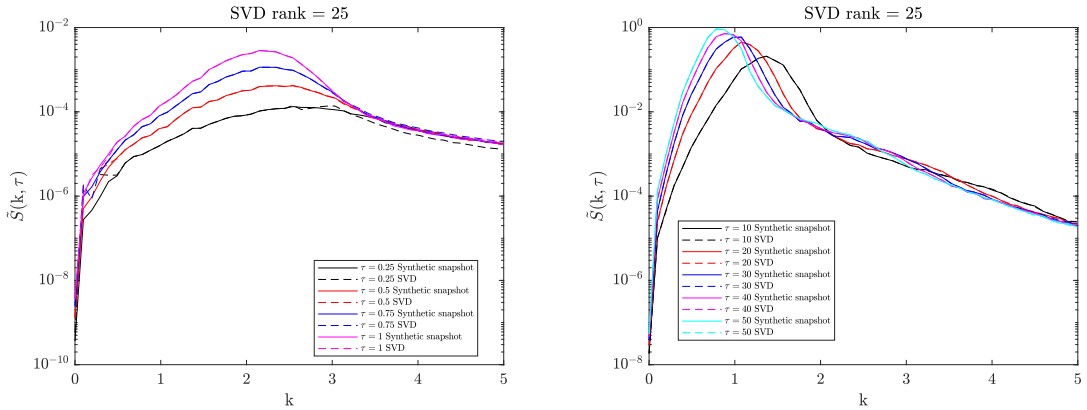

(a) (b)

Figure B.10: A comparison between the 25-mode SVD reconstruction of synthetic structure factor snapshots from the critical shallow time series and the originals at (a) $\tau = 0.25, 0.5, 0.75, 1$ and (b) $\tau = 10, 20, 30, 40, 50$. The snapshots are presented with a log scale on the y-axis. Some of the reconstructed values were negative. These values are not plotted.

In the case of the log (base 10) of the critical shallow time series, figures B.11a and B.11b compare the five-mode reconstruction of synthetic structure factor snapshots with the originals at $\tau = 0.25, 0.5, 0.75, 1$ and $\tau = 10, 20, 30, 40, 50$, respectively. In the case of the log (base 10) of the off-critical deep time series, figures B.12a and B.12b compare the five-mode reconstruction of synthetic structure factor snapshots with the originals at $\tau = 0.25, 0.5, 0.75, 1$ and $\tau = 10, 20, 30, 40, 50$, respectively.

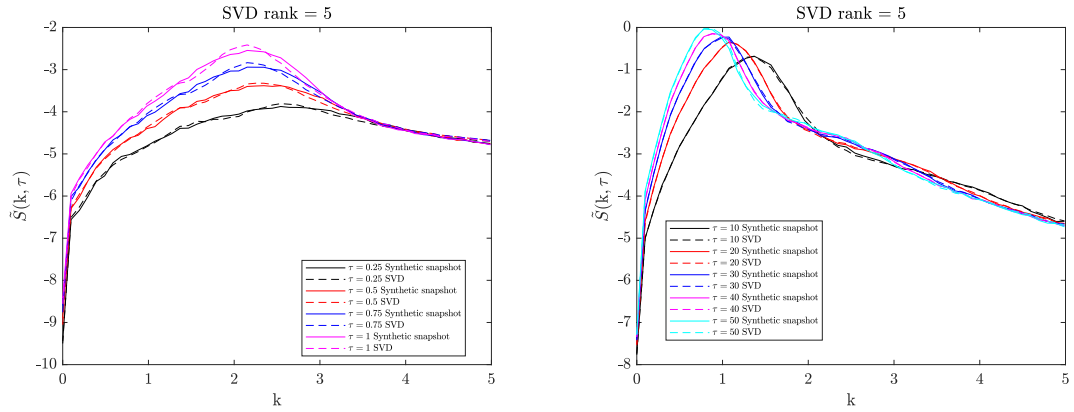

(a) (b)

Figure B.11: A comparison between the five-mode SVD reconstruction of the log (base 10) of synthetic structure factor snapshots from the critical shallow time series and the originals at (a) $\tau = 0.25, 0.5, 0.75, 1$ and (b) $\tau = 10, 20, 30, 40, 50$.

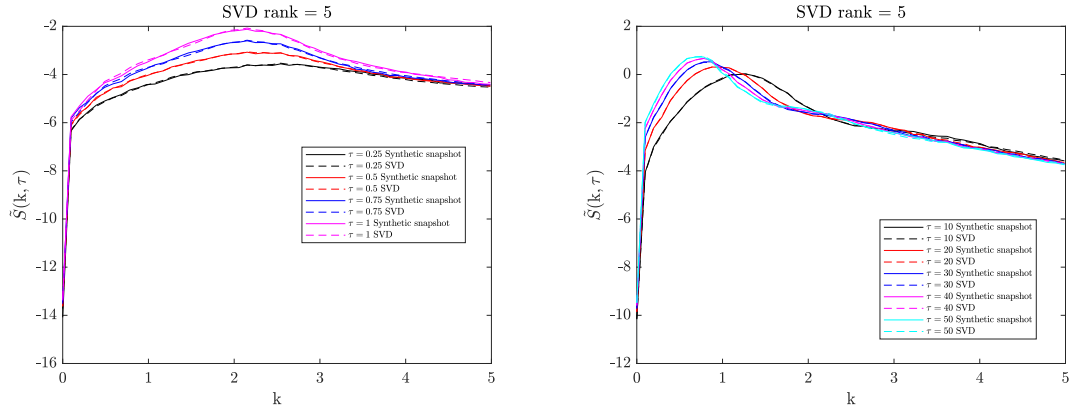

(a) (b)

Figure B.12: A comparison between the five-mode SVD reconstruction of the log (base 10) of synthetic structure factor snapshots from the off-critical deep time series and the originals at (a) $\tau = 0.25, 0.5, 0.75, 1$ and (b) $\tau = 10, 20, 30, 40, 50$.

Bibliography

[1] S. Thomas, Y. Grohens, and P. Jyotishkumar. *Characterization of Polymer Blends: Miscibility, Morphology and Interfaces*. Wiley-Blackwell, 2014.

[2] J. T. Cabral and J. S. Higgins. Spinodal nanostructures in polymer blends: On the validity of the Cahn-Hilliard length scale prediction. *Progress in Polymer Science*, 81:1–21, 2018.

[3] S. L. Burg, A. Washington, D. M. Coles, A. Bianco, D. Mcloughlin, O. O. Mykhaylyk, J. Villanova, A. J. C. Dennison, C. J. Hill, P. Vukusic, S. Doak, S. J. Martin, M. Hutchings, S. R. Parnell, C. Vasilev, N. Clarke, A. J. Ryan, W. Furnass, M. Croucher, R. M. Dalgliesh, S. Prevost, R. Dattani, A. Parker, R. A. L. Jones, J. Patrick, A. Fairclough, and A. J. Parnell. Liquid-liquid phase separation morphologies in ultra-white beetle scales and a synthetic equivalent. *Communications Chemistry*, 2(100), 2019.

[4] C. M. Portela, A. Vidyasagar, S. Krödel, T. Weissenbach, D. W. Yee, J. R. Greer, and D. M. Kochmann. Extreme mechanical resilience of self-assembled nanolabyrinthine materials. *Proceedings of the National Academy of Sciences of the United States of America*, 117(11):5686–5693, 2020.

[5] G. A. Buxton and N. Clarke. Predicting structure and property relations in polymeric photovoltaic devices. *Physical Review B*, 74(8):085207, 2006.

[6] R. A. L. Jones. *Soft Condensed Matter*. Oxford University Press, 2002.

[7] G. Strobl. *The Physics of Polymers*. Springer, 2007.

[8] J. Kumaki and T. Hashimoto. Time-Resolved Light Scattering Studies on Kinetics of Phase Separation and Phase Dissolution of Polymer Blends. 4. Kinetics of Phase Dissolution of a Binary Mixture of Polystyrene and Poly (vinyl methyl ether). *Macromolecules*, 19(3):763–768, 1986.

[9] N. Clarke. Target Morphologies via a Two-Step Dissolution-Quench Process in Polymer Blends. *Physical Review Letters*, 89(21):215506, 2002.

[10] T. Nishi, T. T. Wang, and T. K. Kwei. Thermally Induced Phase Separation Behavior of Compatible Polymer Mixtures. *Macromolecules*, 8(2):227–234, 1975.

[11] J. T. Cabral, J. S. Higgins, N. A. Yerina, and S. N. Magonov. Topography of Phase-Separated Critical and Off-Critical Polymer Mixtures. *Macromolecules*, 35(5):1941–1950, 2002.

[12] S. Kumar, S. Tan, L. Zheng, and D. M. Kochmann. Inverse-designed spinodoid metamaterials. *npj Computational Materials*, 6(73):1–10, 2020.

[13] S. Huang, L. Bai, M. Trifkovic, X. Cheng, and C. W. Macosko. Controlling the Morphology of Immiscible Cocontinuous Polymer Blends via Silica Nanoparticles Jammed at the Interface. *Macromolecules*, 49(10):3911–3918, 2016.

[14] A. L. Esquirol, P. Sarazin, and N. Virgilio. Tunable Porous Hydrogels from Cocontinuous Polymer Blends. *Macromolecules*, 47(9):3068–3075, 2014.

[15] J. S. Higgins and H. C. Benoit. *Polymers and Neutron Scattering*. Oxford University Press, 1994.

[16] R. Roe. *Methods of X-ray and neutron scattering in polymer science*. Oxford University Press, 2000.

[17] J. D. Gunton, M. San Miguel, and P. S. Sahni. *The Dynamics of First Order Phase Transitions*. Academic Press, London, 1983.

[18] J. D. Gunton and M. Droz. *Introduction to the Theory of Metastable and Unstable States*. Springer-Verlag, 1983.

[19] A. Z. Akcasu and R. Klein. A Nonlinear Theory of Transients Following Step Temperature Changes in Polymer Blends. *Macromolecules*, 26(6):1429–1441, 1993.

[20] J. W. Cahn and J. E. Hilliard. Free Energy of a Nonuniform System. I. Interfacial Free Energy. *The Journal of Chemical Physics*, 28(2):258–267, 1958.

[21] J. W. Cahn. On spinodal decomposition. *Acta Metallurgica*, 9(9):795–801, 1961.

[22] H. E. Cook. Brownian Motion in Spinodal Decomposition. *Acta Metallurgica*, 18(3):297–306, 1970.

[23] P. J. Flory. *Principles of Polymer Chemsitry*. Cornell University Press, 1953.

[24] M. L. Huggins. Some properties of solutions of long-chain compounds. *J. Phys. Chem.*, 46(1):151, 1942.

[25] P. G. de Gennes. Dynamics of fluctuations and spinodal decomposition in polymer blends. *The Journal of Chemical Physics*, 72(9):4756–4763, 1980.

[26] K. Binder. Collective diffusion, nucleation, and spinodal decomposition in polymer mixtures. *The Journal of Chemical Physics*, 79(12):6387–6409, 1983.

[27] H. L. Snyder, P. Meakin, and S. Reich. Dynamical Aspects of Phase Separation in Polymer Blends. *Macromolecules*, 16(5):757–762, 1983.

[28] T. Hashimoto, J. Kumaki, and H. Kawai. Time-Resolved Light Scattering Studies on Kinetics of Phase Separation and Phase Dissolution of Polymer Blends. 1. Kinetics of Phase Separation of a Binary Mixture of Polystyrene and Poly(vinyl methyl ether). *Macromolecules*, 16(4):641–648, 1983.

[29] J. S. Higgins and J. T. Cabral. A Thorny Problem? Spinodal Decomposition in Polymer Blends. *Macromolecules*, 53(11):4137–4140, 2020.

[30] K. Binder and P. Fratzl. *Spinodal Decomposition*. Wiley, 2001.

[31] A. Z. Akcasu, I. Bahar, B. Erman, Y. Feng, and C. C. Han. Theoretical and experimental study of dissolution of inhomogeneities formed during spinodal decomposition in polymer mixtures. *The Journal of Chemical Physics*, 97(8):5782–5793, 1992.

[32] A. Z. Akcasu, B. Erman, and I. Bahar. Nonlinear Kinetics of Spinodal Decomposition, and Dissolution of Inhomogeneities Formed by Spinodal Decomposition in Polymer Blends. *Makromolekulare Chemie. Macromolecular Symposia*, 62(1):43–60, 1992.

[33] S. L. Brunton and J. N. Kutz. *Data-Driven Science and Engineering: Machine Learning, Dynamical Systems, and Control*. Cambridge University Press, 2019.

[34] S. J. Blundell and K. M. Blundell. *Concepts in thermal physics*. Oxford University Press, 2006.

[35] M. L. Huggins. Solutions of Long Chain Compounds. *The Journal of Chemical Physics*, 9(5):440–440, 1941.

[36] P. J. Flory. Thermodynamics of high polymer solutions. *J. Chem. Phys.*, 10(1), 1942.

[37] J. H. Hildebrand. The term 'regular solution'. *Nature*, 168:868, 1951.

[38] M. Doi. *Introduction to polymer physics*. Oxford University Press, 1996.

[39] J. E. Mark. *Physical properties of polymers handbook*. Springer, 2007.

[40] M. Rubinstein and R. H. Colby. *Polymer physics*. Oxford University Press, 2003.

[41] R. A. L. Jones and R. W. Richards. *Polymers at Surfaces and Interfaces*. Cambridge University Press, 1999.

[42] E. L. Wood. *Phase separation in areospace polymer blends*. PhD thesis, University of Sheffield, 2019.

[43] F. S. Bates. Polymer-Polymer Phase Behavior. *Science*, 251(4996):898–905, 1991.

[44] F. S Bates and P. Wiltzius. Spinodal decomposition of a symmetric critical mixture of deuterated and protonated polymer. *J. Chem. Phys*, 91(5):3258–3274, 1989.

[45] J. W. Cahn. Phase Separation by Spinodal Decomposition in Isotropic Systems. *The Journal of Chemical Physics*, 42(1):93–99, 1965.

[46] J. W. Cahn. The 1967 Institute of Metals Lecture - Spinodal Decomposition. *Transactions of the Metallurgical Society of AIME*, 242(1):89–104, 1968.

[47] S. Coveney. *Fundamentals of phase separation in polymer blend thin films*. Springer, 2015.

[48] N. Goldenfeld. *Lectures on phase transitions and the renormalization group*. CRC Press, 2018.

[49] R. Zwanzig. *Nonequilibrium statistical mechanics*. Oxford University Press, 2001.

[50] P. G. de Gennes. *Scaling Concepts in Polymer Physics*. Cornell University Press, 1979.

[51] A. Z. Akcasu and I. C. Sanchez. A closed-form, free-energy functional for a binary polymer mixture. *Journal of Chemical Physics*, 88(12):7847–7850, 1988.

[52] H. Manzanarez, J. P. Mericq, P. Guenoun, J. Chikina, and D. Bouyer. Modeling phase inversion using Cahn-Hilliard equations – Influence of the mobility on the pattern formation dynamics. *Chemical Engineering Science*, 173:411–427, 2017.

[53] S. C. Glotzer. Computer Simulations of Spinodal Decomposition in Polymer Blends. In *Annual Reviews of Computational Physics II*, pages 1–46. World Scientific, 1995.

[54] N. Gibbions. *Hydrodynamics in a minimal nanocomposite system: theoretical description and computational simulation*. PhD thesis, University of Sheffield, 2022.

[55] A. Z. Akcasu. The 'fast' and 'slow' mode theories of interdiffusion in polymer mixtures: resolution of a controversy. *Macromol. Theory Simul*, 6(4):679–702, 1997.

[56] C. Castellano and S. C. Glotzer. On the mechanism of pinning in phase-separating polymer blends. *J. Chem. Phys*, 103(21):9363–9369, 1995.

[57] M. Jones and N. Clarke. Machine learning real space microstructure characteristics from scattering data. *Soft Matter*, 17(42):9689–9696, 2021.

[58] K. F. Riley, M. P. Hobson, and S. J. Bence. *Mathematical methods for physics and engineering*. Cambridge University Press, 2006.

[59] A. Z. Akcasu. Fluctuations of Macrovariables in Nonlinear Systems: Langevin Equation Approach. *Journal of Statistical Physics*, 16(1), 1977.

[60] G. R. Strobl. Structure Evolution during Spinodal Decomposition of Polymer Blends. *Macromolecules*, 18(3):558–563, 1985.

[61] J. S. Langer, M. Bar-On, and H. D. Miller. New computational method in the theory of spinodal decomposition. *Physical Review A*, 11(4):1417–1429, 1975.

[62] S. L. Brunton, B. R. Noack, and P. Koumoutsakos. Machine Learning for Fluid Mechanics. *Annu. Rev. Fluid Mech.*, 52:477–508, 2020.

[63] S. A. Billings. *Nonlinear System Identification: NARMAX Methods in the Time, Frequency, and Spatio-Temporal Domains*. John Wiley and Sons, Ltd, 2013.

[64] C. Wehmeyer and F. Noe. Time-lagged autoencoders: Deep learning of slow collective variables for molecular kinetics. *J. Chem. Phys.*, 148(241703):1–9, 2018.

[65] S. Hochreiter and J. Schmidhuber. Long short-term memory. *Neural computation*, 9(8):1735–1780, 1997.

[66] S. L. Brunton, J. N. Kutz, J. L. Proctor, and B. W. Brunton. *Dynamic Mode Decomposition: Data-Driven Modeling of Complex Systems*. SIAM, 2016.

[67] P. J. Schmid. Dynamic mode decomposition of numerical and experimental data. *J. Fluid Mech*, 656:5–28, 2010.

[68] J. H. Tu, C. W. Rowley, D. M. Luchtenburg, S. L. Brunton, and J. N. Kutz. On dynamic mode decomposition: theory and applications. *Journal of Computational Dynamics*, 1(2):391–421, 2014.

[69] R. Penrose. A generalized inverse for matrices. *Mathematical Proceedings of the Cambridge Philosophical Society*, 51(3):406–413, 1955.

[70] J. L. Proctor, S. L. Brunton, and J. N. Kutz. Dynamic Mode Decomposition with Control. *SIAM J Applied Dynamical Systems*, 15(1):142–161, 2016.

[71] D. Sashidhar and J. N. Kutz. Bagging, optimized dynamic mode decomposition for robust, stable forecasting with spatial and temporal uncertainty quantification. *Philosophical Transactions of the Royal Society A*, 380(2229):1–16, 2022.

[72] Z. Wu, S. L. Brunton, and S. Revzen. Challenges in dynamic mode decomposition. *Journal of the Royal Society Interface*, 18(185):1–11, 2021.

[73] N. Demo, M. Tezzele, and G. Rozza. PyDMD: Python Dynamic Mode Decomposition. *Journal of Open Source Software*, 3(22):530, 2018.

[74] J. Bongard and H. Lipson. Automated reverse engineering of nonlinear dynamical systems. *Proceedings of the National Academy of Sciences of the United States of America*, 104(24):9943–9948, 2007.

[75] M. Schmidt and H. Lipson. Distilling free-form natural laws from experimental data. *Science*, 324(5923):81–85, 2009.

[76] S. L. Brunton, J. L. Proctor, and J. N. Kutz. Discovering governing equations from data by sparse identification of nonlinear dynamical systems. *Proceedings of the National Academy of Sciences of the United States of America*, 113(15):3932–3937, 2016.

[77] S. L. Brunton. (2021, August 27), Sparse Identification of Nonlinear Dynamics (SINDy): Sparse Machine Learning Models 5 Years Later! https://doi.org/10.52843/cassyni.sx3npx.

[78] S. L. Brunton. (2021, September 10), Sparse Nonlinear Dynamics Models with SINDy, Part 2: Training Data and Disambiguating Models. https://doi.org/10.52843/cassyni.y7yb6y.

[79] S. L. Brunton. (2021, September 24), Sparse Nonlinear Dynamics Models with SINDy, Part 3: Effective Coordinates for Parsimonious Models. https://doi.org/10.52843/cassyni.5z2jld.

[80] S. L. Brunton. (2021, October 8), Sparse Nonlinear Dynamics Models with SINDy, Part 4: The Library of Candidate Nonlinearities. https://doi.org/10.52843/cassyni.p7t7ds.

[81] S. L. Brunton. (2021, October 22), Sparse Nonlinear Dynamics Models with SINDy, Part 5: The Optimization Algorithms. https://doi.org/10.52843/cassyni.f1bn05.

[82] K. Champion, B. Lusch, J. N. Kutz, and S. L. Brunton. Data-driven discovery of coordinates and governing equations. *Proceedings of the National Academy of Sciences of the United States of America*, 116(45):22445–22451, 2019.

[83] S. H. Rudy, A. Alla, S. L. Brunton, and J. N. Kutz. Data-driven identification of parametric partial differential equations. *SIAM J Applied Dynamical Systems*, 18(2):643–660, 2019.

[84] S. H. Rudy, S. L. Brunton, J. L. Proctor, and J. N. Kutz. Data-driven discovery of partial differential equations. *Science Advances*, 3(4):1–6, 2017.

[85] H. Schaeffer. Learning partial differential equations via data discovery and sparse optimization. *Proceedings of the Royal Society A: Mathematical, Physical and Engineering Sciences*, 473(2197):20160446, 2017.

[86] B. M. de Silva, K. Champion, M. Quade, JC. Loiseau, J. N. Kutz, and S. L. Brunton. PySINDy: A Python package for the sparse identification of nonlinear dynamical systems from data. *Journal of Open Source Software*, 5(49):2104, 2020.

[87] A. A. Kaptanoglu, B. M. de Silva, U. Fasel, K. Kaheman, A. J. Goldschmidt, J. Callaham, C. B. Delahunt, Z. G. Nicolaou, K. Champion, JC. Loiseau, J. N. Kutz, and S. L. Brunton. PySINDy: A comprehensive Python package for robust sparse system identification. Journal of Open Source Software. *Journal of Open Source Software*, 7(69):3394, 2022.

[88] S. H. Rudy, S. L. Brunton, J. L. Proctor, and J. N. Kutz. (2016) PDE-FIND GitHub Repository. https://github.com/snagcliffs/PDE-FIND?tab=readme-ov-file.

[89] S. H. Rudy, A. Alla, S. L. Brunton, and J. N. Kutz. (2018) Parametric PDE-FIND GitHub Repository. https://github.com/snagcliffs/parametric-discovery.

[90] A. Chakrabarti, R. Toral, J. D. Gunton, and M. Muthukumar. Spinodal Decomposition in Polymer Mixtures. *Physical Review Letters*, 63(19):2072–2075, 1989.

[91] A. Chakrabarti, R. Toral, J. D. Gunton, and M. Muthukumar. Dynamics of phase separation in a binary polymer blend of critical composition. *The Journal of Chemical Physics*, 92(11):6899–6909, 1990.

[92] J. D. Gunton, R. Toral, and A. Chakrabarti. Numerical Studies of Phase Separation in Models of Binary Alloys and Polymer Blends You may also like Physics of active emulsions Numerical Studies of Phase Separation in Models of Binary Alloys and Polymer Blends. *Physica Scripta*, T33:12–19, 1990.

[93] P. J. Flory. *Statistical mechanics of chain molecules*. Interscience, 1969.

[94] J. Bezanson, A. Edelman, S. Karpinski, and V. B. Shah. Julia: A Fresh Approach to Numerical Computing. *SIAM Review*, 59(1):65–98, 2017.

[95] T. Besard, C. Foket, and B. De Sutter. Effective Extensible Programming: Unleashing Julia on GPUs. *IEEE transactions on parallel and distributed systems*, 30(4), 2019.

[96] M. Jones. (2024) Polymeric spinodal decomposition and dissolution GitHub Repository. https://github.com/mpjones1/PhD.

[97] T. M. Rogers, K. R. Elder, and R. C. Desai. Numerical study of the late stages of spinodal decomposition. *Physical Review B*, 37(16):9638–9649, 1988.

[98] L. Isserlis. On a Formula for the Product-Moment Coefficient of any Order of a Normal Frequency Distribution in any Number of Variables. *Biometrika*, 12(1/2):134–139, 1918.

[99] C. C. Han and A. Z. Akcasu. Phase Decomposition in Polymers. *Annual Review of Physical Chemistry*, 43:61–90, 1992.

[100] A. Z. Akcasu. Microscopic Derivation and Extension of The Cahn-Hilliard-Cook Theory In Polymer Blends. *Macromolecules*, 22(9):3682–3689, 1989.

[101] I. C. Henderson and N. Clarke. Two-Step Phase Separation in Polymer Blends. *Macromolecules*, 37(5):1952–1959, 2004.

[102] T. Hashimoto, M. Itakura, and N. Shimidzu. Late stage spinodal decomposition of a binary polymer mixture. II. Scaling analyses on Qm(τ) and Im(τ). *The Journal of Chemical Physics*, 85(11):6773–6786, 1986.

[103] T. L. Tran, P. K. Chan, and D. Rousseau. Morphology control in symmetric polymer blends using two-step phase separation. *Computational Materials Science*, 37(3):328–335, 2006.

[104] A. Mendible, S. L. Brunton, A. Y. Aleksandr, W. Lowrie, and J. N. Kutz. Dimensionality reduction and reduced-order modeling for traveling wave physics. *Theoretical and Computational Fluid Dynamics*, 34(4):385–400, 2020.

[105] A. Aksimentiev, K. Moorthi, and R. Holyst. Scaling properties of the morphological measures at the early and intermediate stages of the spinodal decomposition in homopolymer blends. *Journal of Chemical Physics*, 112(13):6049–6062, 2000.

[106] M. Fiałkowski and R. Hołyst. The unphysical pinning of the domain growth during the separation of homopolymer blends near the spinodal. *The Journal of Chemical Physics*, 120(12):5802–5808, 2004.

[107] L. Ramírez-Piscina, J. M. Sancho, and A. Hernández-Machado. Numerical algorithm for Ginzburg-Landau equations with multiplicative noise: Application to domain growth. *Physical Review B*, 48(1):125, 1993.

[108] R. Petschek and H. Metiu. A computer simulation of the time-dependent Ginzburg–Landau model for spinodal decomposition. *The Journal of Chemical Physics*, 79(7):3443–3456, 1983.

[109] R. Toral and P. Colet. *Stochastic Numerical Methods: An Introduction for Students and Scientists*. Wiley-VCH, 2014.